https://doi.org/10.15388/vu.thesis.585
https://orcid.org/0000-0002-6616-4353

VILNIUS UNIVERSITY
STATE RESEARCH INSTITUTE CENTER FOR PHYSICAL SCIENCE AND TECHNOLOGY

Katsiaryna Charniakova

Synthesis and Characterization of Functional Coatings and Nanoparticles

DOCTORAL DISSERTATION

Natural Sciences,
Chemistry (N 003)

VILNIUS 2024

The dissertation was prepared between 2019 and 2023 (State Research Institute Center for Physical Science and Technology). The research was supported by the Research Council of Lithuania and the Polish National Agency for Academic Exchange.

Academic supervisor –
Dr. Arūnas Jagminas (Center for Physical Sciences and Technology, Natural Sciences, Chemistry – N 003).

This doctoral dissertation will be defended in a public meeting of the Dissertation Defence Panel:

Chairman – Prof. Habil. Dr. Aivaras Kareiva (Vilnius University, Natural Sciences, Chemistry – N 003).
Members:
Dr. Jurga Juodkazytė (Center for Physical Sciences and Technology Natural Sciences, Chemistry – N 003),
Dr. Tadas Malinauskas (Vilnius University, Natural Sciences, Physics – N 002),
Prof. Dr. Rimantas Raudonis (Vilnius University, Natural Sciences, Chemistry – N 003),
Assoc. Prof. Dr. Wojciech Stępniowski (Military University of Technology (Warsaw), Natural Sciences, Chemistry – N 003).

The dissertation shall be defended at a public meeting of the Dissertation Defence Panel at 14.00 on 21 February 2024 in conference hall A101 of the Center for Physical Sciences and Technology.

Address: Sauletekio av., 3, Vilnius, Lithuania, Tel. +37052648884; e-mail: office@ftmc.lt

The text of this dissertation can be accessed at the libraries of the Center for Physical Sciences and Technology and Vilnius University, as well as on the website of Vilnius University:
www.vu.lt/lt/naujienos/ivykiu-kalendorius

https://doi.org/10.15388/vu.thesis.585
https://orcid.org/0000-0002-6616-4353

VILNIAUS UNIVERSITETAS
VALSTYBINIS MOKSLINIŲ TYRIMŲ INSTITUTAS FIZINIŲ IR TECHNOLOGIJOS MOKSLŲ CENTRAS

Katsiaryna Charniakova

Funkcinės paskirties dangų ir nanodalelių sintezė ir charakterizavimas

DAKTARO DISERTACIJA

Gamtos mokslai,
Chemija (N 003)

VILNIUS 2024

Disertacija rengta 2019–2023 metais Valstybinis mokslinių tyrimų institutas Fizinių ir technologijos mokslų centro Elektrocheminės medžiagotyros skyriuje.

Mokslinius tyrimus rėmė Lietuvos mokslo tarybe ir Lenkijos nacionalinė akademinių mainų agentūre.

Mokslinis vadovas –
Dr. Arūnas Jagminas (Valstybinis mokslinių tyrimų institutas Fizinių ir technologijos mokslų centras, gamtos mokslai, chemija – N 003).

Gynimo taryba:
Pirmininkas – prof. habil. dr. Aivaras Kareiva (Vilniaus universitetas, gamtos mokslai, chemija – N 003).
Nariai:
dr. Jurga Juodkazytė (VMTI Fizinių ir technologijos mokslų centras, gamtos mokslai, chemija – N 003),
dr. Tadas Malinauskas (Vilniaus universtitetas, gamtos mokslai, fizika – N 002),
prof. dr. Rimantas Raudonis (Vilniaus universtitetas, gamtos mokslai, chemija – N 003),
dr. Wojciech Stępniowski (Karo technologijos universitetas (Varšuva), gamtos mokslai, chemija – N 003).

Disertacija ginama viešame Gynimo tarybos posėdyje 2024 m. vasario mėn. 21 d. 14.00 val. Fizinių ir technologijos mokslų centro A101 konferencijų salėje.

Adresas: Saulėtekio al. 3, LT-10257 Vilnius, tel. +37052648884; el. paštas office@ftmc.lt

Disertaciją galima peržiūrėti Vilniaus universiteto, Fizinių ir technologijos mokslų centro bibliotekose ir VU interneto svetainėje adresu:
https://www.vu.lt/naujienos/ivykiu-kalendorius

ABBREVIATIONS

AES	Auger electron spectroscopy
AHM	Ammonium heptamolybdate
CNPs	Carbon nanoparticles
EDX	Energy dispersive X-ray
EG	Ethylene glycol
EPR	Electron paramagnetic resonance
FA	Formic acid
FL	Fluorescence
FTIR	Fourier-transformed infrared spectroscopy
FWHM	Full width at half maximum
GNP	Graphene nanoparticles
HFS	Hyperfine structure
LSV	Linear sweep voltammetry
MS	Mass spectroscopy
NT	Nanotube
NTs	Nanotubes
OxA	Oxalic acid
PCs	Paramagnetic centers
RBS	Rutherford backscattering
SEM	Scanning electron microscopy
SERS	Surface-enhanced Raman scaterring
TEM	Transmittance electron microscopy
TG/DTA	Thermogravimetry/Differential thermal analysis
XAES	X-ray Auger electron spectroscopy
XPS	X-ray photoemission spectroscopy
XRD	X-ray diffraction

CONTENTS

INTRODUCTION

Valve metal anodizing is a widely applied and convenient process for obtaining ordered oxide nanomaterials with controllable properties. The anodizing conditions, such as anodizing voltage, type of electrolyte, concentrationб and temperature, significantly influence the morphology and composition of the obtained coatings and films. Modifying anodic oxides with the products of electrochemical oxidation of electrolyte components can create additional opportunities for regulating the properties of materials. In particular, during one-step aluminum anodizing in organic acids, such as oxalic, malonic, tartaric, and glycolic, the electrochemical anion transformation resulted in amorphous carbon formation and its incorporation into the alumina, which modified the fluorescence characteristics, shifting the fluorescence maximum positions or affecting emission intensity. Carbon/alumina composites can also be used as adsorbents, catalysts, catalyst supports, supercapacitors, electrode materials for fuel cells, and absorbents for storing gases. However, in the case of mentioned electrolytes, anodizing is high-field, i.e. it takes place at voltages above 100 V, which is too high for the wide use of these processes. Therefore, it is an urgent task to search for electrolytes that make it possible to obtain carbon-enriched alumina films at lower anodizing voltages.

Similarly, amorphous carbon can also be formed during titanium anodizing in organic electrolytes; modifying titania nanotubes with carbon enhances their photocatalytic activity. Carbon might also promote the oriented growth of TiO_2 nanocrystals, which affects the properties of the materials.

Therefore, one can develop new materials with the required morphological, physical-chemical, photocatalytic, or optical properties by knowing the processes of carbon species insertion in anodic oxides, their chemical nature, and their structural peculiarities.

Major goal

Show the possibility of one-stage electrochemical formation of carbon-containing anodic alumina and titania films, characterize them, and investigate the possible application areas of the obtained products.

Tasks

1. Investigate the peculiarities of electrochemical growth of carbon-containing aluminum anodic oxide films in electrolytes promoting carbon formation and incorporation.

2. Suggest the synthesis conditions to obtain anodic alumina films at lower anodizing voltages with higher carbon content compared with other anodically synthesized carbon/alumina composites.

3. Investigate the state of carbon inclusions during aluminum and titanium anodizing.

4. Determine the structure, composition, and fluorescence properties of the anodic films concerning the state, amount, and form of embedded carbon.

5. Extract the carbon phase from carbon-containing anodic alumina films and characterize it.

Statements of defense

1. Carbonaceous species embedded in the anodic alumina from formic acid and ammonium heptamolybdate (or sodium metavanadate) electrolyte is in the form of carboxylate ions and carbon species in the sp^2 and sp^3 states.
2. The average content of carbon incorporated into the formic acid films (ca. 5.0 mass.%) is approximately twice as high as entrapped in oxalic and tartaric anodic alumina films, typically formed at higher anodizing voltages.
3. The ammonium heptamolybdate and sodium metavanadate additives to the formic acid solution prevent the release of aluminum ions into the solution during aluminum anodizing, increasing the thickness of the films and promoting carbon incorporation into the alumina matrix. Oxalic acid additives affected the electrochemical oxidation process of aluminum, forming a thicker oxide layer with a smoother surface.
4. Carbonaceous species entrapped in formic acid alumina films exhibit excitation-dependent blue fluorescence.

Novelty

The use of additives of ammonium heptamolybdate, sodium metavanadate, and oxalic acid made it possible for the first time to obtain films of anodic aluminum oxide in a solution of formic acid with a thickness of more than 1 μm, namely 20–40 μm. Moreover, depending on the anodizing conditions, the average carbon content in the films did not decrease and amounted to 3.45–5.5 mass%, almost twice as much as in films obtained in solutions of oxalic and tartaric acids. In this case, the anodizing voltage was 80 V, comparable to the anodizing in a solution of oxalic acid and 2.5 times less than in a solution of tartaric acid. It was demonstrated that in anodic alumina films, CO_2 and CO molecules, carboxylate ions, and carbonaceous species in the sp^2 and sp^3 states were embedded in the oxide. Carbon-containing inclusions incorporated during the aluminum anodic oxidation into the oxide matrix were extracted from the films. It was shown for the first time that they exist as luminescent and biocompatible nanoparticles possessing an excitation-dependent emission behavior at 280–450 nm.

The practical value of the dissertation

1. Established and suggested conditions for the synthesis of carbon-enriched anodic alumina films in the complex electrolytes containing 0.4 M formic acid, 0.03 M ammonium heptamolybdate or 0.2 M sodium metavanadate, and oxalic acid, with an average carbon content of 5.0 mass.%.
2. Investigated the impact of ammonium heptamolybdate, sodium metavanadate, and oxalic acid additives to the formic acid solution on the morphology and composition of the anodic alumina films.
3. Established the amount as 3.45–5.75 mass% and form of carbon embedded in the anodic alumina as CO_2, CO, carboxylate ions, and carbonaceous species in the sp^2 and sp^3 states, depending on electrolyte composition.
4. Established a wide blue fluorescence of anodic alumina films in the wavelength range of 350–700 nm with a maximum at around 460 nm and the non-exponential fluorescence decay with an average lifetime of about 0.30–0.32 ns.
5. Carbon inclusions incorporated during the aluminum anodic oxidation into the oxide matrix can be extracted from the films, and they exist as luminescent and biocompatible nanoparticles possessing an excitation-dependent emission behavior at 280–450 nm with average lifetimes of 7.25–8.04 ns, depending on the composition of the initial film.

1. LITERATURE REVIEW

The process of anodic oxidation of metals and alloys has been known for over 100 years and is widely used to obtain protective and decorative coatings. During anodizing, a layer of a protective oxide film is formed on the surface of a metal, for example, on aluminum or tantalum, which prevents the interaction of the metal and the environment. Since the importance of the structure of anodic films is not limited to their decorative and protective properties, it is necessary to understand the basic mechanisms of film growth to increase their potential and realize their diverse functions.

1.1. Anodic oxide fabrication

Usually, metal foil and thin film anodizing is carried out in two-electrode glass or plastic electrochemical cells in electrolyte solutions at a constant temperature using the DC power supply (Figure 1.1, A). Electrolyte solutions are commonly stirred (by magnetic or mechanical stirring), reducing the double layer's thickness at the metal|electrolyte interface and ensuring uniform local current density and temperature over the electrode surface [1,2]. The horizontal arrangement of electrodes in the electrochemical cell can also be used (Figure 1.1, B) [3].

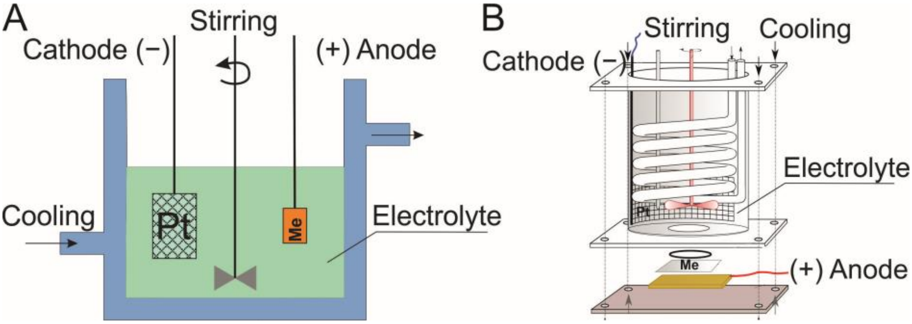

Figure 1.1. Schematic drawing of the two-electrode cells for metal anodizing: vertical cell (A) and horizontal cell (B). Adapted from Refs. [4–6].

Before anodizing, the samples should be pretreated to clean the surface (e.g., chemical etching, electropolishing, ultrasonication). The oxide can also be removed from the surface of the metal if one needs to obtain free-standing anodic oxide. Aluminum can be chemically dissolved in solutions containing $CuCl_2$ and HCl, or $HgCl_2$. Different methods are applied for titanium removal, including ultra-sonication after anodizing, rapid breakdown anodizing, and hydrothermal techniques [3,7].

1.1.1. Aluminum anodizing

The type of anodic alumina film that can be obtained on the surface of aluminum during anodizing depends on many factors, but one of the most important is the ***nature of the electrolyte***. *Barrier-type (compact) films* are formed on aluminum in electrolytes that practically do not dissolve alumina, e.g., aqueous solutions of boric acid, ammonium borate, or tartrate (pH 5–7), weak organic acids, e.g., citric, tartaric, and glycolic [3,5]. *Porous (structured) films* are formed on aluminum in electrolytes that partially dissolve alumina. Many such electrolytes exist; however, in industry, aqueous solutions of sulfuric, chromic, phosphoric, and oxalic acids are usually used [3,5]. It should be noted that the classification of anodic alumina films according to their ability to dissolve in electrolytes is rather conditional since both barrier- and porous-type films can be obtained in the same electrolyte solution depending on the concentration and other anodizing modes. Thus, porous films were obtained by anodizing aluminum in aqueous solutions of different carboxylic acids [5,8–12]. The barrier film of anodic alumina covers the metal surface with a dense layer. The thickness of the barrier layer depends on the anodizing voltage and is proportional to 1.4 nm V^{-1}. Due to the high resistivity of Al_2O_3 (10^{15}–10^{17} Ohm m [13]), dense anodic oxide layers, even ca. 1 μm thick, are difficult to obtain [3,5]. Porous alumina films are a system of ordered pores on the aluminum surface (Figure 1.2).

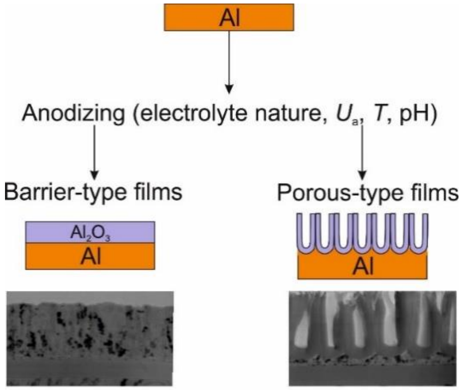

Figure 1.2. Two different types of anodic alumina films on alumina formed by barrier- and porous-type anodizing depending on the electrolyte nature. Adapted from Ref. [1].

The porous alumina structure can be represented as a hexagonal close packing of cylindrical pores perpendicular to the film surface (Figure 1.3). In films of anodic alumina, porous and barrier layers are isolated. The porous layer makes up most of the volume of the oxide. The barrier layer is a fairly thin and dense film at the base of the pores. The main characteristics of the anodic alumina structure are the degree of porosity, pore diameter, the distance between pores, pore wall thickness, and thickness of the porous and barrier layers.

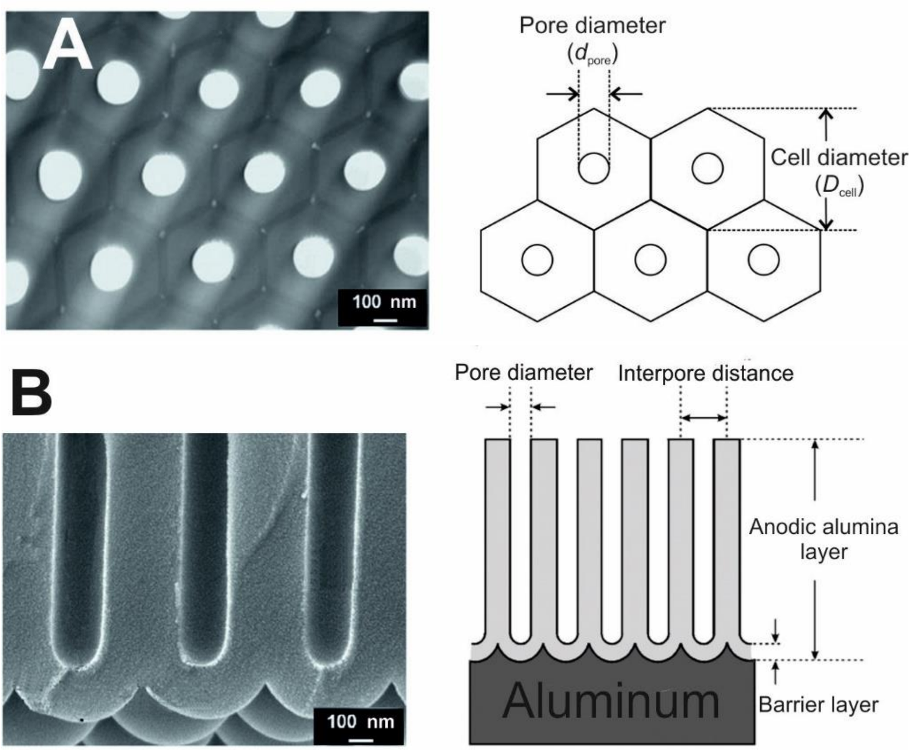

Figure 1.3. Schematic drawing of porous alumina structure. Adapted from Refs. [5,14].

The interpore distance is proportional to the ***anodizing voltage***. The values of the proportionality coefficient lie in the range $2.5 – 2.8\ \text{nm V}^{-1}$ [21]. It should be noted that the pore formation process is very complex, and, therefore, its mechanism has not yet been fully established.

Due to the greater permeability of porous films for the electrolyte solution, the limiting thickness of the oxide layer is ca. 100 μm or more. The thickness of the porous layer depends on the amount of electricity passed through the anode, i.e., it grows according to the Faraday law. Barrier layer thickness is also a function of anodizing voltage and electrolyte concentration and remains nearly constant and proportional to 1.0 nm V^{-1} in most electrolytes used [1,4,15].

The ***electrolyte concentration*** also significantly affects the structure of anodic alumina films only when porous coatings are obtained. Thus, it was shown in [3] that the pore diameter depends on the dissolution rate of alumina. The dissolution rate, in turn, depends on the pH of the solution in which oxidation is performed: the lower the pH of the electrolyte, the lower the voltage required for the dissolution of Al_2O_3 to begin at the bottom of the pore, and the smaller the diameter of the resulting pores. Pores of the minimum diameter are formed during oxidation in strong acids. Forming a highly ordered hexagonal structure requires an accurate selection of the concentration of the electrolyte solution.

The ***electrolyte temperature*** is another important factor affecting porous anodic alumina coatings' structure and protective properties. At low temperatures (0–5 °C), thick films are obtained with increased hardness and a highly ordered microstructure. At a higher temperature (60–75 °C), the rate of chemical dissolution of Al_2O_3 increases several times, and a thin oxide layer with poor protective properties is formed. In addition, maintaining a low anodizing temperature helps prevent local overheating at the bottom of the pores, which occurs due to the release of heat during the flow of electric current and can lead to an uneven distribution of the electric field strength, which can lead to the breakdown of the oxide layer. The anodizing temperature determines the growth rate of the oxide layer: the lower the temperature, the lower the growth rate of the oxide layer [3,5,16]. The ***anodizing current density*** only affects the structure and composition of porous anodic alumina films. With increasing anodizing current density, the time for obtaining coatings decreases (the higher the current density, the thicker the film, and in less time it is possible to obtain [16]), and the degree of ordering of the cellular-porous structure of anodic alumina increases (the spread of pores in diameter decreases) [17]. The composition of the formed alumina depends on the anodizing current density [1,10,11].

1.1.2. Titanium anodizing

The tubular titania arrays are formed in fluoride-containing electrolytes through three main processes: 1) oxidation of metallic titanium with the formation of barrier-type TiO_2 on its surface; 2) pitting/nanopore formation; 3) steady-state nanotube growth (Figure 1.4). The structure of the resulting oxide layer on the metal surface mainly depends on the concentration and composition of the electrolyte solution and the applied voltage.

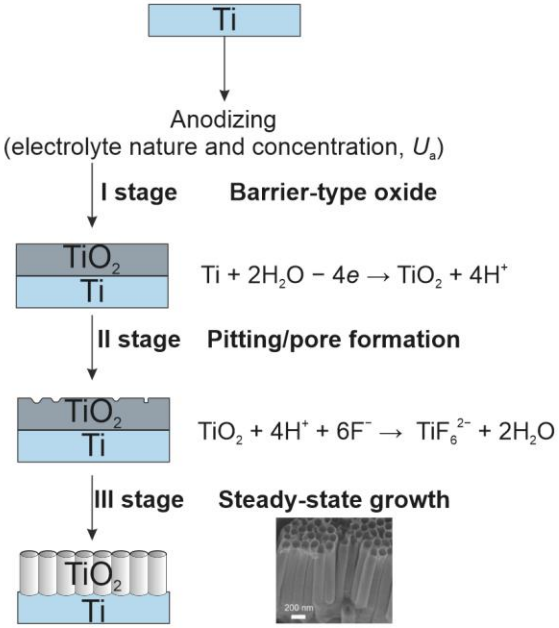

Figure 1.4. Schematic drawing of nanotube titania growth during Ti anodizing in fluoride-containing electrolytes. Adapted from Refs. [7,18,19].

The as-formed titania nanotubes (TNTs) are mostly amorphous [3,6,20]. However, amorphous coatings can be converted into anatase or rutile at temperatures above 450 °C [21,22]. The nanotube structure is stable to ca. 550 °C [6].

1.2. Mechanism of metal anodic oxidation

During anodizing, metals are oxidized at the Me|oxide interface, yielding Me^{z+} ions:

$$\mathrm{Me} \rightarrow \mathrm{Me}^{z+} + ze^{-}$$

So, a double layer is localized at the Me|oxide interface, where metal oxide acts as a solid electrolyte. The relevant diffuse double-layer thickness is small and is mainly determined by the Helmholtz layer. At the oxide|solution interface, oxygen ions enter the oxide. Oxygen ions can be formed by the following reactions:

$$\mathrm{H_2O} \rightarrow \mathrm{OH^-_{(ad)}} + \mathrm{H^+}$$

$$\mathrm{OH^-_{(ad)}} \rightarrow \mathrm{O^{2-}_{(ad)}} + \mathrm{H^+}$$

$$O^{2-}_{(ad)} \rightarrow O^{2-}_{(ox)}$$

Cations drift through the oxide layer due to the electric field and are ejected into the solution at the oxide|electrolyte interface (Figure 1.5, A). At the same time, oxygen-containing ions, such as O^{2-} and OH^{-}, migrate from the electrolyte|oxide interface through the oxide layer to the metal|oxide interface, resulting in metal oxidation. The electrolyte anions are adsorbed at the pore bottom|electrolyte interface. All anions are pulled toward the positively charged electrode by the electric field. The migration rate of electrolyte ions is much lower than that of OH^{-} or O^{2-} ions due to their larger size and lower mobility. As a result, the concentration of electrolyte anions will decrease from the outer to the inner layers.

Ionic transfer numbers differ in the oxide layer for cations and anions. The relative contribution of anions and cations to the charge transport varies among the types of metal oxides and depends on the process conditions. An oxide film can grow at the outer (closer to the oxide|electrolyte interface (Figure 1.5, B)) or inner (closer to metal|oxide interface (Figure 1.5, C)) oxide interface depending on the ionic transport number of oxygen ions compared with metal cations.

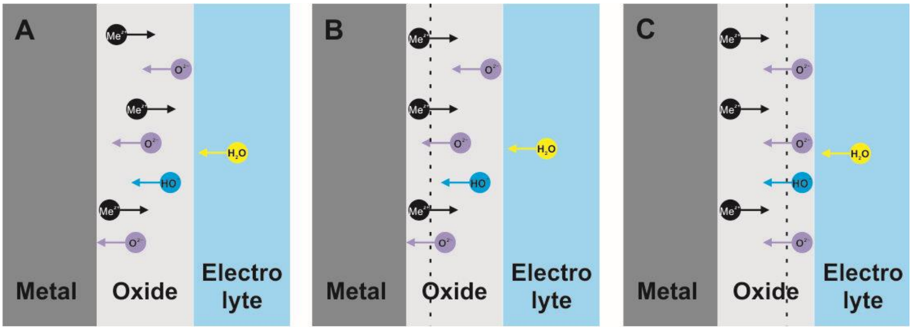

Figure 1.5. Migration of ions through the oxide layer under the applied high electric field (A). Influence of ionic transport numbers on the location of oxide formation zone: inward anionic transport is dominant (B), and outward cationic transport is dominant (C). Adapted from Ref. [3].

For most valve metals (Al, Ta, Nb, and Ti), both ions contribute to the ionic current, and oxide is formed at both interfaces [3,23,24].

1.3. Chemical and phase composition of anodic alumina films

Determining the composition of anodic alumina is an important issue that requires detailed study since films and membranes of anodic alumina are currently widely used in industry. Solutions of sulfuric, phosphoric, and oxalic acids are the most commonly used electrolytes in the industry for the production of coatings from anodic alumina. Therefore, most works are devoted to studying alumina obtained in these electrolytes, which have been used for over 100 years. However, anodic alumina is also formed in other electrolytes, but the physicochemical properties of such films and membranes have not been sufficiently studied: the surface morphology and kinetics of film growth on aluminum have been mainly studied.

In recent decades, the ***chemical composition*** of anodic alumina and the distribution of electrolyte components in the oxide matrix have been studied [1,3,5,25]. To study the amorphous structure, phase composition of anodic alumina, and polymorphic transformations in films, the following research methods were used: solid-state nuclear magnetic resonance spectroscopy (NMR) [26,27], infrared (IR) spectroscopy [11,28], small-angle X-ray phase analysis (XRD) [29], thermogravimetric (TG) and differential thermal (DTA) analyses [30]; to determine the quantity and state of electrolyte components, as well as their distribution over the depth of the film – Auger spectroscopy [31], Rutherford backscattering spectroscopy (RBS) [32], secondary ion mass spectroscopy (SIMS), TL-OES, glow-discharge optical emission spectroscopy (GDOES) [33,34], and XPS [35]. According to these studies, ***anodic alumina is an X-ray amorphous material*** and is a mixture of hydroxide $Al(OH)_3$ and aluminum oxyhydroxide AlOOH, hydrated aluminum oxide Al_2O_3 $(H_2O)_{0...3}$ and anions and (or) their oxidation products built into the alumina matrix from an electrolyte solution.

The chemical composition of anodic alumina has also been a long-discussed issue. However, despite the variety of research methods, there is no consensus on this question. The main difference between nanostructured alumina and alumina obtained by other methods is that the process of anodizing aluminum is accompanied by the introduction of electrolyte components into the forming alumina layer. The nature of these inclusions and their transformation during anodizing and annealing remain the subject of many years of debate.

In the first works devoted to studying the composition of nanostructured anodic alumina, it was found that during anodizing, the electrolyte components are incorporated only into the outer layer of alumina, i.e., the layer immediately adjacent to the solution forms an oxide film, and its inner layer is almost pure alumina [8,36–38]. The content of electrolyte components in anodic alumina depends on the electrolyte and anodizing modes (current density, temperature) and can range from 2–3% (for oxalic acid) to 10–13% (for sulfuric acid) [5]. It is known that the inclusions of electrolyte components affect the physicochemical properties of anodic alumina: color, photoluminescence, ionic and electronic conductivities, dissolution, and crystallization rates [27,30,39,40].

The first works of Japanese scientists were devoted to studying the reasons for the coloring of nanostructured films of anodic alumina formed in various organic acids, for example, oxalic, maleic, malonic, formic, and tartaric. By comparing IR and ESR spectroscopy data, the authors found that a signal with a g factor of 2.0044–2.0050, $\Delta H = 0.8$ mT, in the oxide is caused by carbon-containing radicals formed from electrolyte anions in the process of electrochemical oxidation [8,36–38].

Later, nanostructured anodic alumina films formed in an oxalic acid solution were studied [41]. IR and EPR spectroscopy methods were used to establish the sequence of transformations of oxalate ions during anodizing, their state (degree of oxidation of carbon atoms) in the oxide matrix, and depth distribution. Since the EPR signal corresponding to the stoichiometric aluminum carboxylic acid complex or carboxylic acids was not detected, and IR spectroscopy data (when compared with the spectra of oxalic acid and aluminum oxalate) also did not confirm the presence of oxalate -ions, so the authors concluded that oxalic acid anions, under the influence of a high-intensity electric field, are partially oxidized and incorporated into the barrier layer of porous alumina in the form of carboxylate ions.

Subsequent studies of porous alumina were devoted mainly to studying the migration of ions in the oxide during anodizing and the distribution of electrolyte components in depth [42]. A group of scientists led by Thompson and Wood [32], based on RBS data, proposed a model that explains the mechanisms of adsorption and incorporation of electrolyte anions into anodic alumina with their possible subsequent transformation under the influence of an electric field.

In one of the works of the same team of authors, the approximate composition of porous aluminum oxide was established using the RBS method – $Al_2O_3 \cdot 0.025Al_2[(COO)_2]_3$ and $Al_2O_3 \cdot 0.014Al_2[CH_2(COO)_2]_3$ – for films obtained in solutions of oxalic and malic acids, respectively [43]. One of the disadvantages is that the authors did not determine the state of the electrolyte components but believed that the anions are embedded in the barrier oxide layer without oxidizing.

In [41,44], the composition of anodic alumina films obtained in solutions of oxalic, sulfosalicylic, and sulfuric acids was studied using IR spectroscopy. The nature of the electrolyte had the greatest influence on the general appearance of the IR absorption spectra. More detailed studies on the effect of anodizing modes on the properties of anodic alumina were carried out on films formed in a solution of oxalic acid. It was shown that the thickness of the anodic alumina film determined the position of individual bands in the spectra. At the same time, the influence of voltage, current density, and electrolyte concentration had an insignificant effect.

In the spectra of porous alumina films obtained in oxalic acid, against the background of a broad band of 400–1000 cm^{-1} characterizing amorphous Al_2O_3, are peaks corresponding to vibrations of the Al–O bond in isolated and connected AlO_4 tetrahedra (700–900 cm^{-1} and 800–850 cm^{-1}), in isolated and bonded AlO_6 octahedra (400–500 and 500–570 cm^{-1}) in various modifications of aluminum oxide. The main difference between nanostructured anodic alumina obtained in solutions of organic acids and those obtained in inorganic acids is the presence of a doublet band of carboxylate ions at 1420–1480 and 1500–1600 cm^{-1} (Table 1.1).

Table 1.1. Absorption maxima of the IR spectra of nanostructured anodic alumina films obtained in solutions of organic acids [30,41,44]

Wavenumbers, cm^{-1}	**Assignment**
500–400	$\nu_{as}(AlO_6)$
700–500	$\nu_s(AlO_6)$
850–800	$\nu_{as}(AlO_4)$
900–700	$\nu_s(AlO_4)$
980–920	δ(OH) Al–O–H or ν(Al=O)
1150–1100	δ(Al–OH)
1480–1420	$\nu_{as}(COO^-)$
1600–1500	ν_s(COO–)
2100–2000	ν(C–O) in CO molecule
2350–2300	ν(C=O) in CO_2 molecule
3100–3050	ν(OH) boehmite AlOOH
3450–3350	ν_s(OH) in H_2O
3500–3700	$\nu_{as}(OH_{surf})$

Based on their presence in the IR transmission spectra of anodic films obtained in solutions of oxalic and formic acids, depending on the time of oxide dissolution, the authors of the work proved that carbon-containing components of the electrolyte are in the surface layer of the oxide in the form of carboxylate ions. The partial oxidation of organic acid anions during anodizing is also evidenced by the presence of ν(C–O) bands of CO molecules at 2000–2100 cm^{-1} in the spectra of the initial anodic alumina (see Table 1.1). Stretching vibrations of the C–O bonds of CO_2 molecules can appear due to the adsorption of air CO_2 or the oxidation of electrolyte anions.

1.4. Carbon-containing oxide films obtained by metal anodizing

As is known, the electrolyte anions are incorporated into the alumina during aluminum anodizing. Depending on the electrolyte type, the electrolyte species can be immobile and migrate inward or outward throughout the oxide under the electric field, thus affecting the morphological, optical, and physical-chemical properties of the alumina films [1,23]. For example, Minguez-Bacho et al. [45], while studying the optical properties of sulfuric acid anodic alumina, pointed out that the refractive index of nanoporous anodic alumina films depended on the concentration of incorporated sulfate anions. Fan et al. [46] showed that increasing the annealing temperature during the heat treatment of the oxalic acid anodic alumina affected its refractive index by decreasing the concentration of oxalic impurities due to their thermal decomposition. Many studies are also devoted to the influence of electrolyte-derived anions on the fluorescence of porous anodic alumina films obtained in inorganic and organic acids. The most pronounced effect was observed in the samples formed in organic acids, e.g., oxalic, malonic, tartaric, glycolic, and others [5,47,48]. The electrochemical anion transformation, followed by their incorporation into the alumina, modified the fluorescence characteristics, shifting the fluorescence maximum positions or affecting emission intensity. Our previous investigations showed that alumina/carbon composites with an average carbon content of about 3.2 mass.% could be obtained during one-stage electrochemical aluminum oxidation in the aqueous solution of tartaric acid at ca. 180 V [11,12,49]. However, the anodizing voltage is too high for the wide use of this process.

Even though it is commonly accepted that anodic films thicker than 100 nm on the aluminum surface cannot be formed in monocarboxylic acid solutions [37], at relatively high temperatures and concentrations, porous oxide layers with irregular structure within a wide range of anodic voltages can be formed [50,51]. Pashchanka and Schneider [52] reported that porous alumina with a clear tendency to hexagonal order was formed in cold solutions at 18–30 V. However, preparing porous alumina in an aqueous solution of formic acid is a rather complicated and long procedure since the process takes more than 20 h and produces a film with a thickness of about 200 nm [52]. Klimas et al. demonstrated that aluminum anodizing in formic acid allows for obtaining porous anodic alumina films at lower voltages (ca. 22 V) and with a higher carbon content of ca. 5.8 at.% [53] compared with anodizing in other organic acids such as oxalic, malonic, and tartaric (Table 1.2). However, formic acid anodic alumina films did not possess the regular porous structure, and their thickness did not exceed 1 μm. The exact decomposition mechanism of formate ions and the insertion pathway of carbon-containing species are not discussed and still require further investigation.

Table 1.2. Comparison of carbon content and anodizing conditions for porous alumina formed in different acids

Acid	**C content, at%**	**Anodizing voltage, V**	**Refs.**
Formic	5.8	22–25	[53]
Oxalic	2–3	40–60	[5]
Malonic	ca. 3	120	[5]
Tartaric	4.7–7.8	180	[11,12,49]

Therefore, the ways for morphology improvement and thickness increase should also be explored. According to the existing ideas about aluminum anodizing process improvement when organic compounds and/or complex oxyanions are added to the electrolyte solutions, they can not only reduce the dissolution rate durig anodizing [54–58] but also inhibit the chemical dissolution of pore walls by adsorbing and changing the double-layer structure at the oxide|electrolyte interface thus improving film morphology and thickness. As earlier, it was demonstrated that oxalic acid additives affected the electrochemical oxidation process of aluminum in sulfuric acid solution, leading to the formation of a more compact oxide layer and improvement of film growth and their mechanical properties [24,54,59]. It was also shown that molybdate additions changed the rate of thickening of anodic alumina during anodizing in sulfuric acid or the mixture of sulfuric and tartaric acids [55,57,59,60]. The behavior of oxyanions, e.g., molybdates, in acidic media is complex. Molybdates are polymeric in the solutions with $pH < 4.5$ [61]. According to Thompson et al. [62], steric factors determine the ease of anion embedding in the film. Hence, the large polymeric molybdate species cannot be easily incorporated compared with smaller metavanadate ions. Oxyanions changed the morphology of the anodic films, making them more compact, less porous, and more corrosion-resistant.

Therefore, the strategy for improving the aluminum anodizing process in formic acid might be the following: one can add to the anodizing electrolyte small amounts of oxyanions, such as vanadates, molybdates, tungstates, and/or organic acids, such as oxalic or tartaric.

It should be noted that electrolyte species oxidation and their further incorporation into the oxide structure usually occur during valve metal anodizing. Amorphous carbon can also be formed during titanium anodizing in ethylene glycol due to electrochemical oxidation of the electrolyte species [63–65]. For example, based on XPS studies, Winiarski et al. [66]

concluded that organic carbon (ca. 4–7 at.%) was built into the TiO_2 layer during titanium anodizing. Modifying anodic titania with the products of electrochemical oxidation of electrolyte components can create additional opportunities for tailoring the properties of materials. In particular, modifying titania nanotubes (TiNTs) with carbon enhances their photocatalytic activity [67–69]. Carbon might also promote the oriented growth of TiO_2 nanocrystals, which affects the properties of the materials [70]. The presence of carbon and carboxylate ions can impact the photocatalytic activity and the electrophysical and optical properties of the oxides.

1.5. Fluorescence properties of anodic alumina films

The nature and mechanism of fluorescence (FL) of anodic alumina films obtained in various electrolytes have been debated for many years. It has been established that anodic alumina exhibits a broad fluorescence (full width at half maximum (FWHM) 100–150 nm) in the wavelength range 300–600 nm with excitation of 250–470 nm [37,40,48,71–74]. However, the origin of the fluorescence in anodic alumina formed in organic and inorganic acids is still unclear. At least two states might be responsible for blue fluorescence [47,75–77]. Like the porous alumina films obtained in organic acid solutions, films formed in sulfuric acid solutions also possess near-UV and visible fluorescence. By analogy with α-Al_2O_3, in anodic alumina, it is assumed that oxygen vacancies have captured one or two electrons from F^+ and F centers, respectively. Obviously, in the case of sulfuric acid anodizing, oxygen vacancies or other structure defects can be responsible for the fluorescence. However, the situation is not so determined for anodizing in organic acid solutions as carbon and other carbon-containing inclusions are also optically active [78,79]. Some authors believe that oxygen defects determine the electronic and optical properties of anodic alumina [40,71,72,74]. Others suggest that the fluorescence could be attributed to the organic impurities, such as carboxylate species and structures or amorphous carbon, incorporated into the oxide during the anodizing [11,36,77,80]. As was reported before [78,81], both the electrochemically derived amorphous carbon and OH groups adsorbed at the surface and in the bulk of alumina also have a green/blue fluorescence at the same spectral range.

2. MATERIALS AND METHODS

2.1. Aluminum and titanium anodizing in electrolytes containing organic compounds

2.1.1. Aluminum anodizing in a formic acid solution containing sodium metavanadate

Deionized distilled water was used in the preparation of all solutions. Vanadic and formic acids were of analytical grade. Aluminum samples cut from high purity (99.99 at.%, Goodfellow) foil in thickness of 125 μm into coupons 17 × 17 mm^2 were used. Before anodizing, the specimens were etched in the solution of 1.5 M NaOH at 60 °C for 10 s, rinsed, sonicated in 1:1 $H_2O:HNO_3$ for 3 min, thoroughly rinsed again, and dried in an argon stream.

For one-side anodizing, a 250 mL-Teflon cell with a circular window with an area of 0.785 cm^2 at the bottom was applied to fix the sample with a silicon ring. The solution was thermostated and gently mixed. The platinum sheet was used as a cathode, and Hg/Hg_2SO_4 in the saturated K_2SO_4 solution was a reference electrode. Electrochemical investigations were carried out in the typical thermostated, three-compartment electrochemical cell equipped with a Pt counter, $Hg/HgSO_4/K_2SO_{4(sat)}$ reference, and Al working electrodes under conditions described in Table 2.1. A Zahner Zenium electrochemical workstation was used to control the potential and current generated. All potentials are presented in the SHE scale.

Table 2.1. Aluminum anodizing conditions in metavanadate-containing electrolytes

***C*(HCOOH), M**	***C*($NaVO_3$), M**	***C*(HCOONa), M**	**E_a, V**	**pH**
–	0.05–0.25	–	80	7.1–8.4
0.2–1.0	–	–	Constant current	1.8
0.5–1.0	0.2–0.25	–	80	2.5–3.0
1.0	0.01–0.25	0.1; 1.0	37	8.4

2.1.2. Aluminum anodizing in formic acid containing ammonium heptamolybdate and/or oxalic acid

The high-purity aluminum foil (99.99 wt. %, 100 µm thick, 20 × 20 mm, AlfaAesar) was used as a starting material. The aluminum specimens were pretreated in a hot solution of 1.5 M NaOH for 15 s, neutralized in 1.5 M HNO_3 for 2 min, then carefully rinsed in distilled water and air-dried. The samples were anodized from one side in the 0.4 M aqueous solutions of formic acid with additives of 1) 0.03 M $(NH_4)_6Mo_7O_{24}$ (pH 3.1); 2) 0.03 M $(NH_4)_6Mo_7O_{24}$ and 5, 10, 20 (pH ca. 3.0), and 100 mM (pH ca. 2.5) oxalic acid; 3) 20 mM oxalic acid (pH 1.65) in the thermostated two-electrode Teflon electrochemical cell (250 mL) in which the platinum grid was used as a counter electrode. A Viton O-ring set out the anodizing area of ca. 1.67 cm^2. First, the anodizing voltage (U_a) was gradually increased from 0 to 80 V for 10 min, and then samples were anodized at 80 V for 60 min. The temperature was maintained at a constant value (18.0 ± 0.1) °C by cryostat Lauda (WK 230). The anodizing process was controlled by a direct current power supply GW Instek (GPR-30H100). A Viton O-ring set out the anodizing area of ca. 1.67 cm^2. We also additionally obtained samples in the 0.4 M HCOOH with additives of 1) 0.03 M $(NH_4)_6Mo_7O_{24}$, 20 mM $H_2C_2O_4$; 2) 20 mM $H_2C_2O_4$ at 40 V (U_a was gradually increased from 0 to 40 V for 5 min, and then samples were anodized at 40 V for 55 min). The electrochemical cell described above was equipped with a Zanner Zhenium electrochemical workstation for this purpose. The temperature was maintained at a constant value (18.0 ± 0.1) °C by cryostat Lauda (WK 230). Finally, the samples were air-dried, and, if needed, aluminum was chemically etched in the solution containing $CuCl_2$ and HCl to investigate the anodic alumina's back side (i.e., anodizing front).

The ground for the choice of ammonium heptamolybdate as an additive to formic acid instead of sodium molybdate is that between the three most common Mo(VI) compounds, i.e., Na_2MoO_4, $(NH_4)_6Mo_7O_{24}$, and MoO_3, $(NH_4)_6Mo_7O_{24}$ exhibits the lowest toxicity [82]. Based on the results of optimizing aluminum anodizing in complex electrolytes containing formic acid and sodium metavanadate, we chose $(NH_4)_6Mo_7O_{24}$ concentration so that to get the same number of amount Mo in the final solution of $(NH_4)_6Mo_7O_{24}$ as in 0.2 M Na_2MoO_4.

During Al anodizing in the complex electrolyte containing HCOOH and $(NH_4)_6Mo_7O_{24}$, the heptamolybdate ions are reduced at the cathode to Mo_2O_3 (black layer covering platinum surface insoluble in water). The solution turned blue, indicating the formation of molybdenum blue, i.e., giant molybdenum oxide clusters belonging to the class of polyoxometalates. These clusters contain molybdenum atoms with oxidation states between +5 and +6 [83]. Therefore, not only heptamolybdate ions but also molybdenum species of different oxidation states adsorb at the anode surface and can take part in the anodizing process.

2.1.3. Titanium anodizing in ethylene glycol

Titanium plates (4 × 1 cm^2; 99.7 % Ti, Alfa Aesar) were polished mechanically and then chemically in $HF:HNO_3$ (1:2 vol.) mixture to mirror finish and finally rinsed with deionized water. According to [84], self-organized, highly ordered nanotubular titania layers were produced by two-step anodizing in ethylene glycol (EG) containing 0.75 % of NH_4F and 2 vol. % of H_2O. The anodizing voltage was increased from 0 to 40 V with a sweep rate of 200 mV s^{-1}, followed by a constant voltage process for 1 h. The oxide films formed during the first anodizing step were removed in an ultrasonic bath with deionized water. Before the second anodizing, the electrochemical cell was filled with a fresh electrolyte. After the second step, the samples were washed with ethanol, and then their surface was cleaned from debris by treatment in an ultrasonic bath with distilled water for 30 s. To obtain crystalline titania nanotubes, we annealed the samples at 450 °C for 1 h in air or 500 °C for 1 h in hydrogen.

2.1.4. Carbon component extraction from carbon-containing anodic alumina films

To obtain the carbon component from the samples, we dispersed the anodic alumina films formed in different electrolytes containing formic acid (see Section 2.1.2) and dissolved them in a hot (ca. 100 °C) aqueous solution of 0.1 M HCl. The solutions were dialyzed in SnakeSkin® 10 kDA for 24 h, centrifugated (Fisherbrand, 7000 rpm, 5 min), and filtrated (Q-Max® RR Syringe Filters 13 mm, 0.45 μm PTFE, hydrophobic). The pH of the final solutions was ca. 5–6 (Figure 2.1). Under laser irradiation, the Tindall effect occurs when the carbon phase is suspended in a slightly acidic aqueous solution. Moreover, under UV exposure (445 nm), solutions possess strong greenish fluorescence (Figure 2.1, F). These are evidence of the presence of nanosized particles in the solutions.

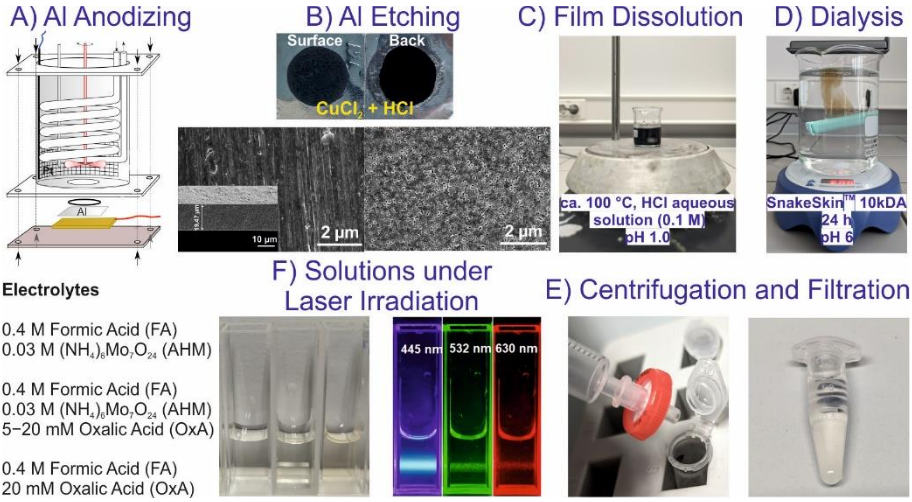

Figure 2.1. The schematic illustration for extraction of carbon components from carbon-containing anodic alumina films. Aluminum anodizing in different electrolytes containing formic acid (A), Al etching and SEM images of the films (B), film dissolution (C), dialysis of the solution (D), centrifugation and filtration (E), and final solutions under laser irradiation: 445 nm (blue), 532 nm (green), and 630 nm (red) (F).

2.2. Characterization techniques

2.2.1. Anodic alumina and anodic titania films

The morphology and cross section of anodized samples were studied from both sides of the film and in the cross-sections by *scanning electron microscopy (SEM)* using a SEM FEI Helios Nanolab 650 equipped with a field emission gun and EDX spectrometer. Cross sections were obtained by brittle cracking of the film via the bending of the sample over the blade of a knife. SEM images were further processed by the ImageJ software following the data processing procedure described by Vrublevsky et al. [85]. Since anodic Al_2O_3 is a non-conductive material, to study the membrane morphology (charge removal and screening of the incident beam from the charge accumulated in the volume of the material), a gold layer about 20 nm thick was deposited on the sample surface in a vacuum, which significantly increases the contrast of the electron microscope image. An SC7620 Mini Sputter Coater (Polaron) was used for sample preparation. The thickness of the coating deposited on the sample during the operation of the installation was determined by the formula:

$$d = 0.17IUt \tag{2.1}$$

where d is the thickness of the layer (nm), I is current through the gas discharge gap (A), U is the voltage applied to the gas discharge gap (V), and t is sputtering time (s).

The thickness of thin films formed by anodic treatments in the formic and vanadic acids alone was determined by analyzing the corresponding ellipsometry plots. Variations of Ψ and Δ parameters for nonporous alumina layers formed in the solutions of metavanadate were determined in the region from 200 to 1700 nm wavelengths by spectroscopic ellipsometry. The Bruggeman effective medium approximation was applied to calculate the optical constants and thickness of these films by fitting the model functions to the measured data using the Complete EASE software program.

The *linear sweep voltammetry (LSV) technique* was applied to characterize the electrochemical oxidation of aluminum in the aqueous solutions of 0.4 M HCOOH and in the mixture of 0.4 M HCOOH and 0.03 M $(NH_4)_5Mo_6O_{24}$ in the anodizing voltage (U_a) range of 0–100 V at 18 °C. The electrochemical cell described above equipped with a Zanner Zhenium electrochemical workstation was used for this purpose. The applied voltage was increased with a constant rate of 100 mV s^{-1}.

To determine the content of carbon-containing species entrapped in the anodic film, *thermogravimetry (TG)/differential thermal analysis (DTA) coupled with mass spectrometry (MS)* of evolved H_2O, CO_2, and CO gases were applied. The simultaneous thermal analysis apparatus STA Pt 1600 (Linseis, Selb, Germany) was used with the mass spectrometer MS Thermostar GDS 320 (Linseis/Pfeiffer, Asslar, Germany). For the investigation, the sample (19–22 mg) was loaded in Al_2O_3 crucibles and then heated in an argon (Ar 6.0) atmosphere up to 1300 °C at a heating rate of 10 $°C \cdot min^{-1}$. The data were collected and fitted using the software ‘Evaluation’ and ‘Quadera’ provided with the equipment.

Fourie-transformed infrared (FTIR) spectroscopy is a fast and reliable way to identify various functional groups: carbonyl, hydroxyl, and carboxyl; as well as various unsaturated fragments: double and triple carbon-carbon bonds, aromatic or heteroaromatic systems. FTIR measurements were performed using a Vertex 80v FTIR spectrometer (Bruker Inc., Ettlingen, Germany) equipped with a liquid nitrogen-cooled mercury-cadmium-telluride narrow band detector and transmission accessory. The spectrum was acquired from 64 scans with a resolution set at 4 cm^{-1} in the 800–4000 cm^{-1} spectral range. A HeNe laser ($P \leq 0.001$ W, $\lambda = 633$ nm) was used as a source. Data recording was performed using a two-channel delta-sigma analog-to-digital converter with a 24-bit dynamic range built into the preamplifier of the DLaTGS detector (DigiTect). It prevented signal distortion by external interference. Signal-to-noise ratio (minimum): at 5 s sample scan, reference signal > 7000:1 (6.2 × 10–5 AU noise) at 4 cm^{-1} resolution and standard optical components. The photometric error of the spectrometer is 0.01%. The air measurement was used as the background. The assignment of the bands was carried out, considering the data available in the literature [30,86,87].

X-ray photoemission spectroscopy (XPS) investigations were carried out to obtain information about the chemical states of carbon, aluminum, molybdenum, and oxygen in anodic alumina films both on the surface and back sides. An upgraded Vacuum Generator ESCALAB MKII spectrometer fitted with a new XR4 twin anode was used. The non-monochromatic MgK_α *X*-ray source was operated at $h\nu = 1253.6$ eV with 300 W power (20 mA/15 kV), and the pressure in the analysis chamber was lower than $5 \cdot 10^{-7}$ Pa during spectral acquisition. The spectra were acquired with an electron analyzer pass energy of 20 eV for narrow scans, a resolution of 0.05 eV, and a pass energy of 100 eV for survey spectra. All spectra were recorded at a 90° take-off angle and calibrated using the C 1*s* peak at 284.6 eV. Thermo VG Scientific provided the spectra calibration, processing, and fitting using Avantage software (5.918). In addition, *the X-ray-induced Auger electron spectroscopy (XAES) and Auger electron spectroscopy (AES)* measurements were performed to determine the *D* parameter from the C *KVV* spectra [88,89]. An Al K_α source, a constant analyzer pass energy of 100 eV for the survey and C *KVV* region and 20 eV for the elemental regions, and small-area lens mode A 3 × 12 with a diameter of about 3 mm were used. Auger electron spectra were acquired in the constant ratio mode CRR = 2 by the electron gun LEG200.

Diffuse reflectance spectra of films were studied by the Shimadzu UV-Vis-NIR Spectrophotometer UV-3600 coupled with the MRC-3100 unit. Measurements were performed by mounting a sample holder onto the integrating sphere. The measurable range of wavelengths falls between 200 and 850 nm, covering the UV and visible light regions. In the integrating sphere, one beam strikes the sample normally to the surface while the other beam aslant. Light absorbance was calculated from the diffuse reflection coefficient using the Kubelka–Munk function.

A femtosecond Yb:KGW oscillator was employed for the *time-resolved fluorescence measurements*. The third harmonic (343 nm, HIRO harmonics generator) of the light pulse oscillator (1030 nm, 80 fs at 76 MHz repetition rate) was used for fluorescence excitation. Laser light pulses were attenuated and focused into ~100 μm spot on the sample (average excitation power was about 1 mW mm^{-2}). A Hamamatsu streak camera was used for fluorescence detection with a system time resolution of about 10 ps.

The X-ray diffraction (XRD) measurements were carried out using a Philips *X*-ray PANalytical Empyrean diffractometer with CuKα radiation ($\lambda = 1.5406$ Å) in 2θ range of 20–40º. Crystalline phases were identified and indexed using *X*-ray Diffraction Philips Analytical software and the Pcpdfwin database – JCPDS-ICDD.

Most of the intermediates formed during electrochemical oxidation are also radicals. The presence of impurity defects, including paramagnetic ones, is also possible in nanoporous alumina. Therefore, *electron paramagnetic resonance (EPR) spectroscopy* can detect impurities and intrinsic defects in nanoporous carbon-containing anodic alumina. The EPR spectra were recorded at 77 and 298 K on a *VARIAN E* 112 spectrometer at 9.35 GHz (*X*-range). The power of the microwave radiation varied from 0.2 to 64 mW; the modulation amplitude was 0.05, 0.1, 0.2, and 0.4 mT at a modulation frequency of 25 kHz. The values of the *g*-factors and the concentration of paramagnetic centers (PCs) were determined relative to the reference samples: the *g*-factor relative to the position of the lines of hyperfine structure (HFS) of Mn^{2+}/MgO; the concentration of PCs (N_x) relative to a carbon standard using the equation as follows (the spectra of the samples and the standard were recorded under the same conditions):

$$N_x = N_{\mathrm{st}} \frac{I_x (\Delta B_x)^2}{I_{\mathrm{st}} (\Delta B_{\mathrm{st}})^2}, \tag{2.2}$$

where I is the intensity of the signal, and ΔB is its halfwidth.

EPR spectra were recorded directly from titanium plates with TiO_2 films deposited during the anodizing process. It was found that the presence of non-anodized titanium did not affect the spectrum parameters. The size and morphology of the nanotubes do not change after annealing in different atmospheres. However, untreated films were amorphous, while annealing in air at 450 °C and hydrogen at 500 °C led to anatase phase formation [84,90].

Besides the bare titania nanotubular films, samples covered with gold were obtained using a colloidal solution of gold nanoparticles with an average size of 5 nm. According to [91], after adding colloidal gold, the samples were successively dried in a vacuum and heated at 200 °C for 1 h. Thus, obtained films coated with Au were found to differ from the bare TiNT films by the electrocatalytic properties. In the present work, Au was introduced to the TiNTs to change their relaxation characteristics and, consequently, make it possible to register the EPR signals from Ti^{3+} ions and *F*-centers at 77 K. As is known, in crystallites with high symmetry, the signal from these centers can be registered at a very low temperature only (4 K). A decrease in the symmetry of the coordination surrounding can make it possible to record EPR spectra of titania at 77 K due to high non-stoichiometry or local lattice distortions caused by contact with the surface of Au nanoparticles [92]. The EPR spectrum of the A-12 graphene nanosized powder (GNP) (2 mg) was collected at 77 K using the microwave radiation power of 5 mW and the modulation amplitude of 0.2 mT.

The Raman spectra were recorded using a Nanofinder HE (LOTIS TII) confocal spectrometer). The registration of spectra was performed according to the scheme of backscattering, excitation radiation 532 nm, spectrometer resolution 2.5 cm^{-1}, optical power 2 mW, and diameter of the excitation laser beam 1 μm.

2.2.2.Carbon state characterization

Surface-enhanced Raman scattering was performed using a Renishaw InVia Raman (United Kingdom) spectrometer equipped with a thermoelectrically cooled (–70 °C) CCD camera and microscope. The continuous wave He-Cd Kimmon (Japan) laser emitting 442 nm wavelength light was used for the excitation via Leica 50×/0.75NA objective. The laser beam was focused on a 0.71-μm spot in diameter with an average power of 0.0264 mW at the sample and iteration time of 400 s. The Raman frequencies and relative intensities of Raman spectra were calibrated using the polystyrene standard ASTM E 1840 spectrum and luminescence of NIST Intensity Standard SRM 2241, respectively. Spectra were corrected using polynomial function background subtraction, and a binomial smoothing procedure was applied to the experimental data using the GRAMS/AI 8.0 (Thermo Electron Corp.) software. Carbon residuals were detected using silver nanoparticles (AgNPs) obtained by the synthesis protocol described previously [93]. The samples were mixed with AgNPs in a ratio of 5:1, applied on a stainless steel ‘Tienta’ substrate for Raman, and dried at room temperature. The procedure was repeated two times. Then, the samples were washed with Milli-Q water to remove the salts from sample solutions and impurities from the synthesis of the AgNPs.

The size distribution of CNPs was characterized by *transmission electron microscopy* (TEM, LEO-906E, Leica Microsystems GmbH, Germany). The *surface charge* was estimated by Zetasizer Nano ZS (Malvern Instr.) Data were analyzed using Malvern Zetasizer software 7.03.

Absorbance spectra of CNP solutions were measured in a 1-cm path-length quartz cuvette using UV-Vis spectrophotometer JASCO V-670 (Jasco Ltd., Japan). The optical density at the excitation wavelength was in the 0.01–0.9 range.

Fluorescence emission and fluorescence excitation spectra were performed using an Edinburgh Instruments FS5 spectrometer (Edinburgh Instruments Ltd., UK). Samples were excited by the 150 W CW Ozone-free Xenon arc lamp. The fluorescence was measured at 90° to the incident excitation beam. The range of excitation wavelengths was 280–450 nm, and fluorescence spectra were recorded in 400–700 nm spectral range with 0.5-nm and 0.2-nm slit for excitation and emission, respectively. CNP concentrations were held low enough to avoid the self-absorption effect with an absorbance value not exceeding ca. 0.2. The measurement error did not exceed 1–2%. All fluorescence spectra were corrected for instrument sensitivity.

Fluorescence time-decay kinetics were measured using a fluorescence lifetime spectrometer Edinburgh Instruments FL920 (Edinburgh Instruments Ltd., UK) under 375-nm picosecond laser diode excitation with pulse duration 57.3 ps, the repetition rate of 5 MHz (200 ns), pulse energy 140 μW. The fluorescence decay kinetics were approximated using one-component, two- or three-component exponentials considering the instrumental function with different characteristic decay times. The fitting procedure was done using Edinburgh F920 advances lifetime analysis software package with the following function:

$$f(t) = \sum_{i=1}^{3} B_i \exp\left(-\frac{t}{\tau_i}\right)$$

where τ_i is a characteristic lifetime, and B_i is a relevant pre-exponential factor. The goodness-of-fit parameter (χ^2) was around 1.

Biocompatibility assay. COS-7 cells (Cell line service, product number 605470) were grown in Ibidi high 8-well plate (Ibidi, catalog number: 80806) in DMEM medium (Gibco, catalog number: 31053028), supplemented with 10% fetal bovine serum (FBS) (Gibco, catalog number: A3840102) and Penicillin-Streptomycin (Gibco, catalog number: 15140122). $2.5 \cdot 10^4$ cells per well were seeded on the first day and grown in an incubator at 37 °C 5% CO_2. After 2 days, cells were washed 3 times with PBS (Gibco, catalog number: 10010023) and incubated with different concentrations of Qdots at 37 °C 5%

CO_2, which were diluted in FluoroBrite DMEM medium (Gibco, catalog number: A1896701) supplemented with 10% FBS, Penicillin-Streptomycin and GlutaMAX (Gibco, catalog number: 35050061). Before adding to the glass coverslip-adhered cells, all CNP stock solutions were filtered using a syringe filter containing 0.1 μm-sized pores (Whatman, catalog number: 6809-1012). Bright-field microscopy images of control and CNP-treated COS-7 cells were acquired at room temperature using a ZEISS Primovert inverted microscope equipped with ZEISS Axiocam ERc 5s camera and using a 10X objective, which is supplied as a pre-installed objective in the microscope's body. For the cell viability measurements, COS-7 cells, either untreated or incubated with respective concentrations of CNPs-1 or CNPs-2, after 10 h of overall incubation time, were initially washed 1 time with PBS (Gibco, catalog number: 10010023) and treated with 1X TrypLE Express (Gibco, catalog number: 12604013) for 5 min at 37 °C 5% CO_2. Then, the enzyme was inactivated by adding FluoroBrite DMEM medium (Gibco, catalog number: A1896701) into the wells, and the detached cells were centrifuged for 5 min at 200*g*. After centrifugation, the cell pellet was resuspended in 100 μL DMEM medium (Gibco, catalog number: 31053028), and 10 μL of the cell suspension was mixed with Trypan Blue Stain (Invitrogen, catalog number: T10282) to obtain a final 0.2% (*v*/*v*) concentration of the dye. Such samples were then analyzed using Countess II Automated Cell Counter that enabled the quantification of viable cells.

3. RESULTS AND DISCUSSION

3.1. Composition of metavanadate-containing electrolyte for obtaining carbon-functionalized porous alumina films

We suspect that the neutral and slightly acidic aqueous solutions might be prerequisites in constructing their electrolytes for Al anodizing due to the low solubility of vanadic acid. It is worth noticing that vanadic acid transforms to *meta* state in the acidic solutions, which further tends to polymerize into di-, tetra-, and decavanadic acids depending on the pH value [94]. The current transients, $J_a(t)$, (Figure 3.1, A), as well as anodic potential-time, $E_a(t)$, plots (Figure 3.1, B) recorded for Al anodizing in pure 0.2 M $NaVO_3$ solution, verified the formation of barrier-layer film [95].

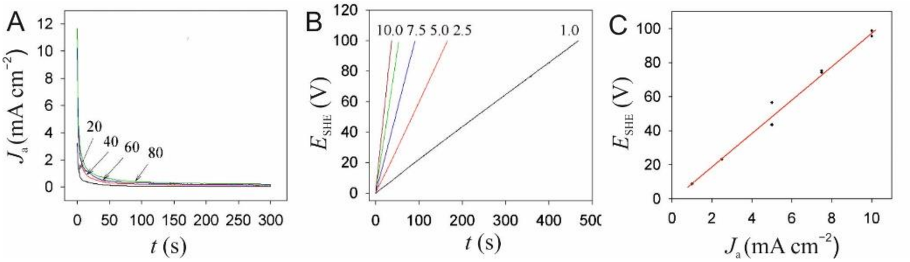

Figure 3.1. Current transience (A) and aluminum anodizing potential (B) with the processing time at the indicated voltage (A) and current density (B) values in 0.2 M $NaVO_3$, pH 7.1. In (C): Typical voltage-current plot for 0.2 M $NaVO_3$ slightly alkaline (pH 7.7) solution.

The thickness of this layer (δb) determined by ellipsometry was about 116–121 nm. The anodic oxidation rate for E_a = 80 V is 1.45–1.5 nm V $^{-1}$, close to 1.4 nm V $^{-1}$ characteristic of the barrier-layer alumina film formation. We also determined that for a given anodizing time, $E_a(t)$ plots are linear (Figure 3.1, C) with a slope that varies to some extent with the pH of the solution applied. For example, if the pH increased from 7.1 to 8.4, the slope of $E_a(J_a)$ plots decreased from $0.257 + 0.0005J_a^{-1}$ to $0.221 + 0.003J_a^{-1}$. We determined that a linear growth of alumina film at a constant current density proceeded up to 178–185 V. With further processing, the breakdown of the film began to cause an E_a drop of 163–167 V and oscillations.

We also studied the anodic behavior of aluminum in the aqueous formate solutions. From these investigations, several conclusions can be made: (i) the sudden increase in potential toward the maximum value at the onset of galvanostatic anodizing is characteristic of all the pH within the 1.8–8.4 range;

(ii) With further processing at a constant J_a, E_a decreased to approximately a similar value independent of the electrolyte pH. For example, at $J_a = 5$ mA cm^{-2} and pH 1.8, U_a stabilized at 24–20 V; (iii) Similar behavior has been estimated in the slightly alkaline solutions revealing a rapid E_a stabilization at some lower voltages, e.g., 20–21 V. In contrast, the E_a vs. t plots varied significantly in the slightly acidic solutions, not stabilizing for several minutes; (iv) The anodizing at a steady-state potential for hours resulted in the formation of porous anodic films just in the sub-micrometer thickness.

We investigated many process variations to optimize Al anodizing in the composite solution. It was established that adding just 0.01 M $NaVO_3$ to the HCOONa solution resulted in the steady-state anodizing potential increase from ca. 25 V to ca. 42 V (Figure 3.2, A). Further increase in $NaVO_3$ concentration to 0.2 M was ineffective (lines 3 and 4). From these, the concentration of formate is crucial for the anodic behavior of Al under the galvanostatic conditions; with the increase in the formate concentration, the growth of film after the barrier layer formation (signed by a star) proceeds further at growing potential with the decreasing rate (Figure 3.2, B). At constant voltage (Figure 3.2, C), an increase in $NaVO_3$ concentration just to 0.05 M resulted in J_a decrease during the first 100 s to a steady state without any fluctuations characteristic of pure formate solutions. Finally, it was determined that an increase in the $NaVO_3$ concentration in the mixed electrolyte of formic acid/sodium formate always resulted in an increase in alumina formation U_a and a decrease in the J_a, while the decrease in the pH of electrolyte led to film formation at a lower potential.

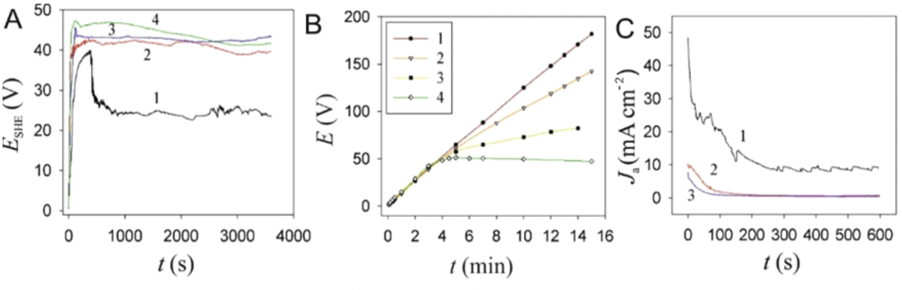

Figure 3.2. (A): E_a vs. t plots for 1.0 M formic acid solution containing 0 (1); 0.01 (2); 0.05 (3), and 0.2 M $NaVO_3$ at pH 2.6, $J_a = 5$ mA cm^{-2}. (B): The same at $J_a = 0.5$ mA cm^{-2} in the solution containing 0.25 M $NaVO_3$ without (1) and with 0.1 M (2) or 1.0 M HCOONa (3,4). pH: 8.4 (1–3) and 2.7 (4). (C): $J_a(t)$ plots in 1.0 M HCOOH + HCOONa solution: (1) without $NaVO_3$, (2) 0.05 M, (3) 0.2 M $NaVO_3$, pH 2.6, $E_a = 37$ V.

It was established that pH was a key parameter influencing the anodic film formation on the Al surface in the mixed electrolyte. Slightly colored films can be formed at pH 2.5–5.6 starting from 23 V. However, as-anodized films, even after 3–4 h of anodizing, remained nonuniformly colored in light tones. The films with khaki and black spots form at 35–38 V. The uniform and deep-colored finishing of the Al surface can be obtained within a wide range of anodizing voltages, e.g., at 40–180 V using 0.2–0.25 M $NaVO_3$ and 0.5–1.0 M HCOOH solutions at pH 2.5–3.0. For example, at 20 °C and 80 V, highly uniform thicknesses of ca. 40 μm and deep colored films were formed during 1 h. So, electrolyte composition was optimized to obtain uniform and deep-colored finishing of the Al surface in formic acid with sodium metavanadate additives.

3.2. Effect of sodium metavanadate additives on carbon-functionalized alumina films fabrication in formic acid solution

3.2.1. Surface characterization and structure

The structure of anodic films formed during 1 h at U_a = 60–100 V in the optimized composite solution (0.8 M HCOOH + 0.2 M $NaVO_3$) was studied. Figure 3.3 displays SEM images of the films obtained by the prolonged anodizing at 80 V. From these, the dense packaging of honeycomb-shaped cells was verified. The size and uniformity of cells at the metal|film interface varied significantly. The uniformity and order of cells seem to be poor for all tested U_a modes.

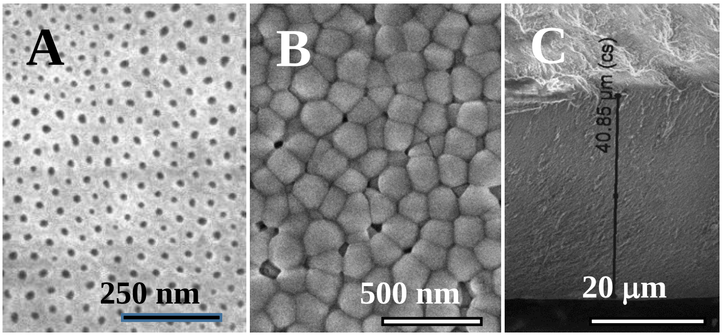

Figure 3.3. Top-side (A), back-side (A), and cross-sectional (C) SEM images of the anodic film formed by Al anodizing in the solution containing 0.8 M HCOOH + 0.2 M $NaVO_3$, 80 V, 20 °C, 1 h.

In addition, in the case of thinner films, the groups of obviously larger cells randomly distributed and uneven in size can be seen (Figure 3.4, A). A more detailed inspection of the areas with larger cells from both film sides revealed the formation of 2–3 times wider pores and two-fold film morphology after prolonged Al anodizing (Figure 3.4, B). The formation of films consisting of uneven and larger cells with wide pores at the Al|film interface and continuous upper and thick layers with three times thinner pores can be seen after the specimen bending and the cleavage of layers (Figure 3.4, B). We found that if during the first 2–5 min initiate anodizing at a lower voltage of 30–40 V, further increasing U_a to 60–100 V caused the formation of single-layered alumina films with quite uniform pores across all the film thickness and did not cleaved upon the specimen bending (Figure 3.4, C).

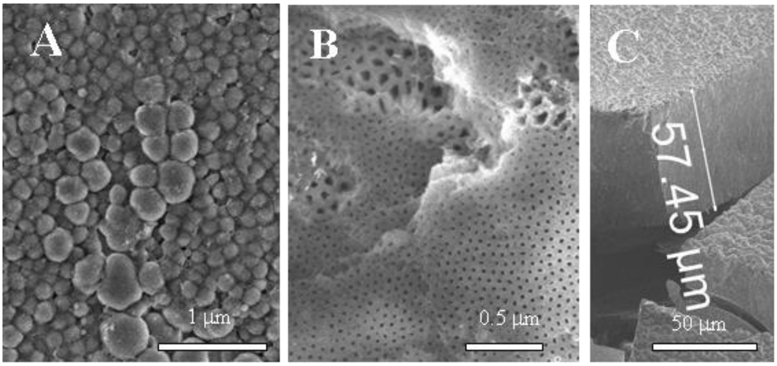

Figure 3.4. Back-side (A) and top-side (B) SEM images into the cleaved film surface of alumina film formed in the solution containing 0.8 M HCOOH + 0.2 M $NaVO_3$ at 60 V, 20 °C, 1 h.

3.2.2. Film composition depending on the anodizing voltage according to XPS studies

Chemical analysis using XPS indicated the presence of Al, O, V, and C elements. The quantification of XPS peaks of Al samples anodized in the optimized electrolyte (0.2 M $NaVO_3$ + 0.8 M HCOOH, pH 2.6) at 60, 80, and 100 V is presented in Table 3.1. According to these data, quite similar contents of elements were determined regardless of the U_a value. The oxygen content was 11–12% higher than required for Al_2O_3 and V_2O_5 stoichiometry, implying the inclusion of water molecules, COO^- and OH^- anions. The content of entrapped vanadium was low, ca. 2.5 at.%, insignificantly increasing with U_a value. Furthermore, a surprisingly high amount of entrapped carbon, ca. 17 at.%, was detected for all specimens, regardless of the anodizing voltage value. The observed phenomenon contradicted the well-known rule for incorporating electrolyte anions inside the outer layer of porous alumina films, postulating that the content of incorporated electrolyte anions should increase with anodizing voltage [32]. Of note, such a high content of carbon-containing species was observed on the surface of alumina films formed in tartaric acid solution at critical voltages and extremely high current densities [96]. The three peaks (Figure 3.5) with binding energies (BEs) of 515.39–515.66 eV, 516.54–516.84 eV, and 517.59–517.71 eV were attributed to V^{3+}, V^{4+}, and V^{5+} states, respectively [97]. Quantification of their peak areas revealed the dominant presence of V^{4+} ions, whereas the content of entrapped V^{5+} ions decreased with increasing U_a. So, the VO$_3^-$ ions are reduced at the cathode during Al anodizing. The solution turned blue, indicating the formation of V^{4+} species. Therefore, not only metavanadate ions but also vanadium species of different oxidation states, i.e., +3, +4, adsorb at the anode surface and penetrate the oxide.

Table 3.1. XPS data for anodic films obtained by Al anodizing in the solution containing 0.2 M NaVO$_3$ and 0.8M HCOOH at different U_a.

U_a, V	**Name**	**Peak, BE**	**FWHM, eV**	**Area (P) CPS, eV**	**Atomic %**	***Q***	**SF**
60	V2*p*	516.74	2.52	25150	2.26	1	6.330
	O1*s*	531.66	3.17	267785	53.51	1	2.850
	C1*s*	284.73	2.28	30885	17.08	1	1.000
	Al2*p*	74.24	2.04	28750	27.16	1	0.574
80	V2*p*	516.89	2.57	29080	2.45	1	6.330
	O1*s*	531.61	3.19	281965	52.80	1	2.850
	C1*s*	284.59	2.19	33005	17.11	1	1.000
	Al2*p*	74.19	2.09	31225	27.64	1	0.574
100	V2*p*	517.04	2.34	29354	2.71	1	6.330
	O1*s*	531.70	3.20	261951	53.75	1	2.850
	C1*s*	284.67	2.19	30490	17.31	1	1.000
	Al2*p*	74.27	2.03	27040	26.23	1	0.574

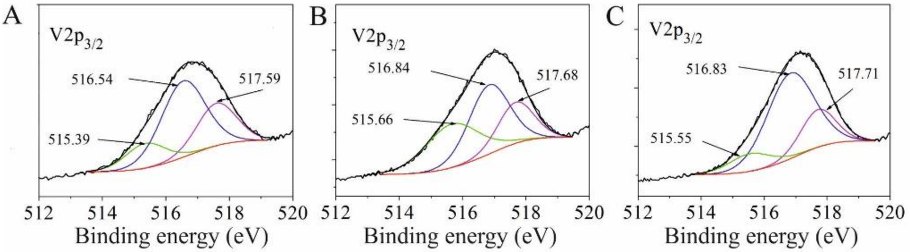

Figure 3.5. Deconvoluted V$_{2p}$ XP spectra of vanadium species entrapped inside the films fabricated by Al anodizing in the solution containing 0.2 M NaVO$_3$ + 0.8 M HCOOH at U_a: (A) 60, (B) 80, and (C) 100 V.

Deconvoluted O1*s* spectra were found to be described by three counterparts with BE peaks within 530.30–530.35 eV, 531.56–531.61 eV, and 532.73–532.90 eV ranges, corresponding to the BEs of oxygen in oxides, hydroxides, and carbohydrates, respectively [98].

3.2.3. Peculiarities of the carbon states depending on the anodizing voltage

For all specimens, the XPS spectra of C1*s* were deconvoluted into four counterparts (Figure 3.6) attributable to C–C, C–OH, C–O, and carboxylic O=C–O bonds with BEs of 284.49–284.60 eV, 285.68–286.03 eV, 286.72–287.13 eV, and 289.01–289.12 eV, respectively [88,89]. From the quantification of peak areas, most carbon-containing species could be ascribed to C–C bonds, while the smallest fraction of entrapped carbon was characteristic of C–O bonded species. Quantitative analysis data are presented in Table 3.2.

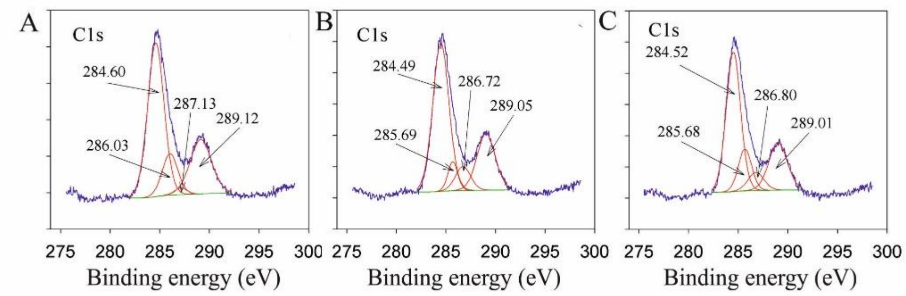

Figure 3.6. Deconvoluted C 1*s* XPS spectra of carbonaceous species entrapped inside the films obtained at U_a values of 60 V (A), 80 V (B), and 100 V (C).

Table 3.2. The relative proportions of carbon species according to C 1*s* spectrograms of the film fabricated as in Table 2.1

U_a, V	**C–C, C–H**	**C–OH**	**C–O**	**C–OOH**
60	0.572	0.146	0.019	0.263
80	0.589	0.070	0.090	0.253
100	0.539	0.149	0.077	0.235

Furthermore, the *D* parameter (the distance between the maximum of the positive-going excursion and minimum of the negative-going excursion in the first derivative XAES spectra) from C *KVV* spectra on the surface of the samples was equal to 20.4 eV, implying the predominance of carbon in sp^2 hybridization [88,89]. For the back side, $D = 12.8$–14.0 eV indicates the predominance of C sp^3 states. According to [7,8,38], the shift in the *D* parameter is the fingerprint of graphene. It is worth noting that, from the C1*s* deconvoluted areas, the content of carbon entrapped inside the anodic film in the C–C and C–H states was the highest among all carbon-containing species.

To determine the average content of carbon entrapped inside the anodic film formed in a solution containing 0.8 M $NaVO_3$ or 0.2 M $NaVO_3$ at 80 V for 1 h, the probe of this film with a thickness of ca. 42 μm was analyzed further by thermogravimetry analysis coupled with mass spectrometry up to 1000 °C. To determine the content of remaining carbon after the TG test in argon, we burned this probe in a synthetic air atmosphere by heating it to 1000 °C. According to Figure 3.7, the average amount of carbon in the film was approximated at 7.7 at.%, and it was removed from the film in the form of CO_2 and CO gases at about 900 °C. Furthermore, 94.8% of all carbon evolved during heating in an argon atmosphere. A relatively uniform distribution of carbon species in the film bulk was also elucidated by EDS mapping of carbon in the film cross section, evidencing the formation of a hybrid alumina/carbon material (Figure 3.8, C, E).

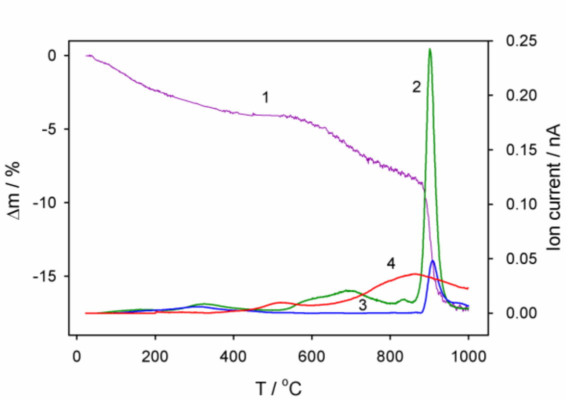

Figure 3.7. Variation of TG curve (1) and ionic currents of CO_2 (2) and CO species (3) during calcination of ca. 42 μm thick aluminum anodic film in an argon atmosphere up to 1200 °C and then in the synthetic air up to 1200 °C for the burning of remained carbon to CO_2 (curve 4, ×10). The anodic film was formed in 0.8 M HCOOH + 0.2 M $NaVO_3$ at 80 V, 1 h.

The large content of entrapped carbonaceous species in the anodic alumina films grown at 60–100 V was established for the first time. These species appear to be inserted into the alumina cell bulk during film growth, similar to that seen for structural ions in other electrolytes, coloring the film from grayish to black with increased anodizing time and film thickness. The main carbon source might be COO^- ions, supplied through the barrier layer during anodizing to the $Al|Al_2O_3$ interface with OH^-/O^{2-} ions. From the large content of carbon entrapped in the thin alumina films (5.8 at.%) formed in the formate solutions, it follows that formate ions were transported easily through the alumina barrier layer and reacted with Al^{3+} species at the $Al|Al_2O_3$ interface.

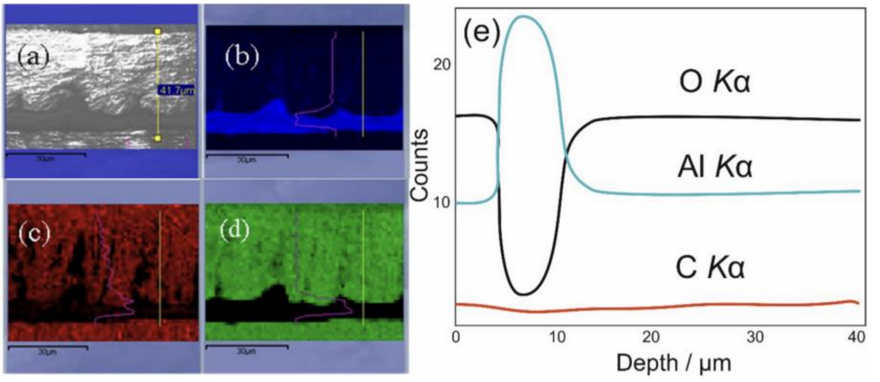

Figure 3.8. Cross-sectional image of anodic alumina/carbon composite film (A) and EDS mapping of aluminum (B), carbon (C), and oxygen (D) elements. (E) Cross-sectional distribution curves of oxygen, aluminum, and carbon elements in the film.

During aluminum anodizing in complex electrolytes containing formic acid and sodium metavanadate, nontypical alumina/carbon composite films are formed. This process was optimized by varying the concentration of both formic acid and sodium metavanadate, pH, and the processing time at the constant voltage (60–100 V). The anodizing conditions were critical in forming thick, nanoporous anodic films with a surprisingly high carbon content of about 17 at.%. Contaminations extracted from the XPS C 1*s* peak deconvolution showed that the main source of entrapped carbon is the carbon in sp^2 hybridization. However, vanadium(V) ions, as well as chromium(VI), are toxic. It would be logical to replace vanadates with nontoxic, more environment-friendly analogs of pentavalent vanadium ions, i.e., molybdate(VI) species (Table 3.3). So, it was the main reason for our further research. We continue our studies on the effect of $(NH_4)Mo_7O_{24}$ additives using optimized conditions for aluminum anodizing in complex electrolytes containing formic acid and sodium metavanadate.

Table 3.3. Toxicity data of the electrolyte components according to safety data sheets (Sigma Aldrich).

Compound	**CAS No**	***LD*** **LD_{50} (oral-rat), mg kg^{-1}**	**Carcinogenicity**	**Ecotoxicity**
CrO_3	1333-82-0	52	Carcinogenic	Discharge into the environment must be avoided
$NaVO_3$	13718-26-8	183	No data available	Do not empty into drains
$(NH_4)Mo_7O_{24}$	12054-85-2	> 2 000	No data available	Do not empty into drains

The results presented in Section 3.5.1 are summarized in a scientific article: Jagminas A, Klimas V, Chernyakova K, Jasulaitiene V. Designing carbon-enriched alumina films possessing visible light absorption, *Materials (Basel)* 15 (2022) 2700. doi: 10.3390/ma15072700.

3.3. Effect of ammonium heptamolybdate additive on aluminum anodizing in formic acid solution

3.3.1. Appearance, surface characterization, and growth of the anodic alumina films

The surface and back sides of the as-anodized anodic alumina films formed in the aqueous solution of 0.4 M HCOOH + 0.03 M $(NH_4)_6Mo_7O_{24}$ at 80 V are black (Figure 3.9). Very high current densities usually cause the formation of black anodic oxide films due to the strong electric field applied during anodizing, a phenomenon called “burning” [100]. Different reasons exist for the appearance of the black color in the porous anodic alumina films. So, Kikuchi et al. [101] obtained black films in croconic and rhodizonic acid solutions under burning conditions. Later, Pashchanka and Cherkashinin [102] synthesized optically black anodic alumina during anodizing in H_2SO_4 solution at 30–34 V, where no carbon sources were present, but the anodizing can be considered hard [103]. The authors explained the light-absorbing properties by the structural effects raised in disordered samples. The appearance of such color in our samples can be explained by carbonaceous species in sp^2 and sp^3 states embedded in the alumina structure. As the burning phenomenon was not observed, carbon is formed during the anodizing of valve metals through the oxidation of organic electrolyte components, for example, oxalates, malonates, and tartrates for aluminum anodizing [10,36], and ethylene glycol for titanium anodizing [64,65,104].

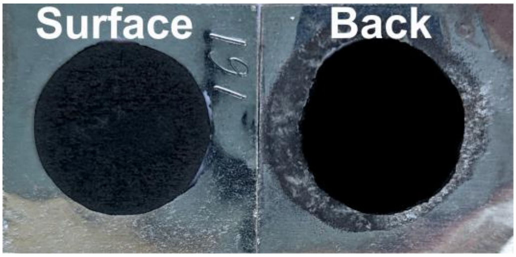

Figure 3.9. The surface appearance of the surface and back (i.e., anodizing front) sides of anodic alumina film formed in the aqueous solution of 0.4 M HCOOH + 0.03 M $(NH_4)_6Mo_7O_{24}$ at 80 V, 18 °C, 1 h.

The characteristic morphology of anodic oxide films formed by Al anodizing in an aqueous solution of formic acid with ammonium heptamolybdate additive under constant bath voltages from 60 to 100 V possesses a hierarchical structure with multi-branched pores (Figure 3.10 and Figure 3.11). The film in the hillock sites is crushed. An increase in the anodizing time increases the size and height of hillocks where numerous terraces with the processing time increase are formed (Figure 3.10, C). In contrast, the morphology of the sample back side resembles the porous structure of these films, similar to the porous structure of alumina grown in the tartaric or oxalic acid electrolytes at higher voltages [49,105]. A highly waved $Al|Al_2O_3$ interface is formed (Figure 3.11, A). The back-side film interface SEM observations also revealed the formation of hexagonal-shaped cells at the metal|oxide interface with an average diameter of about 180 nm (Figure 3.11, B), which agrees with D_{inter} for anodizing in 0.3 M oxalic acid [106]. If we apply the equation, $D_{\text{inter}} = 2.41U_a + 3.5$, we get 196.3 nm. However, these cells are packed less tightly than oxalic acid films. The clefts are viewed between the cells and their groups (marked with red arrows in Figure 3, B).

The surface and cross sections of the resulting films look different from the porous alumina formed in other carboxylic acids [5]. For anodizing in formic acid with ammonium heptamolybdate additive, porous alumina with a thickness of about 20 μm is formed at 80 V in 1 h. However, the ordered porous structure is absent, and the thin, cracked cover layer on the film surface occurs (See Figure 3.10, A–C).

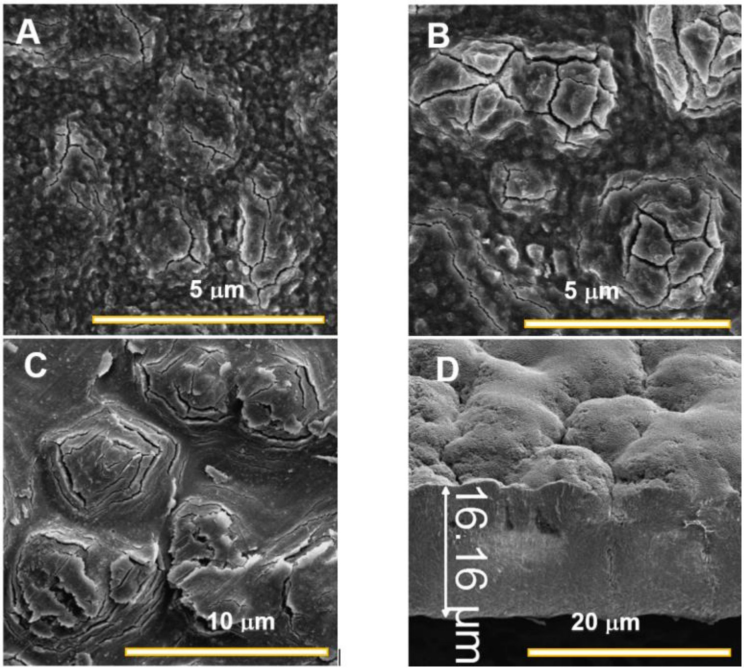

Figure 3.10. SEM images of the surface (A–C) and cross section (D) of anodic alumina film formed in the aqueous solution of 0.4 M HCOOH + 0.03 M $(NH_4)_6Mo_7O_{24}$ at 80 V, 18 °C for 2 (A), 10 (B), and 60 min (C, D).

The current transients of anodic alumina formation in 0.4 M HCOOH + 0.03 M $(NH_4)_6Mo_7O_{24}$ do not depend on U_a (Figure 3.12). After the process starts, in ca. 12 min, the current gradually decreases from the initial 60 mA cm^{-2} to 3.5 mA cm^{-2}, and then it stays almost constant. It is not a typical steady-state porous aluminum anodizing if compared with anodizing in other carboxylic acids [5]. It can be characteristic of non-steady-state processes during which anodic alumina films with tree-like or multi-branched, porous structure was formed [15,107]. In a non-steady state of anodizing, the oxide formation and dissolution rates never reach equilibrium. Negative charges from oxygen-containing species will accumulate in the oxide layer up to an accumulative threshold charge. Then, discharging of the negatively charged oxide layer will occur, leading to the generation of nonuniform current pathways running through the oxide, resulting in the formation of branched pores. Gong et al. [108] showed that a porous alumina layer could be formed under the dense cover layer and explained their results using the oxygen bubble model [109,110]. According to ionic and electronic current theories, one of the reasons for forming porous anodic alumina is the oxide flow around the oxygen bubble. After a short time, oxygen bubbles grown between the interface of the barrier oxide layer and the anion-contaminated layer have not yet evolved from the surface. Therefore, porous anodic alumina embryos are formed. The expansion of oxygen bubbles also can cause the formation of cavities [108,111]. At the same time, many bubbles formed during anodizing can change the current distribution on the surface of the oxide film, leading to a lower heat transfer rate between the electrolyte and the reaction surface. Moreover, HCOOH species are also absorbed in the growing alumina and can be decomposed in one of the possible ways [112], resulting in CO and CO_2 formation. Due to local overheating, they can also disproportionate into carbon through dissociative adsorption, decarboxylation, dehydrocyclization, and polycondensation reactions [113–116]. The intensive gas evolution can also explain the irregular, rough, hierarchical structure with multibranched pores [117].

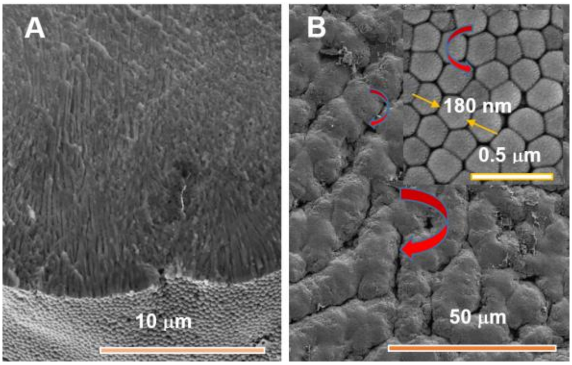

Figure 3.11. Cross-section (A) and back side (B) SEM views of anodic film fabricated in the aqueous solution of 0.4 M HCOOH + 0.03 M $(NH_4)_6Mo_7O_{24}$ at 80 V, 18 °C, 1 h.

As seen in Figure 3.12, inset, the LSV curves of aluminum anodizing in 0.4 M HCOOH and 0.4 M HCOOH + 0.03 M $(NH_4)_6Mo_7O_{24}$ are also different from that of typical porous anodizing in oxalic acid in which the current growths exponentially [118–120]. As mentioned, Al anodizing in formic acid is hardly possible and requires special conditions, so the LSV curve has one linearly increasing region at 25–55 V, corresponding to the beginning of local and pitting corrosion on the Al surface. Nevertheless, the situation changes if ammonium heptamolybdate is added to the formic acid solution: current overshoot at U_a = 53–67 V is observed. In the LSV curve, up to 53 V, the anodizing current does not change and equals 1.0–2.0 mA cm^{-2}. Then, one can observe current growth from 2.0 to 60 mA cm^{-2} in the voltage range of 53–67 V and subsequent current decay to 20 mA cm^{-2} at 67–100 V. Previous investigations of aluminum alloys anodizing in the mixture of sulfuric and tartaric acids with molybdate additives [55,57,58,121] show that low molybdate concentrations slightly hindered film formation. On the contrary, a concentration higher than 0.1 M improved the film formation. Molybdate ions do not affect the oxide formation. However, they can change the double-layer structure and prevent or partially stop the initial corrosion. Anodic alumina formation starts when the potential of formic acid oxidation is reached (the current overshoot in the LSV curve (See Figure 3.14)). Molybdate ions, as well as vanadates [122], can also form the nonporous oxide on the surface of the aluminum and thus prevent its dissolution at the beginning of the process. It can explain the formation of the thin, cracked layer sites on the film surface.

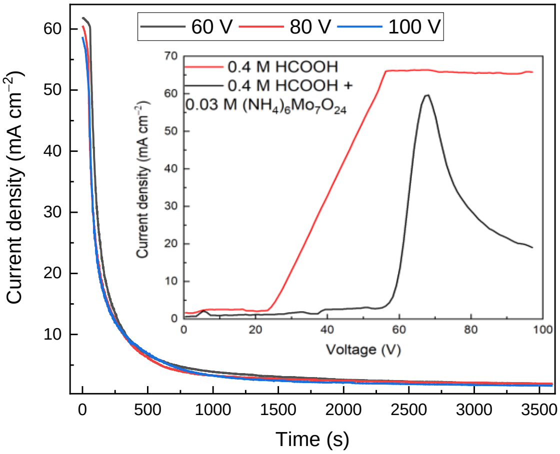

Figure 3.12. Current transient curves of anodic alumina formation in 0.4 M HCOOH + 0.03 M $(NH_4)_6Mo_7O_{24}$ at 60–80 V, 18 °C. Inset shows linear sweep voltammograms for Al anodizing in aqueous solutions of 0.4 M HCOOH and 0.4 M HCOOH + 0.03 M $(NH_4)_6Mo_7O_{24}$, 18 °C recorded at the voltage sweep rate of 0.1 V s^{-1}.

3.3.2. Composition of the anodic alumina film in terms of carbon state and content

To characterize anodic alumina formed in formic acid with ammonium heptamolybdate additive over a broad temperature range and determine the average carbon content in the films, we applied TG/DTA analysis coupled with mass spectrometry up to 1300 °C in the Ar atmosphere (Figure 3.13). In the temperature range of 30–400 °C, dehydration, dihydroxylation, and decarboxylation processes take place, that is, the removal of chemically adsorbed water and hydroxyl species along with the evolution of physically adsorbed CO_2 and CO [123]. At 500–850 °C, the transition of amorphous alumina to γ-Al_2O_3 and partial evolution of CO_2 and CO (most likely resulting from CO_2 and CO adsorbed inside the film) occur [11,30]. Then, at 860 °C (the exothermic first peak in the DTA curve), the θ-Al_2O_3 formation starts, and most carbon from carboxylate ion decomposition is removed from the film [30], [124]. At 1115 °C (the second exothermic peak in the DTA curve), the α-Al_2O_3 appears, and the rest of the carbon is deleted (CO_2 and CO emission peak at 1115–1200 C°). According to TG analysis, the average carbon content is ca. 5.5 mass.%, 2.2 and 1.7 times higher than in oxalic and tartaric anodic alumina films [11,30]. Heating in the Ar atmosphere to 1320 °C removes all the carbon in the sample. There are no traces of CO_2 in the $m/Z = 44$ ionic current curves recorded during the additional combustion of the sample in the synthetic airflow. It means that all the carbon embedded in the alumina is in the form of CO_2, CO, carboxylate ions, and *a*-C:H.

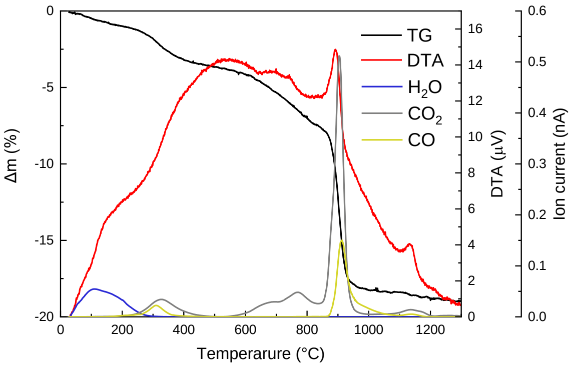

Figure 3.13. TG/DTA plot and evolved gas analysis for anodic alumina film formed in the aqueous solution of 0.4 M HCOOH + 0.03 M $(NH_4)_6Mo_7O_{24}$ at 80 V, 18 °C, 1 h.

FTIR spectroscopy also confirms the complex composition of the anodic alumina films obtained and entirely agrees with TG/DTA data (Figure 3.14). In the spectrum of the film, one can find the bands caused by *amorphous alumina* – intense two absorption bands with maxima at 810 and 910 cm^{-1} and a weak absorption band at 1150 cm^{-1} in the typical vibration region of Al–O [125]; *chemisorbed carboxylate and carbonate ions* – intense unresolved broad band at 1250–1750 cm^{-1} caused by C–O stretching vibration [36]; *chemisorbed CO and* CO_2 *molecules* – weak band centered at ca. 2132 cm^{-1} and strong band at ca. 2340 cm^{-1} due to C–O and C=O stretching vibration, respectively [126]; embedded in the alumina structure *a-C:H* – a complex of broad unresolved bands in the 3100–2850 cm^{-1} region caused by C–H stretching modes (See Figure 3.14, inset). There are –C–H_n modes at 2850–2970 cm^{-1} (namely, 2850 cm^{-1} (sp^3CH_2 sym.), 2875 cm^{-1} (sp^3CH_3 sym.), 2930 cm^{-1} (sp^3CH_2 asym.), 2960 cm^{-1} (sp^3CH_3 asym.)) and =CH_n modes lying at 2975–3100 cm^{-1} (namely, 2975 cm^{-1} (sp^2CH_2 olef. sym.), 3025 cm^{-1} (sp^2CH aromatic)) [78]; *chemisorbed hydroxyl groups* – broad band at 3200−3600 cm^{-1} caused by stretching vibrations of O−H groups adsorbed on the surface and in the bulk of alumina. The presence of carbon atoms in different states is characteristic of carbonaceous species in different hybridization states, e.g., *a*-C:H, embedded in the alumina structure, not the graphene-like carbon clusters [10].

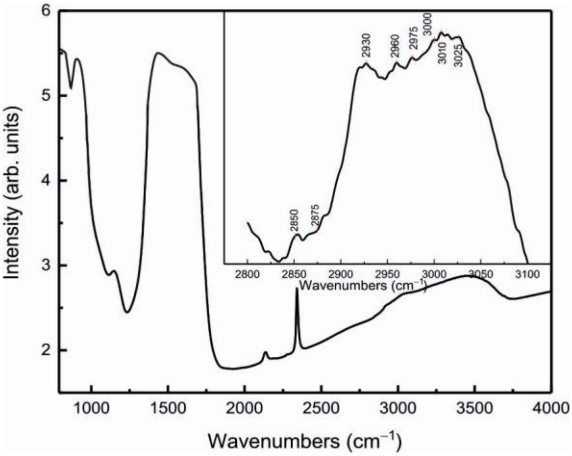

Figure 3.14. FTIR spectrum of anodic alumina film formed in the aqueous solution of 0.4 M HCOOH + 0.03 M $(NH_4)_6Mo_7O_{24}$ at 80 V, 18 °C, 1 h. The inset shows the absorption maxima in the C–H stretching modes.

The structure and properties of *a*-C:H strongly depend on the ratio of carbon atoms in sp^2 and sp^3 hybridization. Evaluating sp^2 and sp^3 content in the *a*-C:H using IR spectroscopy is unreliable, as the oscillator strength of the various C–H modes is not constant [78]. IR spectroscopy can only provide information about the carbon state in the bulk of samples, and it is impossible to investigate the surface and back sides of the films separately. For this purpose, a XAES study of the anodic alumina films obtained at 60–100 V was carried out on both sides of the samples to determine the *D* parameter from C *KVV* spectra. As can be seen from Figure 3.15, U_a does not affect the state of carbon in the films (similar to the metavanadate-containing electrolyte). However, the difference is very noticeable for the surface and back sides. On the surface, the *D* parameter is equal to 21.4 eV. On the back side, it is 17.0 eV for 60 and 80 V and 16.2 eV for 100 V. According to Lascovich et al. [127], the *D* parameter for C sp^3 is 13.2 eV and 23.1 eV for C sp^2 hybridization, and the increase in *D* is associated with the growing number of pπ electrons or sp^2 sites in the films. It was shown during the investigation of thin films of hydrogenated amorphous carbon that induced disorder gives rise to the surface mainly of sp^2 sites; on the other hand, oxidation of amorphous carbon increases the number of sp^3 sites resulting from attaching additional oxygen groups (C−OH, C−OOH) [128].

XPS also confirms this result (Table 3.4). On the surface, O/Al and C/Al ratios almost do not depend on the U_a and are in the range of 2.29–2.35 and 0.46–0.58, respectively. On the back side, these ratios increase for U_a equal to 60 and 80 V compared with the surface; O/Al becomes 2.51–2.55, and C/Al = 0.72–0.79. In the case of 100 V, O/Al equals 2.27, and C/Al = 0.97.

Table 3.4. XPS data for O/Al, C/Al, and C/O ratio on the surface and back sides of the porous alumina film formed in the aqueous solution of 0.4 M HCOOH + 0.03 M $(NH_4)_6Mo_7O_{24}$ at 60–100 V.

Element ratios	**Anodizing voltage, V**		
	60	**80**	**100**
Surface side			
O/Al	2.35	2.34	2.29
C/Al	0.46	0.57	0.58
C/O	0.20	0.24	0.24
Back side			
O/Al	2.55	2.51	2.27
C/Al	0.72	0.79	0.97
C/O	0.28	0.32	0.43

For stoichiometric Al_2O_3, O/Al ratio is 1.5. First, the number of O atoms exceeds the needed for the oxide formation, and consequently, the rest of the atoms are bonded with carbon and hydrogen, which agrees with TG/DTA and FTIR data. Second, one can see that the number of Al atoms decreases, and the number of C atoms increases from the surface to the backside (i.e., anodizing front). It also supports the idea that electrolyte species are adsorbed at the $Al_2O_3|Al$ interface.

The higher carbon content on the back side of this film compared with the samples obtained at 60 and 80 V can be explained by the fact that when anodizing takes place at 100 V, the initial stage lasts up to 100 V (See Figure 3.12, inset). It means that the process starts at the end of the LSV curve, i.e., the maximum possible amount of formate ions delivered to the $Al_2O_3|Al$ interface.

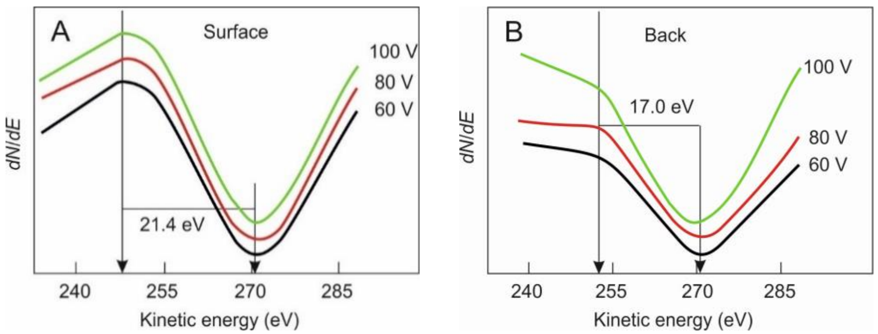

Figure 3.15. Derivative dN/dE XAES spectra of surface (A) and back (B) sides of porous alumina film formed in the aqueous solution of 0.4 M HCOOH + 0.03 M $(NH_4)_6Mo_7O_{24}$ at 60–100 V, 18 °C, 1 h.

Comparing FTIR spectra, D parameter determined from XAES data of porous alumina obtained in the aqueous solution of 0.4 M HCOOH with ammonium heptamolybdate additive and that of porous alumina formed in the aqueous solution of 0.4 M tartaric acid [11,12,49] with other organic acids [36,37,129] does not show any significant differences. So, regardless of the initial organic acid chosen for anodizing, the products of electrochemical oxidation of aluminum in the carboxylic acids are very similar. The difference is only in the driving power of the processes. Anodizing in tartaric acid and other carboxylic acids is a high-field process, i.e. it takes place at voltages above 100 V, during which a huge amount of Joule heating is evolved, and it causes carbon formation. In the case of formic acid with heptamolybdate additives, anodizing occurs at 60–100 V, and carbon formation is due to local overheating caused by the gas bubbles from water and formic acid oxidation. Another reason for this process is that heptamolybdate ions change the double-layer structure at the electrolyte|oxide interface, inhibiting aluminum dissolution and promoting oxide growth. Moreover, the carbon content is higher in this case, and the anodizing voltage is much lower than in the case of the formation of carbon-containing alumina in other carboxylic acids.

However, according to SEM results (See Figure 3.10 and Figure 3.11), the films have hillocks and are crushed. An increase in the anodizing time increases the size and height of hillocks where numerous terraces are formed. A strongly wavy interface between the film and aluminum is also observed, indicating high inhomogeneity of the film morphology. However, this problem can be solved by adding small amounts of oxalic acid to the anodizing solution. As earlier, it was shown that oxalic acid additives affected the electrochemical oxidation process of aluminum in sulphuric acid solution, leading to the formation of a more compact oxide layer and improvement of film growth and their mechanical properties [24,54].

The study results were summarized in a scientific article: K. Chernyakova, V. Jasulaitiene, A. Naujokaitis, R. Karpicz, I. Matulaitiene, V. Klimas, A. Jagminas, Aluminum anodizing in an aqueous solution of formic acid with ammonium heptamolybdate additive, *J. Electrochem. Soc.* 170 (2023) 013501. DOI: 10.1149/1945-7111/acb019.

3.4. Effect of oxalic acid additives on alumina growth in formic acid containing ammonium heptamolybdate

3.4.1. Peculiarities of alumina growth depending on the concentration of oxalic acid

The effect of oxalic acid additives in concentrations ranging from 5 to 100 mM on the electrochemical aluminum oxidation in an aqueous solution of 0.4 M HCOOH with and without 0.03 M $(NH_4)_6Mo_7O_{24}$ was studied. The purpose of using the mixture of formic and oxalic acids (without $(NH_4)_6Mo_7O_{24}$) as an anodizing electrolyte is to eliminate the effect of molybdate ions on the growth kinetics of porous alumina and compare it with the process when the mixed solution is used. Moreover, it was demonstrated that organic additives, such as glycolic acid, oxalic acid, and glycerol, are adsorbed at the oxide/electrolyte, exerting a strong influence on the porosity, density, and tribology properties of the oxide film [24]. As can be seen from the current transients (Figure 3.16), adding oxalic acid, ammonium heptamolybdate, or their mixture does not significantly change the aluminum anodizing kinetics in formic acid in contrast to the effect that the addition of ammonium heptamolybdate to a pure solution of formic acid had when the local and pitting corrosion of the Al foil was prevented, and the formation of thick porous layer became possible (see Section 0). Up to 50 V, anodizing current density (J_a) increases to 6.0 mA cm^{-2}. Then, one can observe sharp J_a growth from 6.0 to ca. 65 mA cm^{-2} in the 50–65 V voltage range with subsequent current decay to 30–35 mA cm^{-2}. Then, the U_a was kept at 80 V for 1 h, and during the next 30 min, the current gradually decreased to 7–8 mA cm^{-2}, staying constant until the end of the process. The situation with the electrolyte containing 0.03 M ammonium heptamolybdate and 100 mM oxalic acid is slightly different: current overshoot maximum shifts to 80 V and is not so pronounced (J_a(max) is about 25 mA cm^{-2}). However, the shape and tendency in growth kinetics of the film remain the same. As shown in Figure 3.16, LSV curves look almost the same regardless of electrolyte composition.

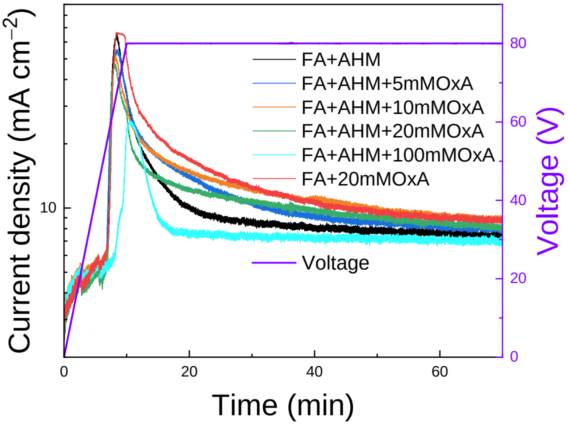

Figure 3.16. Chronoamperograms of anodic alumina formation in a 0.4 M HCOOH (FA) containing 0.03 M $(NH_4)_6Mo_7O_{24}$ (AHM) and different amounts of $H_2C_2O_4$ (OxA), 18 °C. U_a was gradually increased from 0 to 80 V for 10 min, and then samples were anodized at 80 V for 60 min.

Therefore, to explore the oxide growth at the initial stages, i.e., before the current overshoot, we obtained anodic alumina films in the 0.4 M HCOOH with additives of 1) 0.03 M $(NH_4)_6Mo_7O_{24}$, 20 mM $H_2C_2O_4$; 2) 20 mM $H_2C_2O_4$ at 40 V (Figure 3.17). When the U_a was increased from 0 to 40 V, the J_a increased to 5–6 mA cm^{-2} and stayed constant during the process; the current overshoot was not observed (Figure 3.17, A). Anodizing at 40 V formed a thin, transparent porous alumina layer with tiny disordered pores on the aluminum surface (Figure 3.17, A, insets).

The film formed in the electrolyte containing $(NH_4)_6Mo_7O_{24}$ and $H_2C_2O_4$ was so thin that it could not be separated from the Al substrate. The thickness of the oxide layer obtained in the mixture of formic and oxalic acids for 1 h was 1.70 μm, and the film possessed a hierarchical structure with multi-branched pores (Figure 3.17, B). In Section 0, we investigated the process after the current overshoot, i.e., at $U_a = 60–100$ V, and showed that it corresponded to the beginning of electrolyte oxidation and increasing rate of alumina formation. So, one can conclude that a thin film consisting of pure alumina should form on the surface of the samples at the initial stage of Al anodizing in the mixed electrolyte containing formic and oxalic acids with or without ammonium heptamolybdate additive.

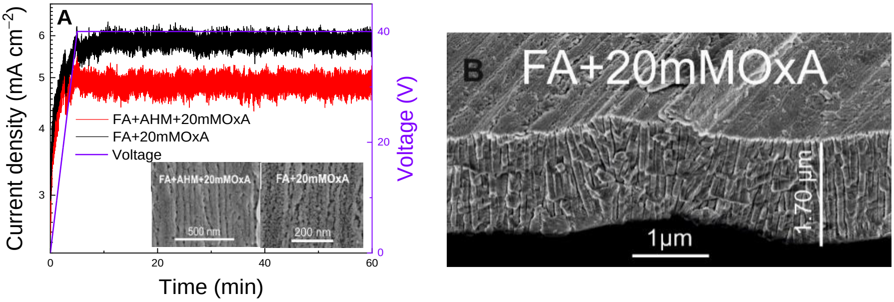

Figure 3.17. Chronoamperograms (A) for anodic alumina formation in a 0.4 M HCOOH (FA) containing 1) 0.03 M $(NH_4)_6Mo_7O_{24}$ (AHM) + 20 mM OxA and 2) 20 mM $H_2C_2O_4$ (OxA), 18 °C. U_a was gradually increased from 0 to 40 V for 5 min, and then samples were anodized at 40 V for 55 min. Insets show SEM images of the surface of the anodic alumina films. Cross section (B) of the anodic alumina film formed in a 0.4 M HCOOH + 0.03 M $(NH_4)_6Mo_7O_{24}$ + 20 mM OxA at 40 V (black curve in A).

3.4.2. Surface characterization and structure depending on the concentration of oxalic acid

The characteristic morphology of anodic oxide films formed by Al anodizing in an aqueous formic acid solution with ammonium heptamolybdate and oxalic acid additives possesses a hierarchical structure with multi-branched pores (Figure 3.18). First, let us consider the series of electrolytes containing 0.4 M HCOOH + 0.03 M $(NH_4)_6Mo_7O_{24}$ with oxalic acid additives (5–100 mM). The film obtained in electrolyte with 5 mM $H_2C_2O_4$ is crushed in the hillock sites. A highly waved interface between the film and aluminum is formed. The thickness of the film formed at 80 V for 120 min varies from 16.92 to 18.19 µm (Figure 3.18, A, inset). Adding 10–20 mM of oxalic acid improves the film surface significantly: hillock sites almost disappear as well as the waved interface does. Film thickness does not change throughout the sample and is 19.47 µm. On the back side of the film, hexagonal-shaped cells are formed at the Al|Al_2O_3 interface with an average diameter (D_{inter}) of about 190–200 nm (Figure 3.18, C, B, D), which agrees with D_{inter} for anodizing in 0.3 M oxalic acid [106]. Applying this equation, $D_{inter} = 2.41U_a + 3.5$, we get 196.3 nm. However, these cells are packed less tightly than in oxalic acid films. Adding 100 mM of oxalic acid changes the situation radically. The interface between the film and aluminum becomes extremely waved; the film thickness changes from 5.58 to 15.36 µm, although the surface remains porous (Figure 3.18, E). The back side is also nonuniform;

huge hillocks ca. 10–15 μm in height and ca. 5 μm in diameter can be observed (Figure 3.18, F).

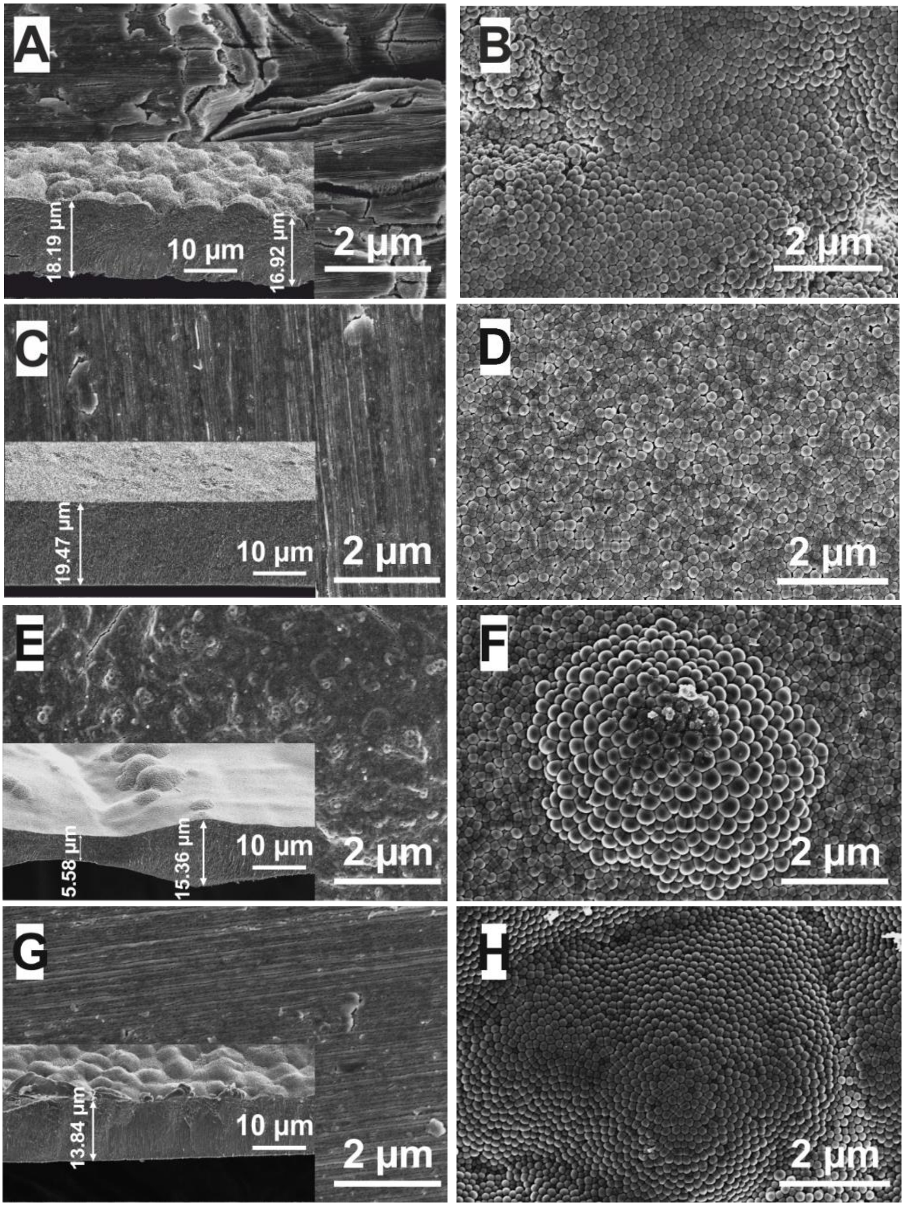

Figure 3.18. SEM images of surface sides (A, C, E) and back sides (B, D, F) of anodic alumina film formed in the aqueous solution of 0.4 M HCOOH with additives of 1) 0.03 M $(NH_4)_6Mo_7O_{24}$ + 5 mM $H_2C_2O_4$ (A, B); 2) 0.03 M $(NH_4)_6Mo_7O_{24}$, + 20 mM $H_2C_2O_4$ (C, D); 3) 100 mM $H_2C_2O_4$ (E, F); 4) 20 mM $H_2C_2O_4$ (G, H) at 80 V, 18 °C. Insets show the cross sections of the films.

Second, let us consider adding 20 mM of oxalic acid to the 0.4 M formic acid solution. Adding oxalic acid also promotes the formation of a thick porous alumina film contrary to the pure formic acid solution. However, compared with the ammonium heptamolybdate additive (see Section 0), it improves the surface morphology of the sample, removing the hillocks, but the back side still possesses a wavy interface. The sample thickness is 13.84 µm (Figure 3.18, G). The back side is also nonuniform, but hexagonal-shaped cells are formed at the Al|Al_2O_3 interface with a D_{inter} of about 170 nm (Figure 3.18, H). Compared with the case of ammonium heptamolybdate and/or oxalic acid additives, the sample thickness is about 25% less, and D_{inter} is 15 % less. So, regardless of the similarities in the shape and behavior of anodizing kinetics, SEM studies indicate differences in forming the films in formic acid solutions without molybdates.

3.4.3. Model for the anodic alumina film formation in the presence of ammonium heptamolybdate and oxalic acid

Thus, a thin porous alumina film similar to that obtained in pure formic acid solutions [53] is formed at the beginning of the process (Figure 3.19). Then, when the electrolyte oxidation potential is reached (at ca. 50 V), the thin film on the surface breaks, resulting in a significant increase in the anodizing surface, and anodic oxide begins to grow rapidly (current overshoot at 50–65 V). It should be noted that the anodizing kinetics at the beginning of the process, when the U_a was increased, in our case, significantly differs from the typical porous anodizing in oxalic acid in which the current grows exponentially [118,119,130]. When the U_a reaches 80 V, the process becomes very similar to the hard anodizing in oxalic acid, where the current decreases with the increasing thickness of the alumina layer [119,130,131]. It is also evident that the process of Al oxidation in these electrolytes is non-steady and results in the formation of anodic alumina films with tree-like or multi-branched, porous structure [15,107]. Gases evolving during electrolyte oxidation and rapid alumina growth can cause the appearance of hillocks and cracks on the surface (see Figure 3.19), and it could be the reason for the formation of the irregular, rough, hierarchical structure with multi-branched pores [117]. Adding oxalic acid to the formic acid solution containing ammonium heptamolybdate improves anodic film growth, increasing the film thickness and smoothing its surface and back sides (see Figure 3.18). This result agrees with data obtained for Al anodizing in the oxalic acid–sulphuric acid mixture [24,54]. As was shown, when organic compounds and/or molybdates were added to the sulfuric acid solution, oxalate ions, as well as molybdates, can not only reduce the dissolution rate during aluminum anodizing [54,55,57,58] but also inhibit the chemical dissolution of pore walls by adsorbing and changing the double-layer structure at the oxide|electrolyte interface [24,59]. So, it can explain the similarities in the shape of current transients regardless oftabf the electrolyte composition. Considering current transients and SEM data, the shift of the overshoot potential to the higher voltage when 100 mM of oxalic acid is added can be explained by the competition of oxalate and formate ions during oxidation at the oxide|electrolyte interface when a ratio of oxalic to formic acid reaches 1:4. It results in an almost complete block of the regular anodic film formation. In the case of 20 mM oxalic acid, this ratio is 1:20, so the oxalate ions do not compete with formates and only prevent the release of aluminum ions into the solution (see Figure 3.16 and Figure 3.18, E).

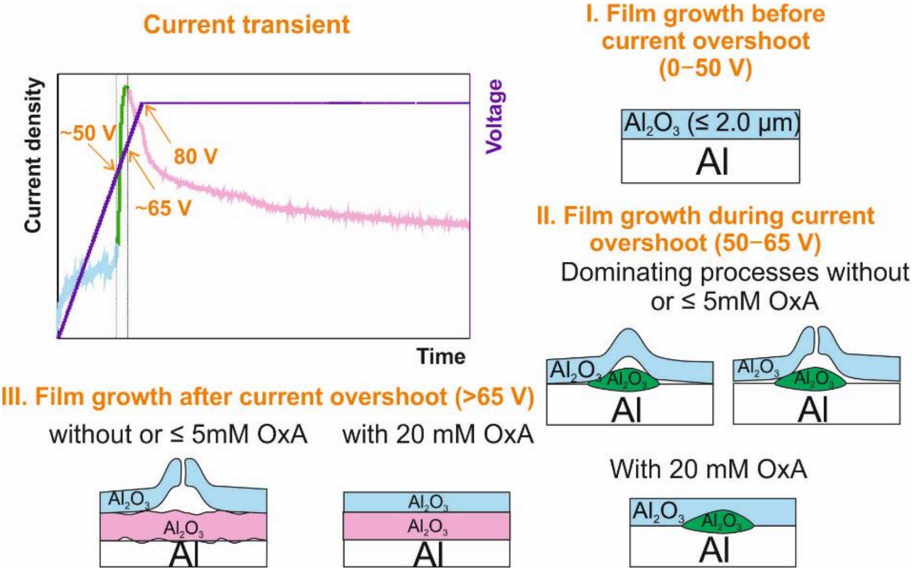

Figure 3.19. Schematic representation of the processes that occur during the electrochemical aluminum oxidation in formation in a 0.4 M HCOOH + 0.03 M $(NH_4)_6Mo_7O_{24}$ + 5–20 mM $H_2C_2O_4$.

Practically, the dependence of J_a on the anodizing time provides only indirect information on the rate of the alumina formation, as the barrier layer possesses high thermal resistance, and part of the electrical energy converts to thermal energy that consequently speeds up alumina dissolution [132]. To investigate the effect of various additives on alumina growth in a formic acid solution, we determined the experimental values of specific charge (Q_h) spent for growing 1 µm of the anodic alumina using current transients (see Figure

3.16) and SEM data (see Figure 3.18). As can be seen from Table 3.5, Q_h is 2.34–2.77 C cm^{-2} µm^{-1} if the electrolyte contains ammonium heptamolybdate. Adding oxalic acid somewhat improves film growth, which completely agrees with data obtained for oxalic–sulfuric acid anodizing [54]. While in the absence of ammonium heptamolybdate, Q_h equals 4.165 C cm^{-2} µm^{-1}, about 1.5 times higher.

Table 3.5. Specific charge (Q_h) spent for growing 1 µm of the anodic alumina in a 0.4 M HCOOH (FA) containing different amounts of $H_2C_2O_4$ (OxA) with and without 0.03 M $(NH_4)_6Mo_7O_{24}$ (AHM) at 80 V.

Sample	**Q_h, C cm^{-2} µm^{-1}**
FA+AHM	2.65
FA+AHM+5mMOxA	2.70
FA+AHM+10mMOxA	2.36
FA+AHM+20mMOxA	2.34
FA+20mMOxA	4.165

Another approach to determine the current efficiency (CE) of electrochemical Al oxidation in formic acid containing different amounts of oxalic acid with and without ammonium heptamolybdate consists of measuring the aluminum ions content in the electrolyte after anodizing. For this, the electrolyte for analysis was taken after 10 h of anodizing. The mass of aluminum in the films was determined by TG/DTA. The overall amount of aluminum oxidized in the electrochemical reaction was calculated using the Faraday law. The CE was evaluated as the ratio of obtained experimentally Al^{3+} ions to their number calculated theoretically. As seen from Table 3.6, the ratio of Al^{3+} ions in the solution to their number in the film varies from 2 to 3% in the case of molybdate-containing electrolytes.

Table 3.6. The current efficiency (CE) of electrochemical Al oxidation in a 0.4 M HCOOH (FA) containing different amounts of $H_2C_2O_4$ (OxA) with and without 0.03 M $(NH_4)_6Mo_7O_{24}$ (AHM) at 80 V, 10 h calculated using TG/DTA and optical emission spectroscopy data.

Sample	**$m_{Al(sol)}$, mg**	**$m_{Al(film)}$, mg**	**$m_{Al(total)}$, mg**	**Q, C**	**$m_{Al(theory)}$, mg**	**CE, %**
FA+AHM	0.24	13.52	13.76	376	35.10	39.2
FA+AHM+5mM OxA	0.47	15.65	16.12	528.5	49.30	32.7
FA+AHM+10mM OxA	0.47	18.26	18.73	567	52.90	35.4
FA+AHM+20mM OxA	0.47	14.81	15.28	528	49.30	31.0
FA+20mMOxA	5.10	24.19	29.29	615	57.40	51.0

The CE is at the level of 31.0–39.2%. Adding oxalic acid to formic acid changes the situation significantly compared with the ammonium heptamolybdate case, and the concentration of Al^{3+} ions in the solutions becomes 10 times higher. The CE increases to 51.0%. Usually, the ratio of Al^{3+} ions in the solution to their number in the film is about 30% [43], so when ammonium heptamolybdate is added, the concentration of Al^{3+} ions in the solution is very low. At the same time, this value is close to the literature data for the formic acid electrolyte containing only oxalic acid. Therefore, these results indicate that in the case of aluminum anodizing in formic acid, the ammonium heptamolybdate additive prevents aluminum dissolution more effectively than only oxalic acid. Adding oxalic acid and ammonium heptamolybdate decreases the acidity of the electrolyte. As ammonium heptamolybdate has the highest pH among other electrolyte components (pK_a(HCOOH) 3.745, $pK_a(H_2C_2O_4)$ 4.14, and pH(0.03 M $(NH_4)_6Mo_7O_{24}$) 5.6), it increases pH of the solution more effectively and therefore reduces aluminum dissolution rate. However, in this case, the morphology of the film leaves something to be desired. The role of oxalic acid in this process is only to improve film growth and morphology, smoothing its surface.

3.4.4. Carbon states and content depending on the oxalic acid concentration

To characterize anodic alumina formed in formic acid containing oxalic acid with or without ammonium heptamolybdate additive over a broad temperature range, determine and compare the composition of the films, we applied TG/DTA analysis coupled with mass spectrometry up to 1300 °C in the Ar atmosphere (Figure 3.20). The TG/DTA curves for all the samples looked very similar, so to simplify the perception of the figure, we show as an example only the TG/DTA plot for the sample anodized in the aqueous solution of 0.4 M HCOOH, 0.03 M $(NH_4)_6Mo_7O_{24}$, and 20 mM $H_2C_2O_4$. The behavior of anodic alumina films upon heating is widely discussed in the literature [5,30,124,133–135], and our study in this aspect does not differ much from previous ones. What we would like to pay special attention to is the composition and behavior of carbon-containing compounds, as the carbon content in our samples is 2.2 and 1.7 times higher than in oxalic and tartaric anodic alumina films [5,11,30].

In Figure 3.20, Peak I (200–400 °C) corresponds to the deletion of physically adsorbed CO_2 and CO; Peak II (600–800 °C) occurs due to the evolution of CO and CO_2 coming from carbonate and carboxylate species decomposition. As was shown in previous TG/DTA and FTIR studies on the thermal decomposition of carbon-containing alumina films (see Section 0), Peak III ($CO + CO_2$ evolution) (800–1050 °C) mainly originates from the decomposition of carbon in sp^2 and sp^3 states. The results obtained for all samples are summarized in Table 3.7.

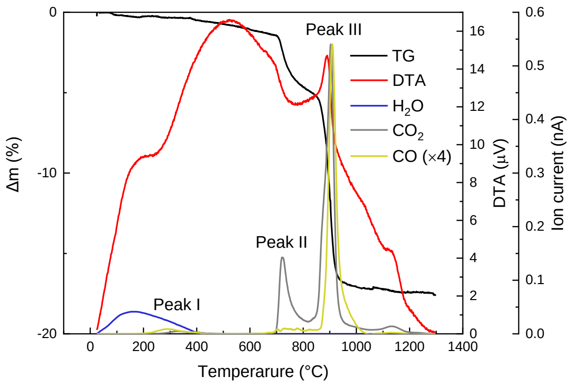

Figure 3.20. TG/DTA plot and evolved gas analysis for anodic alumina film formed in the aqueous solution of 0.4 M HCOOH + 0.03 M $(NH_4)_6Mo_7O_{24}$ + 20 mM $H_2C_2O_4$ at 80 V, 18 °C.

Table 3.7. Chemisorbed CO and CO_2, carbon (from carbonate carboxylate structures), and carbon content (mass %) in the anodic alumina films formed by oxidation in a 0.4 M HCOOH (FA) containing different amounts of $H_2C_2O_4$ (OxA) with and without 0.03 M $(NH_4)_6Mo_7O_{24}$ (AHM) at 80 V according to TG/DTA data (See Figure 3.20).

Sample	**ω_C(Peak I)**		**ω_C(Peak II)**		**ω_C(Peak III)**		**$\omega_{C(CO+CO_2)}$ total, %**
	C_{CO_2}, %	C_{CO}, %	C_{CO_2}, %	C_{CO}, %	C_{CO_2}, %	C_{CO}, %	
FA+AHM	0.53	0.17	0.93	0.01	2.88	0.79	5.31
FA+AHM+ 5mMOxA	0.58	0.07	1.01	0.06	3.39	0.56	5.67
FA+AHM+ 10mMOxA	0.27	0.03	1.05	0.00	3.50	0.39	5.24
FA+AHM+ 20mMOxA	0.07	0.03	0.97	0.03	3.34	0.53	4.97
FA+20mMOxA	0.06	0.01	0.06	0.01	2.64	0.59	3.37

As for chemisorbed CO_2 and CO, they come from electrolyte decomposition in one of the possible ways [112]. The amount of adsorbed gases cannot provide helpful information for quantitative analysis since the part of gases released into the surroundings is unknown. Moreover, the process of their adsorption depends on many factors, such as the presence of active sites on alumina and the rate of oxide formation and dissolution. We also recalculated the contribution of CO and CO_2 to Peak II and Peak III to pure carbon to ease the comparison, as it is almost impossible to distinguish between the contributions of the decomposition of amorphous carbon and carbonate-carboxylate species. However, considering the low intensity of Peak II, we could claim that the decomposition of amorphous carbon mostly contributes to the CO and CO_2 evolving at 600–1050 °C. As seen from Table 3.7, the content of carbonate-carboxylate species (Peak II) and carbon in sp^2 and sp^3 states (Peak III) and total carbon content do not change significantly and is 4.87–5.05 mass % and 4.97–5.67 mass %, respectively, if the electrolyte contains ammonium heptamolybdate. Compared with heptamolybdate-containing electrolytes, if only oxalic acid is added to the formic acid solution, the carbon in sp^2 and sp^3 states and total carbon content decreases to 3.23 mass % and 3.37 mass %, respectively. Another piece of evidence is that ammonium heptamolybdate improves film growth by increasing its thickness. As shown [106,132], the thicker the alumina layer, the more local overheating; thus, more adsorbed electrolyte ions are converted into carbon in the sp^2 and sp^3 states.

The results presented in Section 3.4 are summarized in a scientific article: K. Chernyakova, V. Klimas, R. Karpicz, A. Naujokaitis, A. Jagminas, Effect of oxalic acid additives on aluminum anodizing in formic acid containing ammonium heptamolybdate, *J. Electrochem. Soc.* (2023) DOI: 10.1149/1945-7111/ad0513.

3.5. Optical and fluorescence properties of the porous alumina films formed in formic acid solutions with different additives

3.5.1. Optical properties of the films formed in formic acid with sodium metavanadate additives

The anodic oxides of Al obtained in sulfuric and phosphoric acid solutions are transparent and colorless, while those grown in oxalic, citric, and tartaric acid solutions are slightly yellow, greenish-gray, and gray, respectively [136]. The optical bandgap energy (E_g) of conventional alumina allows direct transitions from 5.40 to 5.75 eV [137]. The E_g of anodic alumina ranges from 1.6 eV [96] to 4.3 eV [138]. Furthermore, the E_g value of oxalic acid anodic films slightly increases with anodizing voltage but remains constant with an increase in film thickness and porosity [139]. As reported in [138,139], photoluminescence investigations indicated the presence of F and F^+ centers in oxalic and sulfuric alumina films, which could be attributed to oxygen vacancy-related defect centers. The diffuse reflection spectra and the corresponding Tauc plots of alumina films formed in the optimized vanadate–formate solutions were found to be dependent on the anodizing time (Figure 3.21).

Moreover, the films formed at U_a values from 60 to 100 V for the same time, e.g., 1 h, possess a similar E_g value of about 1.78 eV, regardless of the anodizing voltage, which is in the far-visible region (Figure 3.21, C, plots 1 to 3). This band value is significantly lower than that reported for porous alumina films formed in sulfuric, oxalic, or carboxylic acid solutions under conventional conditions [138]. However, in the case of thinner films obtained, e.g., during 2- and 5-min anodizing at 80 V, their light absorption edge was approximated at 3.19 and 2.70 eV (Figure 3.21, C, 4 and 5 plots), respectively, implying the potential to control the E_g value and absorption properties of these films as a function of anodizing time.

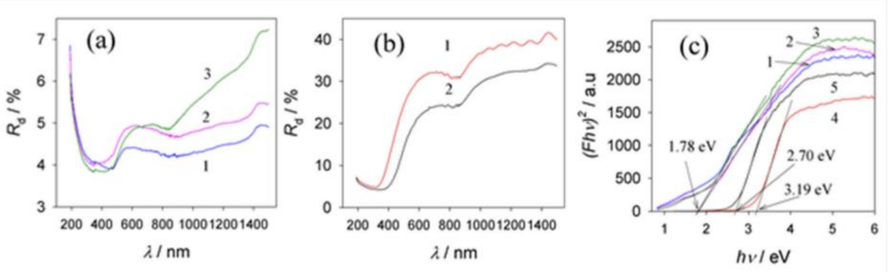

Figure 3.21. Diffuse reflectance spectra (A) and corresponding Tauc plots for possible direct transitions (C) in the composite films fabricated by Al anodizing in a solution containing 0.8 M HCOOH + 0.2 M $NaVO_3$ at U_a 60 V (1), 80 V (2), and 100 V (3) for 1 h. (B) As in (A) for Al anodizing at 80 V for 2 min (1) and 5 min (2). (C) Tauc plots for possible direct transitions in the composite films fabricated by Al in the same solution at U_a 60 V (1), 80 V (2), and 100 V (3) for 1 h, and at 80 V for 2 min (4) and 5 min (5).

Our electrolyte contained formic acid and sodium metavanadate. Therefore, it is reasonable to suggest that entrapped vanadium species could influence the optical properties of these hybrid films. According to previous reports [140], the bandgap energies of vanadium oxides O 2*p*–V 3*d* were equal to 2.0–2.6 eV. Therefore, the calculated E_g values in the range 3.05–3.2 eV would not affect the absorption of films formed in our electrolyte after 2 min with shorter processing, whereas the entrapment of vanadium oxides in thicker films with E_g = 2.98–3.10 eV could have been a factor. Another factor capable of distorting the true $\mathrm{E_g}$ value of our films according to the diffuse reflectance spectral analysis via the Tauc approach is the Al layer remaining under the film, capable of absorbing 1.5 eV energy [141]. To avoid this, we anodized 25 μm thick Al foil and analyzed the obtained transmission spectra before and after film calcination at 950 °C for 2 h (Figure 3.22). It is worth noting that the calculated E_g value for this and the Al substrate film grown at 80 V for 1 h showed quite a similar E_g value of 1.78 eV for the direct forbidden transition. However, the calcination of aluminum oxide/carbon hybrid material in the air increased E_g by 1.2–1.35 eV (see Figure 3.22).

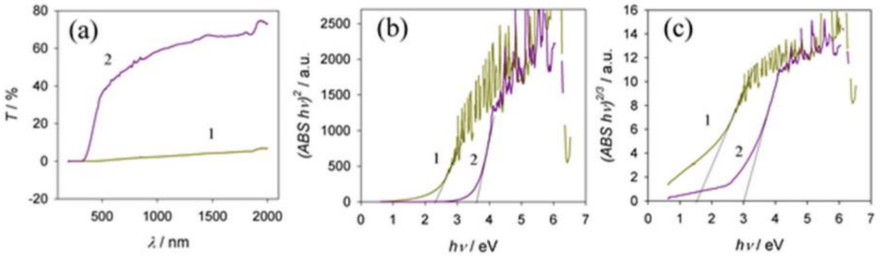

Figure 3.22. The transmission spectra (A) and calculated Tauc dependencies for direct (B) and direct forbidden transitions (C) in aluminum oxide samples obtained by Al anodizing in 0.8 M HCOOH + 0.2 M $NaVO_3$ at 80 V before (1) and after calcination at 950 °C for 2 h (2).

The results presented in Section 3.5.1 are summarized in a scientific article: Jagminas A, Klimas V, Chernyakova K, Jasulaitiene V. Designing carbon-enriched alumina films possessing visible light absorption, *Materials (Basel)* 15 (2022) 2700. doi: 10.3390/ma15072700.

3.5.2. Fluorescence properties of the films formed in formic acid with heptamolybdate and oxalic acid additives

The changes in the chemical composition and structure of anodic alumina formed in 0.4 M HCOOH + 0.03 M $(NH_4)_6Mo_7O_{24}$, depending on the side of the sample, should influence the optical properties of the films. Fluorescence studies carried out using a streak camera under excitation at 343 nm confirm it (Figure 3.23).

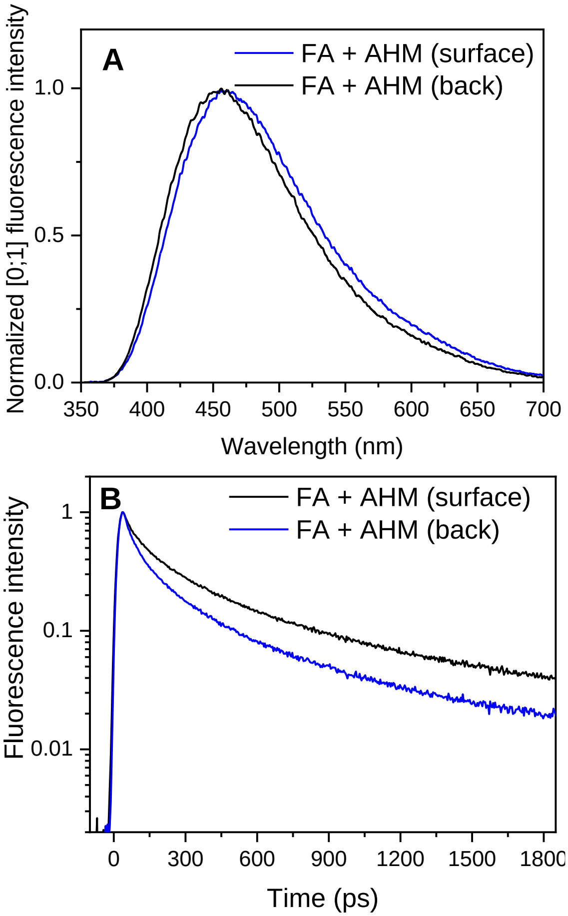

Figure 3.23. Fluorescence spectra of the surface and back sides of the anodic alumina formed in 0.4 M HCOOH + 0.03 M $(NH_4)_6Mo_7O_{24}$, 80 V, 18 °C, 1 h, under excitation at 343 nm. The fluorescence was integrated with a 350–650 nm spectral range (A). Normalized fluorescence decay kinetics of the surface and back sides under excitation at 343 nm (B).

As can be seen from Figure 3.23, integrated fluorescence spectra are characterized by a wide blue fluorescence in the wavelength range of 350–700 nm with a maximum at around 455 and 460 nm for surface and back sides, respectively. All spectra were normalized to maximum intensity for a better qualitative comparison of the different spectra. The width of the spectra (full width at half maximum (FWHM)) is approximately the same and equal to 120 nm (Figure 3.23, A). The fluorescence decay data were integrated into a 350–650 nm wavelength range to obtain fluorescence decay kinetics (Figure 3.23, B). The measurements revealed that fluorescence decay is nonexponential and can be described by the average lifetime of 0.30 and

0.32 ns for the surface and back sides, respectively. The fluorescence spectra for the time interval 0–1000 ps were acquired by integrating the emission maps (Δt = 100 ps) and the time axis (Figure 3.24). As can be seen, for the surface side of the sample in the first 100 ps after excitation, there is a maximum at around 450 nm. In 1000 ps after excitation, the fluorescence maximum slightly redshifts (to 470 nm), but the FWHM almost does not change. The broad fluorescence band of anodic alumina is determined by the amorphous state of the sample as, in this case, various local electronic states of the same structure defects can occur.

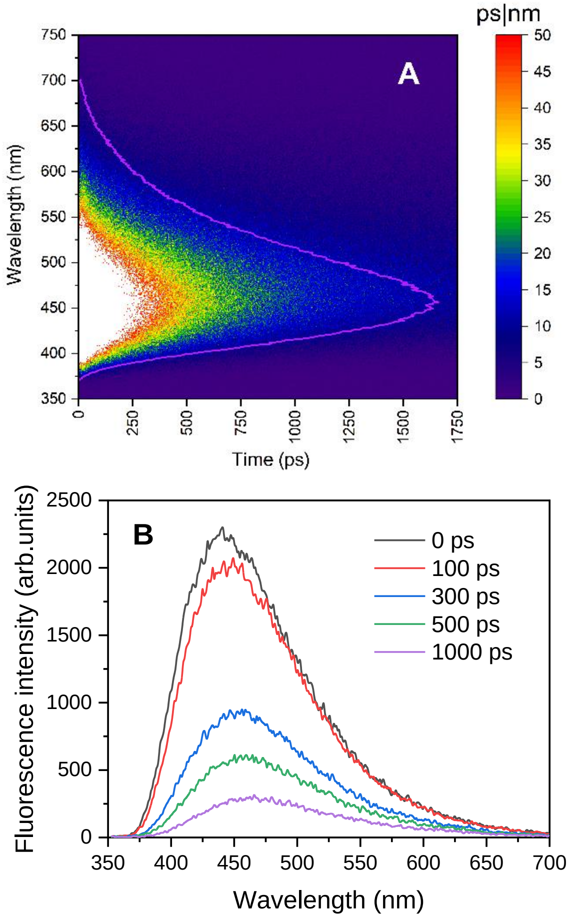

Figure 3.24. Time-resolved emission map of the back side of the anodic alumina formed in 0.4 M HCOOH + 0.03 M $(NH_4)_6Mo_7O_{24}$, 80 V, 18 °C, 1 h under excitation at 343 nm (A). The fluorescence given by the color scale increases from blue to red. Time-resolved emission spectra at different decay times (B).

Moreover, there are different carbon-bearing components by nature, and their emission spectral range can overlap with each other and the alumina [113]. Our previous studies showed that hydrogenated amorphous carbon (*a*-C:H) clusters formed during anodizing in tartaric acid are linked to the oxide network through the carboxylate ions and coordinative polyhedra of Al^{3+} ions. Under annealing at 800 °C, they undergo structural changes affecting the fluorescence character, i.e., its intensity and spectrum width [11]. These findings imply that the fluorescence spectrum is a superposition of several decay components. These can be different carbon-containing compounds and functional groups, such as OH, C=O, and COOH. At the same time, functional groups possess their fluorescence [142] and, therefore, can change the fluorescence of amorphous films. According to XAES data, carbon in the sp^3 state prevails on the back side of the films, and it can cause a redshift of the fluorescence spectrum. Decay kinetics also confirm this, as the fluorescence kinetics at 450 nm drops faster than at 550 nm (Figure 3.25).

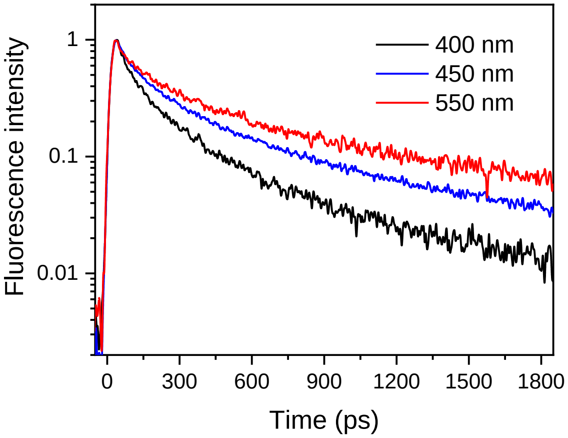

Figure 3.25. Normalized fluorescence decay kinetics of the back side of the anodic alumina formed in 0.4 M HCOOH + 0.03 M $(NH_4)_6Mo_7O_{24}$, 80 V, 18 °C, 1 h, recorded at different emission wavelengths.

Further studies showed the differences between the fluorescence properties of anodic alumina films formed in formic and sulfuric acid solutions. The first thing to note is the differences in the colors of the samples obtained. The ones formed in formic-acid-containing solution are black (0.4 M HCOOH and 0.03 M $(NH_4)_6Mo_7O_{24}$) or yellowish (0.4 M HCOOH and 20 mM $H_2C_2O_4$), and the ones formed in sulfuric acid are colorless and completely transparent (Figure 3.26, Inset). Second, the fluorescence excitation spectra of both samples formed in formic acid (λ_{em} = 450 nm) have a narrow peak

(FWHM is ca. 60 nm) at ca. 350 nm; the emission spectra of these films (λ_{ex} = 380 nm) have a broad emission peak (FWHM is ca. 125 nm) at ca. 440 nm. At the same time, the sulfuric acid anodic alumina does not have fluorescence in the mentioned wavelength region (Figure 3.26). Therefore, one can conclude that these peaks belong to the fluorescence of carbon-containing samples and can be attributed to the carbon embedded into the anodic alumina films.

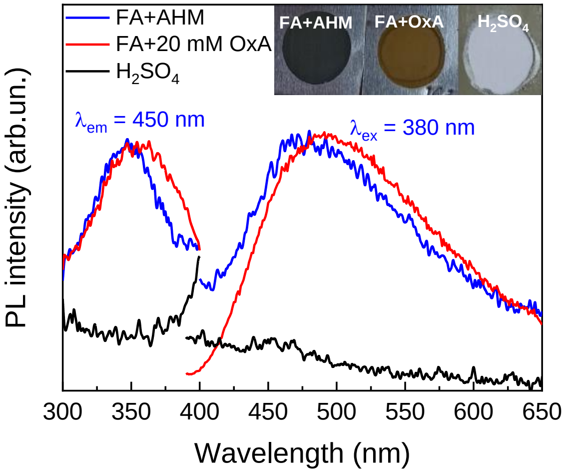

Figure 3.26. Fluorescence excitation at λ_{em} = 450 nm and fluorescence emission at λ_{ex} = 380 nm spectra of the anodic alumina films formed in 0.4 M HCOOH (FA) + 0.03 M $(NH_4)_6Mo_7O_{24}$ (AHM), 0.4 M HCOOH + 20 mM $H_2C_2O_4$ (OxA), and 1.8 M H_2SO_4. The inset shows the surface appearance of the films.

The results presented in Section 3.5.2 are summarized in a scientific article: K. Chernyakova, V. Jasulaitiene, A. Naujokaitis, R. Karpicz, I. Matulaitiene, V. Klimas, A. Jagminas, Aluminum anodizing in an aqueous solution of formic acid with ammonium heptamolybdate additive, *J. Electrochem. Soc.* 170 (2023) 013501. DOI: 10.1149/1945-7111/acb019.

3.6. Characterization of states of the carbonaceous species embedded into the anodic alumina oxide

We further extracted the carbon from anodic alumina films according to the procedure described in Section 2.1.4. As was mentioned above, the carbon embedded in the films is in the form of nanosized particles. The solutions of carbon nanoparticles (CNPs) obtained from the anodic alumina films formed in 0.4 M HCOOH + 0.03 M $(NH_4)_6Mo_7O_{24}$ and 0.4 M HCOOH + 20 mM $H_2C_2O_4$ are denoted CNPs-1 and CNPs-2, respectively. As shown before, by combining with the surface groups of carbon nanoparticles, Al^{3+} and Fe^{3+} ions became one of the most effective sources among other metal ions for quenching the fluorescence of these nanoparticles [38]. Therefore, the solutions were carefully washed from Al^{3+} ions by dialysis.

CDs are a comprehensive term for various nanosized carbon materials. In a broad sense, all nanosized materials composed mainly of carbon can be called CDs. They are quasi-spherical fluorescent nanoparticles with sizes of less than 10 nm, composed of carbon nuclei with various functional groups on the surface. CDs include carbon nanodots (CNDs) and polymeric dots (PDs). CNDs are always spherical and are divided into CNPs, which do not have a crystal lattice, and carbon quantum dots (CQDs), which have an obvious crystal lattice. As a result, the fluorescence center is very different for the different types of CDs. There are a variety of fluorescent CDs and synthetic routes to obtain these materials. Therefore, the chemical structures of CDs are diverse and depend on synthesis approaches.

Moreover, fluorescent CDs are mostly not “pure” carbon materials, so the hybridization and ratio between the carbon core and surrounding chemical groups play an important role in the fluorescence behavior of CDs. To our knowledge, carbon nanoparticles have not been previously obtained from carbon-containing anodic alumina films. Therefore, to understand the nature of synthesized carbon nanoparticles and characterize them, we determined their composition and investigated optical and fluorescence properties. Before discussing the fluorescence of CNPs, it should be noted that its mechanism is still not well understood. At least two fluorescence mechanisms for CDs are extensively accepted. One mechanism is that the fluorescence comes from the band gap states based on the conjugated π-domains in the carbon nucleus of the CDs, and the other is that the luminescence comes from the surface-related defect band states of the CDs, which can cause surface energy traps [143].

Figure 3.27, A–B, shows the TEM images of the produced CNPs, revealing the spherical separated from each other nanoparticles with a ca. 20–25 nm diameter. The zeta potential of the CNPS-1 and CNPS-2 does not differ and shows a single negative peak at −29.2 mV with a width of 8.20 mV (Figure 3.27, C). The negative potential indicates that the surface of CNPs has negatively charged moieties, such as C=O, C–O, and O–H, which are essential to get the water solubility of CNPs. Z-potential also shows the degree of repulsion between the charged particles in the dispersion. High zeta potential implies highly charged particles, which prevents aggregation of the particles due to electric repulsion. If the zeta potential is low, attraction overcomes repulsion, and the mixture likely coagulates. The zeta potential value of −30 mV is considered optimum for good stabilization of a nanodispersion [144]. Therefore, in our case, the value of zeta potential indicates that the colloidal stability of CNPs is high, and the solutions can be used over time.

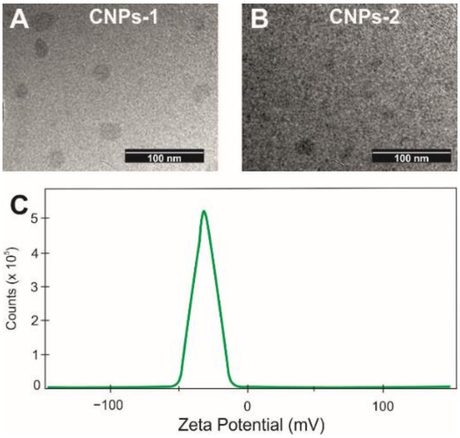

Figure 3.27. TEM images of CNPs-1 (A) and CNPs-2 (B) and Z-potential curve of CNPs-1 dispersed in water (C).

SERS spectra of CNPs-1 and CNPs-2 obtained from the films formed in the solution of 0.4 M HCCOH and 0.03 M $(NH_4)_6Mo_7O_{24}$ and 0.4 M HCOOH and 20 mM $H_2C_2O_4$, respectively, show two distinct peaks at 1365 cm^{-1} (*D*-band) and 1600 cm^{-1} (*G*-band) (Figure 3.28). The *G*-band (sp^2 hybridization) represents the graphitization associated with the CNPs, and the *D*-band (sp^3 hybridization) represents the amount of defect and functionalization. The intensity ratio of the peak of the *G*- to the *D*-band was found to be 2.20. The I_G/I_D ratio indicates that the synthesized CNPs mainly comprise sp^2 graphitic carbons with sp^3 carbon defects originating from oxygen-containing groups [145–148]. SERS results agree with Raman spectra of CDs obtained by other methods [147,149]. Moreover, they agree with our FTIR studies of the corresponding films (see Section 3.3.2) that showed the presence of physically adsorbed CO_2 and CO on the surface of the samples and incorporated carboxylate and hydroxyl ions and carbon in sp^2 and sp^3 states in the anodic alumina.

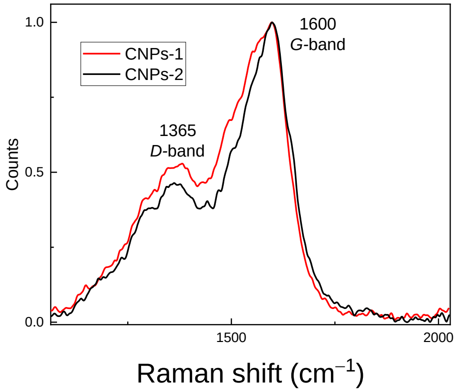

Figure 3.28. SERS spectra CNP-1 and CNP-2 solutions extracted from the films obtained in 0.4 M HCOOH + 0.03 M $(NH_4)_6Mo_7O_{24}$ and 0.4 M HCOOH + 20 mM $H_2C_2O_4$, respectively.

The aqueous solutions of CNP-1 and CNP-2 are transparent or slightly yellowish (Figure 3.29, inset). UV-Vis absorption spectra of the CNP-1 and CNP-2 solutions have characteristic bands at 237, 267, and 316 nm and a long absorption slope toward 500 nm (Figure 3.29, A). The typical absorption spectrum of CQDs, like CNPs, appears as a strong absorption in the UV region (230–320 nm), sometimes with a band at 285 or 340 nm and a long tail expanding in the visible region, which partly belongs to the light scattered on the small particles [145–149]. The absorption in the 230–290 nm region belongs to the π-π^* transitions in the C=C bonds and in the 290–380 nm region, to the n-π^* transitions usually determined by C=O bonds or other species outside the core-shell [146].

The fluorescence excitation spectra of both CNP samples (λ_{em} = 440 nm) have a similar narrow peak (FWHM of ca. 60 nm) at ca. 350 nm as in the anodic alumina films (see Figure 3.26). Upon excitation at 360 nm, the CNP spectra exhibit one broad and strong emission band at ca. 440 nm (Figure 3.29, B). Similar absorption-emission features were observed for carbon dots (CDs) obtained from candle soot [150]. The emission spectra of the films excited at 380 nm are broader, with a maximum redshifted to ca. 490 nm compared with the spectra of CNPs. The alumina matrix is amorphous and has various structural and point defects that also contribute to the total emission of the samples, so it affects the shape and maximum position of the fluorescence spectra [71,74–77,80].

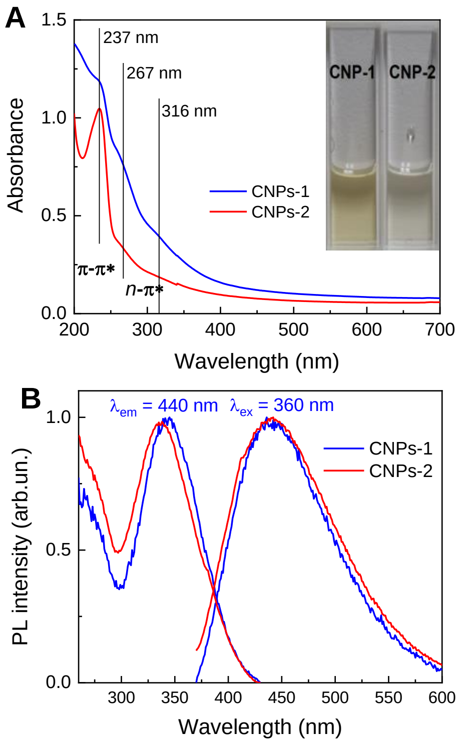

Figure 3.29. Absorption (A) and fluorescence at $\lambda_{ex} = 360$ nm and fluorescence excitation at $\lambda_{em} = 440$ nm (B) spectra of CNP-1 and CNP-2 solutions. Inset shows CNP solutions in 10-mm quartz cuvettes.

Solutions of CNPs-1 and CNPs-2 exhibit an excitation-dependent emission behavior at 280–450 nm excitation wavelengths. At λ_{ex} = 280–290 nm, the emission maximum is at ca. 450 nm, then slightly blueshifts to 415 nm at λ_{ex} = 320–340 nm. It redshifts from 415 to 525 nm as λ_{ex} increases from 350 to 450 nm (Figure 3.30). The excitation-dependent emission behavior is one of the typical photophysical characteristics of CDs that originates from the surface state of these nanomaterials [143,145,150–154]. The bandgap of CDs decreases with an increase in the degree of oxidation, i.e., CDs with a lower degree of oxidation are more likely to be excitation-independent [155]. Before discussing the fluorescence of CNPs, it should be noted that its mechanism is still poorly understood. At least two fluorescence mechanisms for CDs are extensively accepted. One mechanism is that the fluorescence comes from the band gap states based on the conjugated π-domains in the carbon nucleus of the CDs, and the other is that the luminescence comes from the surface-related defect band states of the CDs, which can cause surface energy traps [143]. In our case, both mechanisms are involved: the first dominates when the core of CNPs is excited at λ_{ex} = 300–340 nm, and the second appears due to various emission centers, such as carbonyl, carboxyl, and hydroxyl groups on the CNPs surface, under 280–300 nm and 340–450 nm excitation.

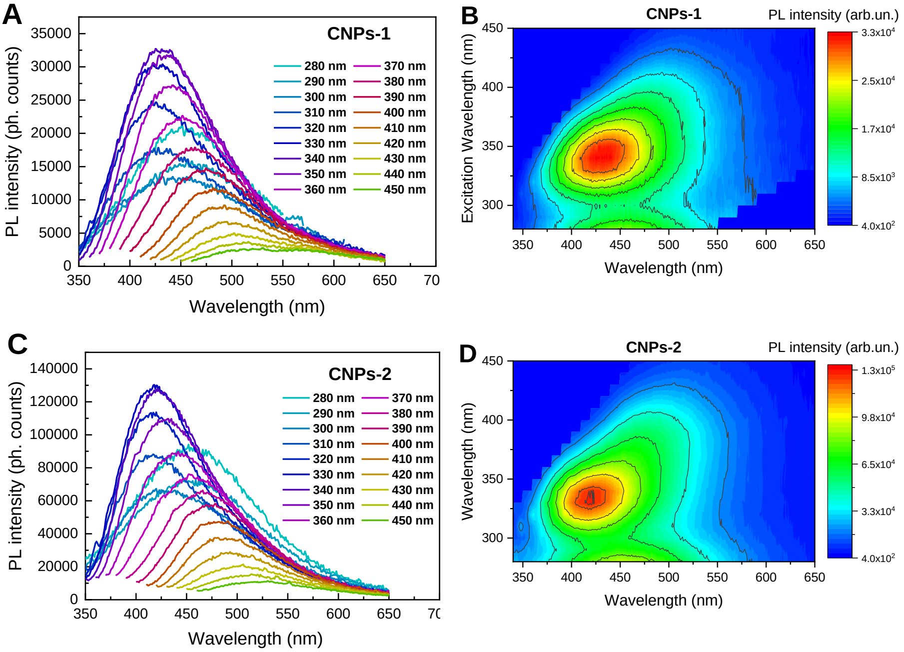

Figure 3.30. Fluorescence spectra under various excitation (A, C) and fluorescence excitation maps (B, D) of CNP-1 (A, B) and CNP-2 (C, D) solutions.

Time-resolved fluorescence experiments are performed at $\lambda_{ex} = 375$ nm to observe the pure radiative recombination processes as a necessary complement. All the fluorescence transients are probed at fluorescence peaks and are well-fitted with multi-exponential functions. The best-fit parameters are listed in Table 3.8; results for the anodic alumina films are shown for comparison. For the anodic alumina films, the average FL lifetimes (τ_{ave}) do not depend on the anodizing conditions and are 1.54 and 1.59 ns for samples formed in 0.4 M HCOOH and 0.03 M $(NH_4)_6Mo_7O_{24}$, 0.4 M HCOOH and 20 mM $H_2C_2O_4$, respectively. For the CNP solutions, τ_{ave} significantly increase compared with the films and are 7.25 and 8.04 ns for CNPs-1 and CNPs-2, respectively.

Table 3.8. Decay times determined for anodic alumina films formed in 0.4 M HCOOH + 0.03 M $(NH_4)_6Mo_7O_{24}$, 0.4 M HCOOH + 20 mM $H_2C_2O_4$ and solutions of CNPs-1 and CNPs-2 (λ_{ex} = 375 nm).

Sample	**FL excitation band, nm**	**FL band, nm**	**τ_1, ns (%)**	**τ_2, ns (%)**	**τ_3, ns (%)**	**τ_{ave}, ns**
FA + AHM	347	484	0.16 (25%)	0.8 (41%)	3.4 (34%)	1.54
FA + 20mM OxA	355	490	0.1 (17%)	0.71 (42%)	3.1 (41%)	1.59
CNPs-1	343	440	0.5 (11%)	2.71 (34%)	11.4 (55%)	7.25
CNPs-2	337	440	0.64 (11%)	3.06 (34%)	12.6 (55%)	8.04

Since the CNPs were obtained by the dissolution of anodic alumina films without additional treatment, such as ultrasonication, we can conclude that, first, carbon is obtained during the anodic oxidation of formate ions and is incorporated in the alumina as carbon in the sp^2 and sp^3 state that can be extracted from the initial films. Second, this carbon component is luminescent carbon nanoparticles; third, the alumina matrix significantly quenches the fluorescence of the embedded carbon.

Luminescence-based immunoassays have become powerful tools in biological and clinical diagnoses and microbial investigations in the past decade. Therefore, CDs could be an exceptional candidate for detection technology as they can be easily prepared and possess chemical and biological compatibility, well-defined luminescence signal with tunable wavelength options, diverse surface functionality for further modification, low electrical resistance, and acceptable conductivity. Several designed detecting systems are also constructed around CD luminescence signals measuring various analytes in biological environments [154,156,157].

Therefore, to test whether our novel CNPs confer any cytotoxicity, we performed their biocompatibility assay with living COS-7 mammalian cells. For this purpose, three different concentrations (3-fold, 10-fold, and 100-fold dilution of the stock solution) of respective CNPs were introduced into the wells containing glass surface-adhered living COS-7 cells and; after that, the samples were stored in an incubator for 10 h with the repeating bright-field microscopy imaging cycles every 2 h. Even at the highest concentration, CNPs-1 and CNPs-2 had little to no effect on both COS-7 cells’ morphology and surface adhesion properties observed after 10 hours of incubation (Figure 3.31).

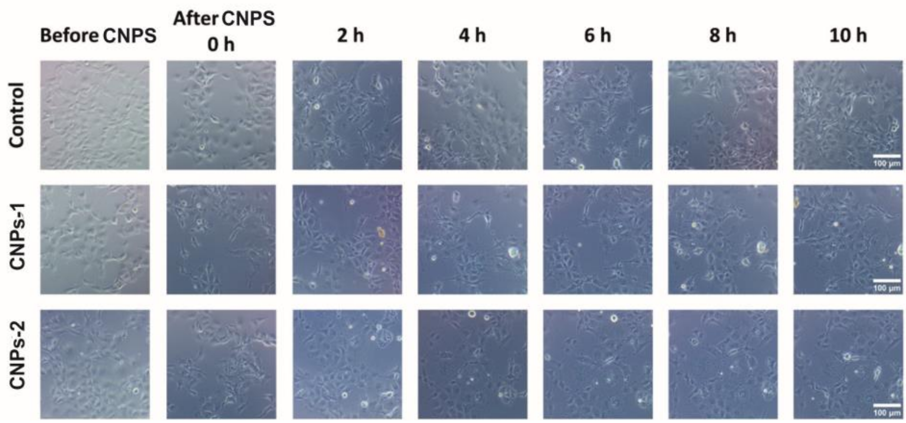

Figure 3.31. Impact of two different CNPs – CNPs-1 or CNPs-2 – on living COS-7 mammalian cells' survival over time. The cells adhered to the glass coverslip's surface were treated with the same concentration (3-fold dilution of the respective CNP stock) of CNP-1 or CNP-2 and then kept in an incubator for 10 h. Bright-field microscopy imaging of the COS-7 cells was performed at the initial moments before and after adding the CNPs and then every 2 h afterward. At every point in time, images were acquired at the different surface positions of the respective wells. Scale bar of all images: 100 µm.

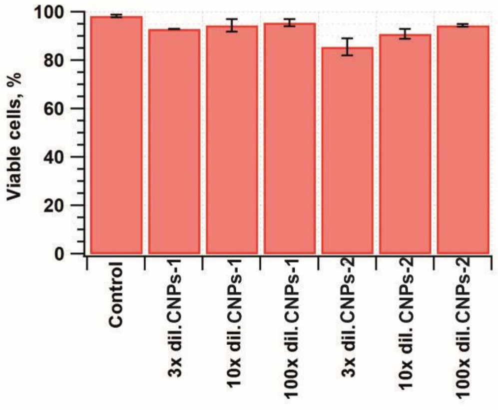

Figure 3.32. COS-7 mammalian cells' viability after 10-hour-long exposure of the cells to varying concentrations of CNPs-1 or CNPs-2. Bars represent the average number of viable cells under different conditions after 10 h. Error bars indicate the standard error of the mean (S.E.M.). The data used for the results represented in this graph was collected from at least two independent experiments.

The negative impact of only a minimal extent to the living cells was also confirmed by assessing the number of viable COS-7 cells left at the very end of the experiment (after 10 h), as for 3-fold diluted CNPs-1 93±0% of the cells remained viable and for 3-fold diluted CNPs-2 the cell survival index was 85.8±3.5%, while for the CNP untreated cells this value was estimated to be 98.3±0.5% (Figure 3.32).

Therefore, we conclude that our CNPs-1 and CNPs-2 exhibit high biocompatibility and possibly can be used for various *in vivo* applications with negligible harm to the living cells' integrity. However, if our method for synthesizing carbon nanoparticles from carbon-containing anodic alumina is considered a new and promising way, it should be improved, and further research is needed. It can be done in one of the following ways: by improving the synthesis conditions of the initial films to obtain samples with a larger amount of carbon and with a smaller CNP size for their more effective use in luminescence-based immunoassays. Depending on the procedure and degree of purification of CNPs and the pH of their solutions, the luminescent properties of the particles themselves can also be improved.

3.7. Formation and state of carbon in TiO_2 nanotubes obtained in ethylene-glycol-containing electrolytes

As titanium anodizing is almost as popular as aluminum, we investigated nanotubular titania prepared by titanium anodizing in electrolytes containing ethylene glycol to find similarities and differences in aluminum and titanium electrochemical oxidation in complex electrolytes containing organic compounds concerning the content and state of carbon embedded in the oxide structure.

3.7.1. Appearance and crystal structure of TiO_2 nanotubes

The as-anodized TiO_2 NTs are gray before heating, typical of amorphous TiO_2 NTs. Under heating in the air, the films turn bluish-gray. The appearance of this color in titanium dioxide crystals is due to color centers (or *F*-centers) and Ti^{3+} ions [158–162]. The film is white only after the nanotube structure is broken and larger TiO_2 crystallites are formed [84]. Under heating in hydrogen, the films become intensely black.

Figure 3.33 shows the SEM images of the TiO_2 NTs/Ti cross section and the surface. The inner diameter of TiO_2 NTs was 60±5 nm, the wall thickness was 12±2 nm, and the TiO_2 NT layer thickness was 13±2 μm. TEM images show the fine structure of individual TiO_2 NTs (Figure 3.34). The tubes have a granular structure. Individual TiO_2 crystallites with a 4.3–6.5 nm diameter occur, but larger particles (about 10 nm) can also be found. Noticeable differences in the size of crystallites after heating in air and hydrogen are not revealed. In TiO_2 NTs heated in hydrogen, the granular structure is more pronounced, and the formation of cracks is possible. These results agree with TEM data presented in [163], as during heating in H_2, the changes occur in a thin (nanometer) near-surface layer of TiO_2 crystallites [163,164].

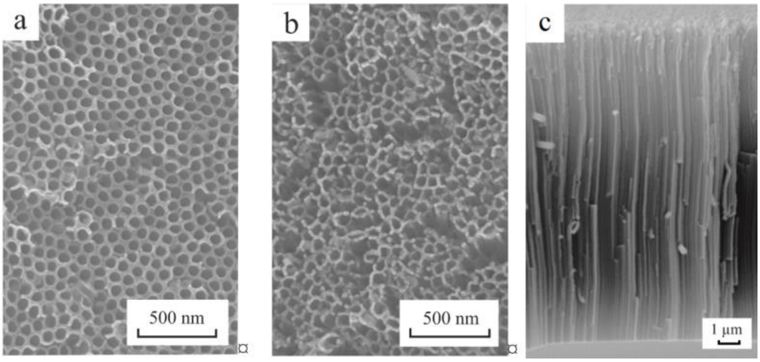

Figure 3.33. SEM images of the surface of (A) blue-gray TiO_2 NTs, 450 °C, air, 1 h, (B) black TiO_2 NTs, 500 °C, H_2, 1 h, (C) cross-section of the black TiO_2 NTs.

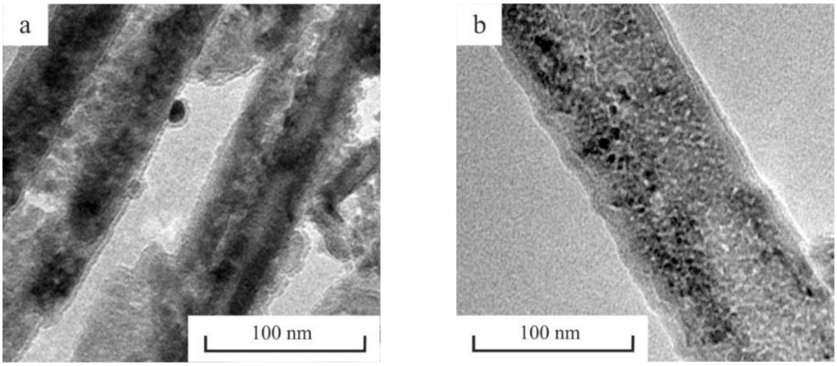

Figure 3.34. TEM images of the individual nanotubes: (A) blue-gray TiO_2 NTs, 450 °C, air, 1 h, (B) black TiO_2 NTs, 500 °C, H_2, 1 h

As-anodized TiO_2 NT films are X-ray amorphous. An anatase phase can only be detected in the samples heated in air and hydrogen with the parameters shown in Table 3.9. The parameters from the TiO_2 unit cell to TiO_2 NTs decrease, which reflects the compression of [TiO_{6-x}] octahedrons.

Table 3.9. XRD data on the parameters of the unit cell and the ratio of the intensities of some peaks

Sample / Color	**Phase**	***a*, Å**	***c*, Å**	I_{004}/I_{101}	I_{004}/I_{112}
Powder [*JCPDS* 84-1286]	Anatase	3.7822	9.5023	0.2	2.65
Powder Hombikat, H_2, 600 °C, 20 min / white	Anatase	3.7839	9.5047	0.2	3.4
TiO_2 nanotubes/Ti, air, 450 °C, 1 h / blue-grey	Anatase	3.7868	9.4773	0.5	2.4
TiO_2 nanotubes/Ti, H_2, 500 °C, 1 h / black	Anatase	3.7839	9.4744	3.2	7.5

3.7.2. Composition of TiO_2 nanotubes

Figure 3.35 shows a survey spectrum and high-resolution spectra of Ti2*p*, O1*s*, and C1*s* in the black TiO_2 NTs. As seen from Table 3.10, the element content is as follows: Ti – 25.0 at.%, O – 54.4 at.% and C – 19.7 at.%. The impurities of fluoride ions and nitrogen on the surface are not detected.

Table 3.10. The apparent surface chemical composition of black TiO_2 NTs determined by XPS

Surface chemical composition (at.%)		
C1*s* sp^3-C/CO/C=O/OC=O	O1*s* O^{2-}–TiO_2/CO(OH)/COH	Ti2*p* Ti^{3+}/Ti^{4+}
20.1	54.4	25.0
13.8/1.5/2.6/2.1	45.8/8.1/0.5	0.6/24.4

It follows from the spectrum (Figure 3.35, C) of Ti2*p* that TiO_2 with the binding energy (BE) Ti2$p_{3/2}$ of 458.8 eV prevails on the surface of the black TiO_2 NTs. Only 2.9 % of the total content of Ti ions are Ti^{3+} ions (BE is 456.7 eV). Ti^{3+} ion content is much lower than in the *c*-axis structured TiO_2 NTs sample obtained by vacuum heating, in which Ti^{3+} ion concentration is 31.7% [67].

The content of Ti^{3+} ions is specified neither in [65] nor in [104] for TiO_2 NTs heated in H_2, and the carbon content is measured to be considerably high (8–42 at.%). These results agree with the data on the carbon content in the black TiO_2 NTs obtained in our study (20.1 at.%). The position of the main C1*s* signal (C1*s* at 284.9 eV) (see Figure 3.35, C) indicates the presence of the amorphous carbon (sp^3 form) [165]. This state of carbon is 68.7 at.% of all carbon in the sample and ca. 13.8 at.% of the sum of atoms of all elements in the surface layer, including oxidized carbon.

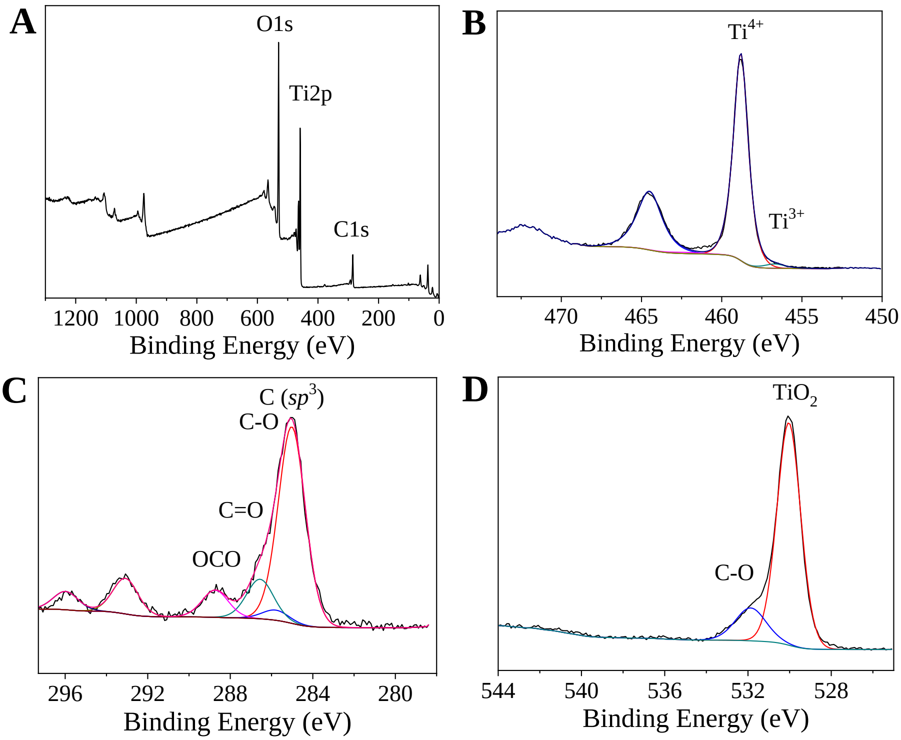

Figure 3.35. XPS spectra of black TiO_2 NTs, 500 °C, H_2, 1 h: (A) overview, (B) Ti2*p*, (C) C1*s*; (D) O1*s*.

The C1*s* lines at 285.8, 286.6, and 288.7 eV refer to the oxygen-containing functional groups: C–O, C=O, and OCO, respectively [166]. They result from partial oxidation of the carbon surface by atmospheric oxygen. According to the spectra of Ti2*p* and C1*s*, a Ti–C bond is not formed (no signal at ca. 282 eV, Figure 3.35, C), which means that the incorporation of C into the crystal lattice of TiO_2 does not occur. In the spectrum given in Figure 3.35, D, the O1*s* line of 530.0 eV is typical of TiO_2 oxygen, while the O 1*s* 531.8 eV line is typical of oxygen in organic C–O-functional and OH groups.

A single peak at 298 K and 77 K is registered in the EPR spectra of TiO_2 NTs heated in H_2 (Figure 3.36). In TiO_2 NTs heated in air, the signal is only detected at 77 K. There are no EPR signals in the spectrum of the as-anodized TiO_2 NTs sample. The signal intensity of TiO_2 NTs heated in H_2 is two orders of magnitude higher than for TiO_2 NTs heated in air. The concentration of PCs per unit area in TiO_2 NTs/Ti and the signal half-width are shown in Table 3.11.

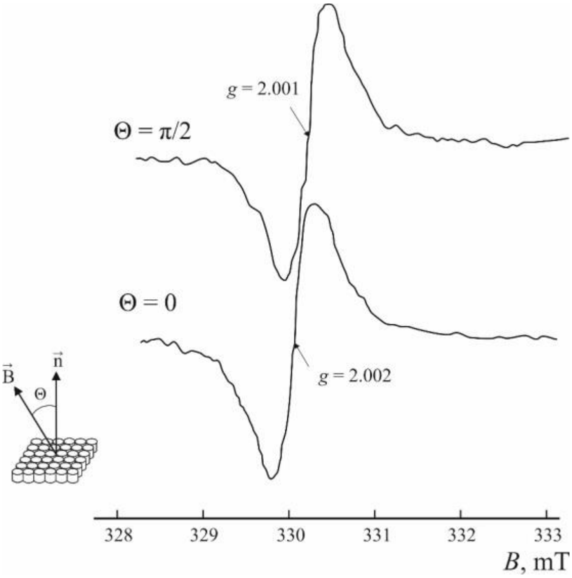

Figure 3.36. EPR spectra of black TiO_2 NTs recorded at different orientations of Ti-plate in the magnetic field *B*. Orientation of magnetic field *B* along the growth axis of TiO_2 NTs ($\theta = 0°$) and parallel to the Ti-plate (perpendicular to the growth axis of TiO_2 NTs) ($\theta = 90°$).

The signal at the arbitrary orientation of the titanium plate in the resonator of the spectrometer has a *g*-factor of 2.0018±0.0002. At parallel and perpendicular orientation of the titanium plate relative to the magnetic field *B*, a difference in *g*-factor values was found (see Figure 3.36). This phenomenon can be explained by a preferred phase orientation, where the spin is distributed [167]. As is known, TiO_2 NTs grow along the direction normal to the Ti substrate. When the orientation of the magnetic field *B* is along the normal to the substrate, the angle between the normal and the magnetic field (θ) is 0, and $g_{av} = 2.0020$. When *B* is parallel to the substrate, $\theta = \pi/2$, and $g_{av} = 2.0010$. The normal to the substrate corresponds to the growth axis of TiO_2 NTs. Thus, considering the oriented growth of TiO_2 [001] crystals, it mainly corresponds to the direction of the *c*-axis in $[TiO_6]$ anatase octahedrons.

The analysis of the experimental data reported in [33] suggests that the observed EPR signal at $g = 2.0018 \pm 0.0002$ can be attributed to C-containing radicals rather than to *F*-centers (single-charged oxygen vacancies). The signal with $g \approx g_e$ in TiO_2 is also assigned with carbon radicals [168–170]. The surface arrangement of the carbon centers on TiO_2 anatase rather than the bulk distribution has been substantiated. The signals with $g = 2.002–2.007$ can be attributed to the carbon centers [171].

Table 3.11. TiO_2 NTs/Ti samples, heat-treatment conditions, color, and EPR data

Heat-treatment conditions	**Crystalline state**	**Color**	**PC concentration, spin mm^{-2}**	**ΔB, mT**
As-anodized	Amorphous	Grey		
450 °C, air	Anatase	Blue-grey	0.2×10^{13}	1.0±0.1 (77 K)
500 °C, H_2	Anatase	Black	20×10^{13}	0.41±0.1 (298 K) 0.52±0.2 (77 K)

Several types of •C-radicals are distinguished in coals depending on the parameters of the spectrum [171]. The half-width of the signal (ΔB) of •C-radicals and the value of the g-factor depend on the degree of polycondensation of the system and the C:H ratio in it. The observed signal with $\Delta B = 0.4$–1.1 mT and $g = 2.0018 \pm 0.0002$ can be attributed to aryl-type radicals, i.e., polycondensed graphite-like molecules.

The angular dependence of the resonance position on the direction of the magnetic field B concerning the growth of TiO_2 NTs indicates an oriented arrangement of cyclic polymer structures in the pores of TiO_2 NTs. There is an oriented arrangement of carbon rings along the walls of TiO_2 NTs similar to that in carbon nanotubes (CNTs) [172]. Given the growth mechanism of CNTs, we can assume that carbon forms its nanotube structure inside the pores of TiO_2 NTs [173,174]. Carbon forms thin nanotubular layers on the surface of round particles [172,174].

In multiwalled carbon nanotubes (MCNTs), we observed an EPR signal with $g = 2.003$ (300 K), the position of the resonance and the intensity of which depend on temperature [175]. Our studies showed that in commercial MCNT NC7000TM with a diameter of $d = 9.5$ nm and a length of 1.5 μm at 298 K, an EPR signal is observed at $g = 2.0027$, $\Delta B = 2$ mT, and the PC concentration is high (about 3×10^{18} g^{-1}). The registration of the EPR signal is only possible at a minimum mass (0.3 mg) due to the high electric conductivity of MCNTs. The difference in the EPR parameters of •C-radicals may be explained by the fact that the size of carbon clusters is smaller, and the degree of polycondensation in the black TiO_2 NTs is evidently lower than those in MCNTs.

A distinctive feature of the FTIR spectra of the black TiO_2 NTs is a strong absorption in the wavenumber range of 750–4000 cm^{-1} (Figure 3.37). Against the background of this absorption, the vibrations δTiOH = 1066 and 1210 cm^{-1}, δOH = 1614 cm^{-1} and νOH = 3380 cm^{-1}, and νCOO = 1489 cm^{-1} are poorly distinguishable.

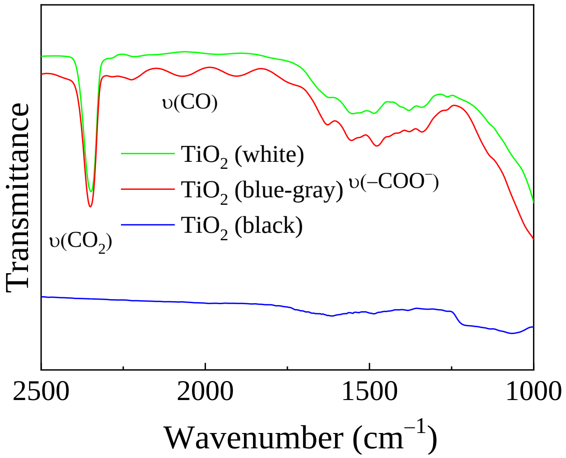

Figure 3.37. Fragment of the FTIR spectra (2500–1000 cm^{-1}) of black TiO_2 NTs, 500 °C, H_2, 1 h, blue-gray TiO_2 NTs 450 °C, air, 1 h, and white films TiO_2 [84].

In contrast to the black TiO_2 NTs, the FTIR spectrum of the blue-grey TiO_2 NTs (see Figure 3.37) heated in air exhibits a large variety of vibrations of carbonate-carboxylate and carbonyl structures in the wavenumber range of 1000–2500 cm^{-1} [176,177]. They might be the products of the electrochemical transformation of ethylene glycol and be formed due to the oxidation of carbon, which is being produced under heating. The results indicate that the thermal destruction of carbon-containing residual inclusions in amorphous TiO_2 NTs is effective even at 450 °C. Various Ti–CO complexes are registered on the surface of the films (νCO vibrations in the range of 1748–2282 cm^{-1}) and carbonate-carboxylate groups with typical vibrations: $\nu_{as}COO^{-}$ = 1485 cm^{-1} and $\nu_{s}COO^{-}$ = 1344 cm^{-1} [177,178]. Deep oxidation of carbon upon heating in the air is evidenced by CO_2 oscillations that emerged in the IR spectrum of TiO_2 NTs heated in the air.

The Raman spectrum of the black TiO_2 NTs is shown in Figure 3.38. In the region of normal Ti–O vibrations, peaks are registered at 634, 517.8, 397, and 147.6 cm^{-1}, which are typical of the Raman spectra of anatase: 634 (E_g), 519, 513 (B_{2g}, A_{1g}), 399 (B_{1g}), and 144 (E_g). The spectroscopy data confirm that the main phase in the black TiO_2 NTs has an anatase structure [177,179,180]. However, some peculiarities of the spectrum are observed, which are a consequence of the nanosized tubular structure of the sample. A decrease in the intensity of the E_g vibrations at 634 and 147.6 cm^{-1} relative to the B_{2g} and B_{1g} vibrations is observed. As noted above, E_g vibrations occur perpendicular to the *c*-axis in [TiO_6] octahedra. Their lower intensity might be due to the small wall thickness of the black TiO_2 NTs. It is known that the presence of impurity phases, for example, adsorbed carbon networks on the side faces, also contributes to the change in the line intensity.

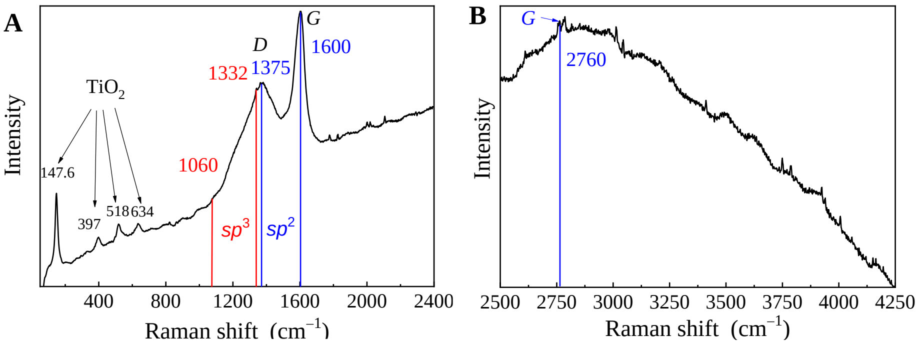

Figure 3.38. Fragments of the Raman spectra of TiO_2 NTs, 500 °C, H_2, 1 h, 50–2450 cm^{-1} (A) and 2500−4250 cm^{-1} (B).

The position of the E_g vibration line (147.6 cm^{-1}) in the Raman spectrum of the black TiO_2 NTs is shifted towards higher values relative to the calculated value for single crystals (144 cm^{-1}) and polycrystalline samples (143 cm^{-1}). The frequency of this oscillation is affected by the size of the particles and the nonstoichiometry of TiO_2 [21,181,182]. In [21], a correlation between the magnitude of this E_g oscillation in the Raman spectra and the size of TiO_2 crystallites was found – it grows with decreasing crystallite size. According to the revealed dependence, the TiO_2 particle size for the E_g vibration at 147.6 cm^{-1} should be less than 7.3 nm. This conclusion is consistent with the TEM data supporting the predominance of titanium dioxide crystallites with sizes of 4.3–6.5 nm in black TiO_2 NTs.

The Raman spectrum of the black TiO_2 NTs shows two high-intensity peaks at 1600 cm^{-1} (*G*-band) and 1375 cm^{-1} (*D*-band) (See Figure 3.38). These are typical sp^2-C vibrations in graphite [90,183,184]. *G*-band as the graphite 1600 cm^{-1}. The *D*-band becomes active in spectra due to the loss of symmetry in cyclic graphite structures caused by the lattice disorder, particle size effect, and impurities. This additional *D*-line corresponds to the vibrational mode forbidden in the ideal graphite by the selection rules [183,184]. The intensity ratio of the *D*- and *G*-lines might indicate the disorder extent in the structure of graphite networks. The high intensity of the *G*-line testifies to the occurrence of ordered, sufficiently long sections of polymeric cyclic structures and the retention of chain structures (polyenes). These data agree with the results of EPR spectroscopy, from which it follows that the C:H ratio in the carbon-containing inclusions is low.

The recorded Raman spectrum mainly characterizes the sp^2 state of carbon and might only indirectly indicate the presence of the sp^3 state. Thus, the peak *T* (1060 cm^{-1}), reflecting the vibration of ν(C–C) atoms in the sp^3 hybridization, is very weakly pronounced in the Raman spectrum. The presence of a 1332 cm^{-1} band corresponding to diamond sp^3-C can also be indirectly evidenced (see Figure 3.38). The low intensity of the sp^3-C peaks and the presence of an intense *D*-band show that symmetry distortion occurs in hexagonal networks due to the disorder or small size of the carbon inclusions themselves. As a result of this disorder, •C-radicals arise.

A broad band is observed in the spectra in the range of 2500–4000 cm^{-1} with a maximum at 2760 cm^{-1}. The ν(CH$_x$) and ν(OH) vibrations [183] are located in this region, and the overtones of the main Ti–O-lines can also emerge. In addition, this region (2600–2760 cm^{-1}) contains the *G*' sp^2-C peak [11,177]. The shift and intensity of the *G*'-peak characterize the deviation in the 2-dimensional state of graphite relative to graphene [183,185]. The interaction between graphite layers causes a shift in the maximum of this peak, which is observed in our spectrum. The absorption maximum is at 2760 cm^{-1}, and G'-band as the graphene (no interaction) lies at 2700 cm^{-1}.

In the 3200–3800 cm^{-1} range, there are ν(OH) stretching vibrations in adsorbed water molecules. The presence of many poorly resolved lines in the 2500–3800 cm^{-1} region indicates the inhomogeneity of the state of hydroxyl groups on the surface of the black TiO_2 NTs.

3.7.3. Peculiarities of the carbon states in TiO_2 nanotubes

Some studies show that carbon had a crucial influence on the formation of black TiO_2 NTs when amorphous TiO_2 NTs prepared in ethylene glycol are heated in H_2. During the electrochemical oxidation of metals in electrolyte solutions, along with the main metal oxidation process, side chemical processes occur, including electrochemical transformations of electrolyte components. Thus, amorphous carbon and other carbon-containing products involved in the oxide film composition are formed using electrolytes containing carbon compounds. This phenomenon has been widely studied in the anodic oxidation of aluminum [10,11]. It is shown that amorphous carbon is formed along with carbonate-carboxylate ions under the electrochemical transformation of organic acids during the anodic oxidation of aluminum [11]. Amorphous carbon has also been shown to be a product of titanium anodic oxidation in ethylene glycol [63,64,104]. The XPS C1*s* spectrum indicates on the surface mainly amorphous carbon. The graphite-like carbon might also be present, but when oxidized or not fully conjugated, it is very difficult to identify this small portion of sp^2 carbon in the sp^3 signal. However, the Raman spectroscopy showed the presence of oxidized graphitic carbon in TiO_2 anodic films obtained in ethylene glycol. The quantitative ratio of these states depends on the heating conditions. Thus, graphitized carbon predominates in the samples heated in H_2.

According to the existing ideas about the mechanism of anodic oxidation of organic molecules [177,186], it might be assumed that dehydrogenation and dehydration reactions occur at the first stage of the process as follows:

$$2HOCH_2CH_2OH \rightarrow H_2 + 4H_2O + CH_2{=}CH{-}CH{=}CH_2$$

Breaking of the terminal C–H bonds, cyclization of polyene chains $(-CH{=}CH{-}CH{=}CH-)_n$, and formation of polycondensed aromatic compounds take place under heating samples in hydrogen. In the initial state at low temperature, a small amount of metamorphism is achieved (C:H<1) [171]. An increase in temperature intensifies the breaking of C–H bonds and causes the appearance of an unpaired electron density in the cyclic system. As the C:H ratio increases, the PC concentration grows, leading to the narrowing of the signals, which is observed in the spectra of H_2-treated samples. Heating in hydrogen effectively removes adsorbed oxygen and the formation of •C-radicals. An increase in the number of double bonds leads to an increase in the stability of radicals.

According to [171], stable •C-radicals are formed when an unpaired electron is located in the p_z-orbital of polyconjugated molecules with an odd number of aromatic carbon atoms. The localization of the unpaired electron density occurs on the carbon of polyconjugated six-membered networks, which is confirmed by the dependence of the EPR signal position on the orientation of the black TiO_2 NTs in a magnetic field. As follows from the quantum mechanical calculations reported in [171], the absorption of visible light in the entire range of the spectrum is due to polyconjugated aromatic systems with the number (n) of conjugated rings $8 < n < 100$ for linear and $6 < n < 50$ for nonlinear systems, as well as polyenes, for which $12 < n < 125$. Since the content of Ti^{3+} ions in the black TiO_2 NTs is low according to the data (2.86 at.%), it can be assumed that carbon contributes mainly to the black color of the samples. Thermal degradation, breaking of C–C and C–H bonds, and partial oxidation of carbon occur under heating in air. Carbon oxidation is indicated by XPS and FTIR spectra in which C–O functional groups are detected.

A specific characteristic of amorphous carbon is that it contains many randomly bound carbon atoms in sp^3 state that crosslink different layers and cause a distortion of the regularity of the structure. In the Raman spectra of the black TiO_2 NTs, *T*-peaks, which could be related to carbon atoms in sp^3 hybridization, are weakly pronounced, indicating the ordering of the structure of amorphous carbon and suggesting a 2*D* shape of graphite-like cyclic carbon networks on the wall surface of TiO_2 NTs. The symmetry distortion in carbon networks, which might be caused by the defects within the cycles and their small size, is reflected by the emergence of the *D*-peak in the Raman spectra. The observed intensity ratio of the I_D/I_G lines in the Raman spectrum of the black TiO_2 NTs may indicate that the carbon film is not single-layer or single-wall carbon nanotubes, and their structure is closer to two-layer double-wall carbon nanotubes [183].

The results presented above show the structure difference between the black TiO_2 NTs obtained by heating in hydrogen and the TiO_2 NTs samples obtained by heating in a vacuum [67]. After heating in hydrogen, we observe a small content of Ti^{3+} ions and a significant (two orders of magnitude) increase in the content of carbon radicals. Hydrogen only reduces the surface layer of titanium dioxide crystallites [164,187] and stimulates structural transformations in carbon-containing products [171]. Under heating in a vacuum, in contrast to hydrogen, the concentration of Ti^{3+} ions grows significantly [67]. It can be explained by more pronounced changes in titanium oxide structure. Along with the formation of oxygen vacancies, disturbances in the cationic sublattice in the form of interstitial titanium ions and cationic vacancies are possible, contributing to the additional stabilization of Ti^{3+} ions [188]. Heating in a vacuum and the processes associated with the structural rearrangements in TiO_2 facilitate the removal of carbon-containing inclusions.

The study results were summarized in scientific articles: 1) K. Chernyakova et al., Nature of paramagnetic defects in black titanium dioxide nanotubes, *Mater. Chem. Phys.* 278 (2022) 125703. DOI: 10.1016/j.matchemphys.2022.125703 and 2) K. Chernyakova et al., Synthesis and structural features of black TiO_2 nanotubes after annealing in hydrogen, *Mater. Chem. Phys.* 297 (2023) 127416. DOI: 10.1016/j.matchemphys.2023.127416.

CONCLUSIONS

1. The ammonium heptamolybdate and sodium metavanadate additives as corrosion inhibitors prevent aluminum dissolution at the initial stages of aluminum anodizing in formic acid solutions, thus increasing film growth rate and thickness. The oxalic acid additives also promote the anodic alumina film formation in the formic acid solution, preventing the pitting corrosion of aluminum. Moreover, oxalic acid additives improve film growth uniformity and morphology, forming an oxide layer with a smoother surface.
2. In the anodic alumina films obtained in the complex electrolytes containing formic acid, ammonium heptamolybdate, and oxalic acid, the average carbon content varies from 3.45 to 5.75 mass%, depending on electrolyte composition. It is 2.2 and 1.7 times higher than in oxalic and tartaric anodic alumina films, and the anodizing voltage is 80 V, which is comparable to the anodizing in oxalic acid solutions and 2.5 times lower than in tartaric acid solutions.
3. Carbonaceous species are embedded in the anodic alumina as CO_2 and CO molecules, carboxylate ions, and carbon species in the sp^2 and sp^3 states.
4. Anodic alumina films have a wide blue fluorescence in the wavelength range of 350–700 nm with a maximum at ca. 460 nm. The fluorescence decay is non-exponential and has an average lifetime of about 0.30 and 0.32 ns. The fluorescence spectrum is a superposition of several decay components. Besides oxygen vacancies, these are hydroxyl groups and carbonaceous species.
5. The carbonaceous species obtained during the aluminum anodic oxidation and embedded in the oxide matrix are luminescent and biocompatible carbon nanoparticles that can be extracted from the initial films. Carbon nanoparticle solutions exhibit an excitation-dependent emission behavior at 280–450 nm wavelengths with average lifetimes of 7.25–8.04 ns, depending on the composition of the initial film.
6. The carbonaceous species were also inserted in the anodic oxide films of titanium coloring in black. The carbon content on the surface of the black titania film formed in the ethylene-glycol-containing electrolyte is 20.1 ± 1 at.%, of which 13.8 at.% is graphite carbon.

BIBLIOGRAPHY

[1] W. Lee, S.J. Park, Porous anodic aluminum oxide: Anodization and templated synthesis of functional nanostructures, Chem. Rev. 114 (2014) 7487–7556. https://doi.org/10.1021/cr500002z.

[2] G. Patermarakis, K. Moussoutzanis, Mathematical models for the anodization conditions and structural features of porous anodic Al_2O_3 films on aluminum, J. Electrochem. Soc. 142 (1995) 737–743. https://doi.org/10.1149/1.2048527.

[3] G.D. Sulka, Introduction to anodization of metals, in: Nanostructured Anodic Met. Oxides Synth. Appl., Elsevier, 2020: pp. 1–34. https://doi.org/10.1016/B978-0-12-816706-9.00001-7.

[4] G.E.J. Poinern, N. Ali, D. Fawcett, Progress in nano-engineered anodic aluminum oxide membrane development, Materials (Basel). 4 (2011) 487–526. https://doi.org/10.3390/ma4030487.

[5] G.D. Sulka, Highly Ordered Anodic Porous Alumina Formation by Self-Organized Anodizing, in: Nanostructured Mater. Electrochem., Wiley, 2008: pp. 1–116. https://doi.org/10.1002/9783527621507.ch1.

[6] G.K. Mor, O.K. Varghese, M. Paulose, K. Shankar, C.A. Grimes, A review on highly ordered, vertically oriented TiO_2 nanotube arrays: Fabrication, material properties, and solar energy applications, Sol. Energy Mater. Sol. Cells. 90 (2006) 2011–2075. https://doi.org/10.1016/J.SOLMAT.2006.04.007.

[7] W.A. Abbas, I.H. Abdullah, B.A. Ali, N. Ahmed, A.M. Mohamed, M.Y. Rezk, N. Ismail, M.A. Mohamed, N.K. Allam, Recent advances in the use of TiO_2 nanotube powder in biological, environmental, and energy applications, (2019). https://doi.org/10.1039/c9na00339h.

[8] M. Shimura, S. Tajima, Organic compounds in aluminum oxide films anodized in aqueous solutions of carboxylic acids, Chem. Lett. 3 (1974) 1435–1438. https://doi.org/10.1246/cl.1974.1435.

[9] I. Vrublevsky, A. Jagminas, S. Hemeltjen, W. Goedel, Behavior of acid species during heat treatment and re-anodizing of porous alumina films formed in malonic acid, J Solid State Electrochem. 13 (2009) 1873–1880. https://doi.org/10.1007/s10008-008-0765-2.

[10] I.A. Vrublevsky, K. V. Chernyakova, A. Ispas, A. Bund, S. Zavadski, Optical properties of thin anodic alumina membranes formed in a solution of tartaric acid, Thin Solid Films. 556 (2014) 230–235. https://doi.org/10.1016/j.tsf.2014.01.074.

[11] K. Chernyakova, R. Karpicz, S. Zavadski, O. Poklonskaya, A. Jagminas, I. Vrublevsky, Structural and fluorescence characterization of anodic alumina/carbon composites formed in tartaric acid solution, J. Lumin. 182 (2017) 233–239. https://doi.org/10.1016/j.jlumin.2016.10.026.

[12] A. Jagminas, G. Grincienė, A. Selskis, K. Chernyakova, Cleavage of alumina cells in organic acid solutions during high voltage anodization, Phys. Chem. Chem. Phys. 21 (2019) 14941–14944. https://doi.org/10.1039/C9CP01466G.

[13] H. Bartzsch, D. Glöß, B. Böcher, P. Frach, K. Goedicke, Properties of

SiO_2 and Al_2O_3 films for electrical insulation applications deposited by reactive pulse magnetron sputtering, Surf. Coatings Technol. 174–175 (2003) 774–778. https://doi.org/10.1016/S0257-8972(03)00384-0.

[14] A.M. Md Jani, D. Losic, N.H. Voelcker, Nanoporous anodic aluminium oxide: Advances in surface engineering and emerging applications, Prog. Mater. Sci. 58 (2013) 636–704. https://doi.org/10.1016/j.pmatsci.2013.01.002.

[15] A. Ruiz-Clavijo, O. Caballero-Calero, M. Martín-González, Revisiting anodic alumina templates: from fabrication to applications, Nanoscale. 13 (2021) 2227–2265. https://doi.org/10.1039/D0NR07582E.

[16] G.E. Thompson, Porous anodic alumina: fabrication, characterization and applications, Thin Solid Films. 297 (1997) 192–201. https://doi.org/10.1016/S0040-6090(96)09440-0.

[17] S. Ono, M. Saito, M. Ishiguro, H. Asoh, Controlling factor of self-ordering of anodic porous alumina, J. Electrochem. Soc. 151 (2004) B473. https://doi.org/10.1149/1.1767838.

[18] Y. Smith, R. Ray, K. Carlson, B. Sarma, M. Misra, Self-ordered titanium dioxide nanotube arrays: anodic synthesis and their photo/electro-catalytic applications, Materials (Basel). 6 (2013) 2892–2957. https://doi.org/10.3390/ma6072892.

[19] V. Galstyan, N. Kaur, D. Zappa, E. Núñez-Carmona, V. Sberveglieri, E. Comini, From conventional to energy-efficient and biocompatible composite structures, Sensors. 20 (2020) 579. https://doi.org/10.3390/s20030579.

[20] K. Indira, U.K. Mudali, T. Nishimura, N. Rajendran, A review on TiO_2 nanotubes: influence of anodization parameters, formation mechanism, properties, corrosion behavior, and biomedical applications, J. Bio- Tribo-Corrosion. 1 (2015) 28. https://doi.org/10.1007/s40735-015-0024-x.

[21] V. Likodimos, T. Stergiopoulos, P. Falaras, J. Kunze, P. Schmuki, Phase composition, size, orientation, and antenna effects of self-assembled anodized titania nanotube arrays: a polarized micro-raman investigation, J. Phys. Chem. C. 112 (2008) 12687–12696. https://doi.org/10.1021/jp8027462.

[22] A. Naldoni, M. Altomare, G. Zoppellaro, N. Liu, Š. Kment, R. Zbořil, P. Schmuki, Photocatalysis with reduced TiO_2: From Black TiO_2 to cocatalyst-free hydrogen production, ACS Catal. 9 (2019) 345–364. https://doi.org/10.1021/acscatal.8b04068.

[23] A.M. Brudzisz, D. Giziński, W.J. Stępniowski, Incorporation of ions into nanostructured anodic oxides—mechanism and functionalities, Molecules. 26 (2021) 6378. https://doi.org/10.3390/molecules26216378.

[24] R. Giovanardi, C. Fontanesi, W. Dallabarba, Adsorption of organic compounds at the aluminium oxide/aqueous solution interface during the aluminium anodizing process, Electrochim. Acta. 56 (2011) 3128–3138. https://doi.org/10.1016/J.ELECTACTA.2011.01.065.

[25] A.K. Eessaa, A.M. El-Shamy, Review on fabrication, characterization, and applications of porous anodic aluminum oxide films with tunable pore sizes for emerging technologies, Microelectron. Eng. 279 (2023) 112061. https://doi.org/10.1016/J.MEE.2023.112061.

[26] H. Hashimoto, K. Yazawa, H. Asoh, S. Ono, NMR spectroscopic analysis of the local structure of porous-type amorphous alumina prepared by anodization, J. Phys. Chem. C. 121 (2017) 12300–12307. https://doi.org/10.1021/acs.jpcc.7b03629.

[27] H. Hashimoto, Y. Fujita, K. Yazawa, H. Asoh, Effects of anion incorporation on the local structure of porous-type amorphous alumina prepared by anodization: NMR study of Al coordination numbers, Results Phys. 44 (2023) 106177. https://doi.org/10.1016/J.RINP.2022.106177.

[28] C.A. Melendres, S. Van Gils, H. Terryn, Toward a quantitative description of the anodic oxide films on aluminum, Electrochem. Commun. 3 (2001) 737–741. https://doi.org/10.1016/S1388-2481(01)00250-8.

[29] N.M. Yakovleva, A.N. Yakovlev, E.A. Chupakhina, Structural analysis of alumina films produced by two-step electrochemical oxidation, Thin Solid Films. 366 (2000) 37–42. https://doi.org/10.1016/S0040-6090(00)00886-5.

[30] P.P. Mardilovich, A.N. Govyadinov, N.I. Mukhurov, A.M. Rzhevskii, R. Paterson, New and modified anodic alumina membranes Part I. Thermotreatment of anodic alumina membranes, J. Memb. Sci. 98 (1995) 131–142. https://doi.org/10.1016/0376-7388(94)00184-Z.

[31] J. De Laet, H. Terryn, J. Vereecken, J. Vanhellemont, Spectroscopic ellipsometry characterization of anodic films on aluminium correlated with transmission electron microscopy and Auger electron spectroscopy, Surf. Interface Anal. 19 (1992) 445–449. https://doi.org/10.1002/sia.740190183.

[32] G.C. Wood, P. Skeldon, G.E. Thompson, K. Shimizu, A model for the incorporation of electrolyte species into anodic alumina, J. Electrochem. Soc. 143 (1996) 74–83. https://doi.org/10.1149/1.1836389.

[33] K. Shimizu, G.M. Brown, H. Habazaki, K. Kobayashi, P. Skeldon, G.E. Thompson, G.C. Wood, Impurity distributions in barrier anodic films on aluminium: a GDOES depth profiling study, Electrochim. Acta. 44 (1999) 2297–2306. https://doi.org/10.1016/S0013-4686(98)00355-7.

[34] B.G.M.. H.H.. K.K.. S.P.. T.G.E.. W.G.C. Shimizu K., Influence of surface roughness on the depth resolution of GDOES depth profiling analysis, Surf. Interface Anal. 27 (1999) 153–156.

[35] S.-Z. Kure-Chu, K. Osaka, H. Yashiro, H. Segawa, K. Wada, S. Inoue, Controllable fabrication of networked three-dimensional nanoporous anodic alumina films on low-purity Al materials, J. Electrochem. Soc. 162 (2015) C24–C34. https://doi.org/10.1149/2.0511501jes.

[36] Y. Yamamoto, N. Baba, S. Tajima, Coloured materials and photoluminescence centres in anodic film on aluminium, Nature. 289 (1981) 572–574. https://doi.org/10.1038/289572a0.

[37] S. Tajima, Luminescence, breakdown and colouring of anodic oxide films on aluminium, Electrochim. Acta. 22 (1977) 995–1011. https://doi.org/10.1016/0013-4686(77)85011-1.

[38] M. Shimura, Behavior of maleic acid during the anodization of aluminum, J. Electrochem. Soc. 125 (1978) 190–193. https://doi.org/10.1149/1.2131411.

[39] I. Vrublevsky, A. Jagminas, J. Schreckenbach, W.A. Goedel, Electronic

properties of electrolyte/anodic alumina junction during porous anodizing, Appl. Surf. Sci. 253 (2007) 4680–4687. https://doi.org/10.1016/J.APSUSC.2006.10.038.

[40] J. Wang, K.N. Vu, A.D. Abell, A. Santos, C.S. Law, Nanoporous anodic alumina-based iontronics: fundamentals and applications, J. Mater. Chem. C. 11 (2023) 9051–9081. https://doi.org/10.1039/D3TC01735D.

[41] Y. Yamamoto, N. Baba, Nature of the carboxylate species incorporated in anodic alumina films formed in oxalic acid solution, Thin Solid Films. 101 (1983) 329–338. https://doi.org/10.1016/0040-6090(83)90099-8.

[42] K. Shimizu, H. Habazaki, P. Skeldon, G.E. Thompson, G.C. Wood, Migration of oxalate ions in anodic alumina, Electrochim. Acta. 46 (2001) 4379–4382. https://doi.org/10.1016/S0013-4686(01)00660-0.

[43] S.J. Garcia-Vergara, H. Habazaki, P. Skeldon, G.E. Thompson, Formation of porous anodic alumina at high current efficiency, Nanotechnology. 18 (2007) 415605. https://doi.org/10.1088/0957-4484/18/41/415605.

[44] S.P. Eremenko, D.B. Sandulov, L.I. Kolomiets, O.N. Malinovskaya, Infrared spectra of anodic oxide films, J. Appl. Spectrosc. 35 (1981) 791–796. https://doi.org/10.1007/BF00620350.

[45] I. Mínguez-Bacho, S. Rodríguez-López, A. Climent-Font, D. Fichou, M. Vázquez, M. Hernández-Vélez, Variation of the refractive index by means of sulfate anion incorporation into nanoporous anodic aluminum oxide films, Microporous Mesoporous Mater. 225 (2016) 192–197. https://doi.org/10.1016/j.micromeso.2015.12.011.

[46] D.H. Fan, G.Q. Ding, W.Z. Shen, M.J. Zheng, Anion impurities in porous alumina membranes: Existence and functionality, Microporous Mesoporous Mater. 100 (2007) 154–159. https://doi.org/10.1016/j.micromeso.2006.10.025.

[47] S. Stojadinovic, R. Vasilic, Characterization of porous anodic aluminum oxide films by luminescence methods - A Review, Curr. Nanosci. 11 (2015) 547–559. https://doi.org/10.2174/1573413711999150608144529.

[48] L.K. Acosta, C.S. Law, A. Santos, J. Ferré-Borrull, L.F. Marsal, Tuning intrinsic photoluminescence from light-emitting multispectral nanoporous anodic alumina photonic crystals, APL Photonics. 7 (2022) 026108. https://doi.org/10.1063/5.0078505.

[49] A.A. Jagminas, S. Kaciulis, V. Klimas, A. Rèza, S. Mickevicius, P. Soltani, A. Rėza, S. Mickevicius, P. Soltani, A. Rèza, S. Mickevicius, P. Soltani, A. Rėza, S. Mickevicius, P. Soltani, Fabrication of graphene-alumina heterostructured films with nanotube morphology, J. Phys. Chem. C. 120 (2016) 9490–9497. https://doi.org/10.1021/acs.jpcc.6b01416.

[50] T. Fukushima, Y. Fukuda, G. Ito, Y. Sato, Anodic oxidation and local corrosion of aluminum in mono-carboxylic acids, J. Met. Finish. Soc. Japan. 21 (1970) 319–326. https://doi.org/10.4139/sfj1950.21.319.

[51] H. Noguchi, C. Yoshimura, Effect of fluoride on anodization of aluminum in mono-carboxylic acid baths., J. Met. Finish. Soc. Japan. 38 (1987) 133–137. https://doi.org/10.4139/sfj1950.38.133.

[52] M. Pashchanka, J.J. Schneider, Origin of self-organisation in porous anodic alumina films derived from analogy with Rayleigh–Bénard convection cells, J. Mater. Chem. 21 (2011) 18761–18767.

https://doi.org/10.1039/c1jm13898g.

[53] V. Klimas, A. Naujokaitis, S. Jankauskas, A. Jagminas, Anodising of aluminium in formate solutions with formation of porous alumina arrays, Trans. IMF. 100 (2022) 333–341. https://doi.org/10.1080/00202967.2022.2110305.

[54] W. Bensalah, M. Feki, M. Wery, H.F. Ayedi, Chemical dissolution resistance of anodic oxide layers formed on aluminum, Trans. Nonferrous Met. Soc. China English Ed. 21 (2011) 1673–1679. https://doi.org/10.1016/S1003-6326(11)60913-8.

[55] V. Moutarlier, M.P. Gigandet, J. Pagetti, L. Ricq, Molybdate/sulfuric acid anodising of 2024-aluminium alloy: influence of inhibitor concentration on film growth and on corrosion resistance, Surf. Coatings Technol. 173 (2003) 87–95. https://doi.org/10.1016/S0257-8972(03)00511-5.

[56] V. Moutarlier, M.P. Gigandet, J. Pagetti, B. Normand, Influence of oxalic acid addition to chromic acid on the anodising of Al 2024 alloy, Surf. Coatings Technol. 182 (2004) 117–123. https://doi.org/10.1016/S0257-8972(03)00875-2.

[57] V. Moutarlier, M.P. Gigandet, L. Ricq, J. Pagetti, Electrochemical characterisation of anodic oxidation films formed in presence of corrosion inhibitors, Appl. Surf. Sci. 183 (2001) 1–9. https://doi.org/10.1016/S0169-4332(01)00364-6.

[58] M. García-Rubio, P. Ocón, A. Climent-Font, R.W. Smith, M. Curioni, G.E. Thompson, P. Skeldon, A. Lavía, I. García, Influence of molybdate species on the tartaric acid/sulphuric acid anodic films grown on AA2024 T3 aerospace alloy, Corros. Sci. 51 (2009) 2034–2042. https://doi.org/10.1016/J.CORSCI.2009.05.034.

[59] M. Sieber, R. Morgenstern, I. Scharf, T. Lampke, Effect of nitric and oxalic acid addition on hard anodizing of $AlCu_4Mg_1$ in sulphuric acid, Metals (Basel). 8 (2018) 1–15. https://doi.org/10.3390/met8020139.

[60] V. Moutarlier, M.P. Gigandet, J. Pagetti, S. Linget, Influence of molybdate species added to sulphuric acid on composition and morphology of the anodic layers formed on 2024 aluminium alloy, Thin Solid Films. 483 (2005) 197–204. https://doi.org/10.1016/J.TSF.2004.12.020.

[61] D.R. Gabe, S.E. Gould, Black molybdate conversion coatings, Surf. Coatings Technol. 35 (1988) 79–91. https://doi.org/10.1016/0257-8972(88)90059-X.

[62] Thompson G. E., Skeldon P., Shimizu K., Wood G., The compositions of barrier-type anodic films formed on aluminium in molybdate and tungstate electrolytes, Philos. Trans. R. Soc. London. Ser. A Phys. Eng. Sci. 350 (1995) 143–168. https://doi.org/10.1098/rsta.1995.0005.

[63] S.K. Mohapatra, M. Misra, V.K. Mahajan, K.S. Raja, Design of a highly efficient photoelectrolytic cell for hydrogen generation by water splitting, Society. (2007) 8677–8685. http://pubs.acs.org/doi/abs/10.1021/jp071906v.

[64] P. Roy, S. Berger, P. Schmuki, TiO_2 Nanotubes: Synthesis and Applications, Angew. Chemie Int. Ed. 50 (2011) 2904–2939. https://doi.org/https://doi.org/10.1002/anie.201001374.

[65] S.K. Mohapatra, M. Misra, V.K. Mahajan, K.S. Raja, A novel method for the synthesis of titania nanotubes using sonoelectrochemical method and its application for photoelectrochemical splitting of water, J. Catal. 246 (2007) 362–369. https://doi.org/10.1016/J.JCAT.2006.12.020.

[66] J. Winiarski, W. Tylus, M. Pawlyta, B. Szczygieł, Titanium anodization in deep eutectic solvents: The effect of anodizing time on the morphology and structure of anodic layers, Appl. Surf. Sci. 577 (2022) 151892. https://doi.org/10.1016/J.APSUSC.2021.151892.

[67] D. Pan, H. Huang, X. Wang, L. Wang, H. Liao, Z. Li, M. Wu, C-axis preferentially oriented and fully activated TiO_2 nanotube arrays for lithium ion batteries and supercapacitors, J. Mater. Chem. A. 2 (2014) 11454–11464. https://doi.org/10.1039/C4TA01613K.

[68] J.H. Park, S. Kim, A.J. Bard, Novel carbon-doped TiO_2 nanotube arrays with high aspect ratios for efficient solar water splitting, Nano Lett. 6 (2006) 24–28. https://doi.org/10.1021/nl051807y.

[69] A.B. Murphy, Does carbon doping of TiO_2 allow water splitting in visible light? Comments on "Nanotube enhanced photoresponse of carbon modified (CM)-n-TiO_2 for efficient water splitting," Sol. Energy Mater. Sol. Cells. 92 (2008) 363–367. https://doi.org/10.1016/J.SOLMAT.2007.10.007.

[70] Y.C. Zhu, C.X. Ding, Oriented growth of nano-TiO_2 whiskers, Nanostructured Mater. 11 (1999) 427–431. https://doi.org/10.1016/S0965-9773(99)00323-2.

[71] W. Stępniowski, M. Norek, M. Michalska-Domańska, A. Nowak-Stępniowska, M. Kaliszewski, P. Chilimoniuk, A. Bombalska, Z. Bojar, Fabrication and luminescence of anodic alumina with incorporated vanadyl citrate chelate anions, J. Mater. Sci. Nanotechnol. 1 (2014). https://doi.org/10.15744/2348-9812.1.S102.

[72] A. Santos, T. Kumeria, D. Losic, Optically optimized photoluminescent and interferometric biosensors based on nanoporous anodic alumina: A comparison, Anal. Chem. 85 (2013) 7904–7911. https://doi.org/10.1021/AC401609C.

[73] S.Y. Li, Z.L. Liu, G.X. Xiang, B.H. Ma, Photoluminescence properties of anodic aluminium oxide films formed in a mixture of malonic acid and oxalic acid, Luminescence. 37 (2022) 1864–1872. https://doi.org/10.1002/BIO.4363.

[74] L. Cantelli, J.S. Santos, T.F. Silva, M.H. Tabacniks, A.O. Delgado-Silva, F. Trivinho-Strixino, Unveiling the origin of photoluminescence in nanoporous anodic alumina (NAA) obtained by constant current regime, J. Lumin. 207 (2019) 63–69. https://doi.org/10.1016/J.JLUMIN.2018.10.015.

[75] X. Sun, F. Xu, Z. Li, W. Zhang, Photoluminescence properties of anodic alumina membranes with ordered nanopore arrays, J. Lumin. 121 (2006) 588–594. https://doi.org/10.1016/J.JLUMIN.2005.12.057.

[76] Z. Li, K. Huang, The effect of high-temperature annealing on optical properties of porous anodic alumina formed in oxalic acid, Luminescence. 22 (2007) 355–361. https://doi.org/10.1002/bio.971.

[77] Z.J. Li, K.L. Huang, Optical properties of alumina membranes prepared

by anodic oxidation process, J. Lumin. 127 (2007) 435–440. https://doi.org/10.1016/J.JLUMIN.2007.02.001.

[78] J. Robertson, Diamond-like amorphous carbon, Mater. Sci. Eng. R Reports. 37 (2002) 129–281. https://doi.org/10.1016/S0927-796X(02)00005-0.

[79] C. Lin, M. Yu, Z. Cheng, C. Zhang, Q. Meng, J. Lin, Bluish-white emission from radical carbonyl impurities in amorphous Al 2 O 3 prepared via the Pechini-type sol−gel process, Inorg. Chem. 47 (2008) 49–55. https://doi.org/10.1021/ic700652v.

[80] T. Gao, G. Meng, L. Zhang, Blue luminescence in porous anodic alumina films: the role of the oxalic impurities, J. Phys. Condens. Matter. 15 (2003) 2071–2079. https://doi.org/10.1088/0953-8984/15/12/324.

[81] M. Rückschloss, T. Wirschem, H. Tamura, G. Ruhl, J. Oswald, S. Veprek, Photoluminescence from OH-related radiative centres in silica, metal oxides and oxidized nanocrystalline and porous silicon, J. Lumin. 63 (1995) 279–287. https://doi.org/10.1016/0022-2313(94)00076-O.

[82] C.W. Wang, C. Liang, H.J. Yeh, Aquatic acute toxicity assessments of molybdenum (+VI) to Daphnia magna, Chemosphere. 147 (2016) 82–87. https://doi.org/10.1016/J.CHEMOSPHERE.2015.12.052.

[83] F.A. Cotton, G. Wilkinson, C.A. Murillo, M. Bochmann, Advanced inorganic chemistry, 6th ed., John Wiley & Sons, Inc., 1999.

[84] H. Maltanava, S. Poznyak, M. Ivanovskaya, N. Scharnagl, M. Starykevich, A.N. Salak, M. de Rosário Soares, A. Mazanik, Effect of fluoride-mediated transformations on electrocatalytic performance of thermally treated TiO_2 nanotubular layers, J. Fluor. Chem. 221 (2019) 34–41. https://doi.org/10.1016/j.jfluchem.2019.02.006.

[85] I. Vrublevsky, A. Ispas, K. Chernyakova, A. Bund, Effect of continuous magnetic field on the growth mechanism of nanoporous anodic alumina films on different substrates, J. Solid State Electrochem. 20 (2016). https://doi.org/10.1007/s10008-016-3274-8.

[86] K. Nakamoto, Infrared and Raman Spectra of Inorganic and Coordination Compounds, Wiley, 2008. https://doi.org/10.1002/9780470405840.

[87] F. Fondeur, J.L. Koenig, FT-IR Characterization of the Surface of Aluminum as a Result of Chemical Treatment, J. Adhes. 40 (1993) 189–205. https://doi.org/10.1080/00218469308031284.

[88] S. Kaciulis, Spectroscopy of carbon: from diamond to nitride films, Surf. Interface Anal. 44 (2012) 1155–1161. https://doi.org/10.1002/sia.4892.

[89] A. Mezzi, S. Kaciulis, Surface investigation of carbon films: from diamond to graphite, Surf. Interface Anal. 42 (2010) 1082–1084. https://doi.org/10.1002/sia.3348.

[90] A.C. Ferrari, J. Robertson, Resonant Raman spectroscopy of disordered, amorphous, and diamondlike carbon, Phys. Rev. B. 64 (2001) 075414. https://doi.org/10.1103/PhysRevB.64.075414.

[91] H. Maltanava, S. Poznyak, M. Starykevich, M. Ivanovskaya, Electrocatalytic activity of Au nanoparticles onto TiO_2 nanotubular layers in oxygen electroreduction reaction: size and support effects, Electrochim. Acta. 222 (2016) 1013–1020. https://doi.org/10.1016/J.ELECTACTA.2016.11.070.

[92] R. W. Fessenden, Introduction to magnetic resonance: with applications to chemistry and chemical physics (Carrington, Alan; McLachlan, Andre D.), J. Chem. Educ. 44 (1967). https://doi.org/10.1021/ed044p772.2.

[93] E. Daublytė, M. Kalnaitytė, A. Klimovich, A. Drabavičius, T. Charkova, Synthesis of silver nanoparticles with polyols under reflux and microwave irradiation conditions, Chemija. 34 (2023) 133–122. https://doi.org/10.6001/chemija.2023.34.3.1.

[94] J. Lemerle, L. Nejem, J. Lefebvre, Condensation process in polyvanadic acid solutions, J. Inorg. Nucl. Chem. 42 (1980) 17–20. https://doi.org/10.1016/0022-1902(80)80036-4.

[95] D. Ifezue, Certified reference materials for quantification of vanadate species in anodic alumina Rf-GDOES depth profiles, J. Anal. At. Spectrom. 28 (2013) 1311. https://doi.org/10.1039/c3ja50061f.

[96] A. Jagminas, S. Kaciulis, V. Klimas, A. Rèza, S. Mickevicius, P. Soltani, Fabrication of graphene-alumina heterostructured films with nanotube morphology, J. Phys. Chem. C. 120 (2016) 9490–9497. https://doi.org/10.1021/acs.jpcc.6b01416.

[97] G. Silversmit, D. Depla, H. Poelman, G.B. Marin, R. De Gryse, Determination of the V2*p* XPS binding energies for different vanadium oxidation states (V^{5+} to VO^{+}), J. Electron Spectros. Relat. Phenomena. 135 (2004) 167–175. https://doi.org/10.1016/J.ELSPEC.2004.03.004.

[98] M.C. Biesinger, L.W.M. Lau, A.R. Gerson, R.S.C. Smart, Resolving surface chemical states in XPS analysis of first row transition metals, oxides and hydroxides: Sc, Ti, V, Cu and Zn, Appl. Surf. Sci. 257 (2010) 887–898. https://doi.org/10.1016/J.APSUSC.2010.07.086.

[99] Y. Mizokawa, T. Miyasato, S. Nakamura, K.M. Geib, C.W. Wilmsen, Comparison of the CKLL first-derivative auger spectra from XPS and AES using diamond, graphite, SiC and diamond-like-carbon films, Surf. Sci. 182 (1987) 431–438. https://doi.org/10.1016/0039-6028(87)90011-2.

[100] T. Aerts, I. De Graeve, H. Terryn, Study of initiation and development of local burning phenomena during anodizing of aluminium under controlled convection, Electrochim. Acta. 54 (2008) 270–279. https://doi.org/10.1016/j.electacta.2008.08.004.

[101] T. Kikuchi, D. Nakajima, J. Kawashima, S. Natsui, R.O. Suzuki, Fabrication of anodic porous alumina via anodizing in cyclic oxocarbon acids, Appl. Surf. Sci. 313 (2014) 276–285. https://doi.org/10.1016/j.apsusc.2014.05.204.

[102] M. Pashchanka, G. Cherkashinin, A strategy towards light-absorbing coatings based on optically black nanoporous alumina with tailored disorder, Materials (Basel). 14 (2021) 5827. https://doi.org/10.3390/ma14195827.

[103] K. Schwirn, W. Lee, R. Hillebrand, M. Steinhart, K. Nielsch, U. Gösele, Self-ordered anodic aluminum oxide formed by H_2SO_4 hard anodization, ACS Nano. 2 (2008) 302–310. https://doi.org/10.1021/nn7001322.

[104] S.K. Mohapatra, M. Misra, V.K. Mahajan, K.S. Raja, Design of a highly efficient photoelectrolytic cell for hydrogen generation by water splitting: Application of $TiO_{2-x}C_x$ nanotubes as a photoanode and Pt/TiO2 nanotubes a a cathode, J. Phys. Chem. C. 111 (2007) 8677–8685.

https://doi.org/10.1021/jp071906v.

[105] I. Vrublevsky, K. Chernyakova, R. Karpicz, A. Jagminas, Stored charge and its influence on properties of anodic alumina films, Curr. Nanosci. 15 (2018) 100–109. https://doi.org/10.2174/1573413714666180430140039.

[106] K. Chernyakova, I. Vrublevsky, V. Klimas, A. Jagminas, Effect of Joule heating on formation of porous structure of thin oxalic acid anodic alumina films, J. Electrochem. Soc. 165 (2018) E289–E293. https://doi.org/10.1149/2.1001807jes.

[107] W. Cheng, M. Steinhart, U. Gösele, R.B. Wehrspohn, Tree-like alumina nanopores generated in a non-steady-state anodization, J. Mater. Chem. 17 (2007) 3493. https://doi.org/10.1039/b709618f.

[108] T. Gong, C. Li, X. Li, H. Yue, X. Zhu, Z. Zhao, R. Lv, J. Zhu, Evidence of oxygen bubbles forming nanotube embryos in porous anodic oxides, Nanoscale Adv. 3 (2021) 4659–4668. https://doi.org/10.1039/D1NA00389E.

[109] A.C. Crossland, H. Habazaki, K. Shimizu, P. Skeldon, G.E. Thompson, G.C. Wood, X. Zhou, C.J.E. Smith, Residual flaws due to formation of oxygen bubbles in anodic alumina, Corros. Sci. 41 (1999) 1945–1954. https://doi.org/10.1016/S0010-938X(99)00035-9.

[110] K. Shimizu, H. Habazaki, P. Skeldon, G. Thompson, G. Wood, Role of metal ion impurities in generation of oxygen gas within anodic alumina, Electrochim. Acta. 47 (2002) 1225–1228. https://doi.org/10.1016/S0013-4686(01)00836-2.

[111] J.M. Albella, I. Montero, J.M. Martinez-Duart, A theory of avalanche breakdown during anodic oxidation, Electrochim. Acta. 32 (1987) 255–258. https://doi.org/10.1016/0013-4686(87)85032-6.

[112] A. Cuesta, G. Cabello, C. Gutiérrez, M. Osawa, Adsorbed formate: the key intermediate in the oxidation of formic acid on platinum electrodes, Phys. Chem. Chem. Phys. 13 (2011) 20091. https://doi.org/10.1039/c1cp22498k.

[113] J. Szatkowski, S. Kulesza, A. Korcala, M. Rebarz, M. Wojdyła, G. Trykowski, W. Bala, F. Rozploch, Structural and photoluminescence study of diamond-like layers grown by electrochemical method, Optoelectron. Adv. Mater. Commun. 2 (2008) 46–49.

[114] V.P. Novikov, V.P. Dymont, Synthesis of diamondlike films by an electrochemical method at atmospheric pressure and low temperature, Appl. Phys. Lett. 70 (1997) 200–202. https://doi.org/10.1063/1.118355.

[115] A.H.C. Sirk, D.R. Sadoway, Electrochemical synthesis of diamond-like carbon films, J. Electrochem. Soc. 155 (2008) E49. https://doi.org/10.1149/1.2883729.

[116] X.B. Yan, T. Xu, S.R. Yang, H.W. Liu, Q.J. Xue, Characterization of hydrogenated diamond-like carbon films electrochemically deposited on a silicon substrate, J. Phys. D. Appl. Phys. 37 (2004) 2416–2424. https://doi.org/10.1088/0022-3727/37/17/012.

[117] X. Zhou, G.E. Thompson, H. Habazaki, M.A. Paez, K. Shimizu, P. Skeldon, G.C. Wood, Morphological development of oxygen bubbles in anodic alumina, J. Electrochem. Soc. 147 (2000) 1747. https://doi.org/10.1149/1.1393428.

[118] A.P. Leontiev, I. V. Roslyakov, K.S. Napolskii, Complex influence of temperature on oxalic acid anodizing of aluminium, Electrochim. Acta. 319 (2019) 88–94. https://doi.org/10.1016/j.electacta.2019.06.111.

[119] I. V. Roslyakov, E.O. Gordeeva, K.S. Napolskii, Role of electrode reaction kinetics in self-ordering of porous anodic alumina, Electrochim. Acta. 241 (2017) 362–369. https://doi.org/10.1016/j.electacta.2017.04.140.

[120] V. Vega, J. García, J.M. Montero-Moreno, B. Hernando, J. Bachmann, V.M. Prida, K. Nielsch, Unveiling the hard anodization regime of aluminum: Insight into nanopores self-organization and growth mechanism, ACS Appl. Mater. Interfaces. 7 (2015) 28682–28692. https://doi.org/10.1021/acsami.5b10712.

[121] W. Wang, P. Dong, H. Wang, J. Cheng, S. Liu, W. Wenbo, D. Peng, W. Haiyun, C. Jie, L. Shengli, Synergistic corrosion inhibition effect of molybdate and phosphate ions for anodic oxidation film formed on 2024 aluminum alloy, J. Wuhan Univ. Technol. Mater. Sci. Ed. 34 (2019) 426–432. https://doi.org/10.1007/s11595-019-2069-z.

[122] D. Ifezue, Certified reference materials for quantification of vanadate species in anodic alumina Rf-GDOES depth profiles, J. Anal. At. Spectrom. 28 (2013) 1311–1319. https://doi.org/10.1039/c3ja50061f.

[123] I. Vrublevsky, K. Chernyakova, A. Bund, A. Ispas, U. Schmidt, Effect of anodizing voltage on the sorption of water molecules on porous alumina, Appl. Surf. Sci. 258 (2012) 5394–5398. https://doi.org/10.1016/j.apsusc.2012.02.020.

[124] T. Masuda, H. Asoh, S. Haraguchi, S. Ono, Nanoporous alpha-alumina membrane prepared by anodizing and heat treatment, Electrochemistry. 82 (2014) 448–455. https://doi.org/10.5796/electrochemistry.82.448.

[125] C. Morterra, G. Magnacca, A case study: Surface chemistry and surface structure of catalytic aluminas, as studied by vibrational spectroscopy of adsorbed species, Catal. Today. 27 (1996) 497–532. https://doi.org/10.1016/0920-5861(95)00163-8.

[126] C. Morterra, C. Emanuel, G. Cerrato, G. Magnacca, Infrared study of some surface properties of boehmite (γ-AlO_2H), J. Chem. Soc., Faraday Trans. 88 (1992) 339–348. https://doi.org/10.1039/FT9928800339.

[127] J.C. Lascovich, A. Santoni, Study of the occupied electronic density of states of carbon samples by using second derivative carbon KVV Auger spectra, Appl. Surf. Sci. 103 (1996) 245–253. https://doi.org/10.1016/0169-4332(96)00526-0.

[128] B. Lesiak, L. Kövér, J. Tóth, J. Zemek, P. Jiricek, A. Kromka, N. Rangam, C sp^2/sp^3 hybridisations in carbon nanomaterials – XPS and (X)AES study, Appl. Surf. Sci. 452 (2018) 223–231. https://doi.org/10.1016/j.apsusc.2018.04.269.

[129] S. Ono, M. Saito, H. Asoh, Self-ordering of anodic porous alumina formed in organic acid electrolytes, Electrochim. Acta. 51 (2005) 827–833. https://doi.org/10.1016/J.ELECTACTA.2005.05.058.

[130] I. V. Roslyakov, D.S. Koshkodaev, A.A. Eliseev, D. Hermida-Merino, V.K. Ivanov, A. V. Petukhov, K.S. Napolskii, Growth of porous anodic alumina on low-index surfaces of Al single crystals, J. Phys. Chem. C.

121 (2017) 27511–27520. https://doi.org/10.1021/acs.jpcc.7b09998.

[131] W. Lee, R. Ji, U. Gösele, K. Nielsch, Fast fabrication of long-range ordered porous alumina membranes by hard anodization, Nat. Mater. 5 (2006) 741–747. https://doi.org/10.1038/nmat1717.

[132] K. Chernyakova, B. Tzaneva, I. Vrublevsky, V. Videkov, Effect of Aluminum Anode Temperature on Growth Rate and Structure of Nanoporous Anodic Alumina, J. Electrochem. Soc. 167 (2020) 103506. https://doi.org/10.1149/1945-7111/ab9d65.

[133] R. Ozao, H. Yoshida, Y. Ichimura, T. Inada, M. Ochiai, Crystallization of anodic alumina membranes studied by simultaneous TG-DTA/FTIR, 2001.

[134] T. Masuda, H. Asoh, S. Haraguchi, S. Ono, Fabrication and characterization of single phase α-alumina membranes with tunable pore diameters, Materials (Basel). 8 (2015) 1350–1368. https://doi.org/10.3390/ma8031350.

[135] A. Ruiz-Clavijo, O. Caballero-Calero, M. Martín-González, Revisiting anodic alumina templates: from fabrication to applications, Nanoscale. 13 (2021) 2227–2265. https://doi.org/10.1039/D0NR07582E.

[136] S.Z. Chu, K. Wada, S. Inoue, M. Isogai, Y. Katsuta, A. Yasumori, Large-scale fabrication of ordered nanoporous alumina films with arbitrary pore intervals by critical-potential anodization, J. Electrochem. Soc. 153 (2006) B384. https://doi.org/10.1149/1.2218822.

[137] K.S. Shamala, L.C.S. Murthy, K.N. Rao, Studies on optical and dielectric properties of Al2O3 thin films prepared by electron beam evaporation and spray pyrolysis method, Mater. Sci. Eng. B. 106 (2004) 269–274. https://doi.org/10.1016/J.MSEB.2003.09.036.

[138] P.R. Reddy, K.M. Ajith, N.K. Udayashankar, Optical and mechanical studies on free standing amorphous anodic porous alumina formed in oxalic and sulphuric acid, Appl. Phys. A. 124 (2018) 765. https://doi.org/10.1007/s00339-018-2163-7.

[139] J. Wang, C.W. Wang, Y. Li, W.M. Liu, Optical constants of anodic aluminum oxide films formed in oxalic acid solution, Thin Solid Films. 516 (2008) 7689–7694. https://doi.org/10.1016/J.TSF.2008.03.023.

[140] C. V. Ramana, R.J. Smith, O.M. Hussain, C.C. Chusuei, C.M. Julien, Correlation between growth conditions, microstructure, and optical properties in pulsed-laser-deposited V2O5 thin films, Chem. Mater. 17 (2005) 1213–1219. https://doi.org/10.1021/cm048507m.

[141] A.D. Rakić, Algorithm for the determination of intrinsic optical constants of metal films: application to aluminum, Appl. Opt. 34 (1995) 4755. https://doi.org/10.1364/AO.34.004755.

[142] S. Ozcan, S. Vempati, A. Çırpan, T. Uyar, Associative behaviour and effect of functional groups on the fluorescence of graphene oxide, Phys. Chem. Chem. Phys. 20 (2018) 7559–7569. https://doi.org/10.1039/C7CP08334C.

[143] J. Li, W. Wang, B.L. An, X. Jia, Y.H. Zhang, J.R. Li, Y.L. Bai, J.Q. Xu, Luminescence color regulation of carbon quantum dots by surface modification, J. Lumin. 246 (2022) 118811. https://doi.org/10.1016/J.JLUMIN.2022.118811.

[144] S. Samimi, N. Maghsoudnia, R.B. Eftekhari, F. Dorkoosh, Lipid-Based Nanoparticles for Drug Delivery Systems, in: Charact. Biol. Nanomater. Drug Deliv., Elsevier, 2019: pp. 47–76. https://doi.org/10.1016/B978-0-12-814031-4.00003-9.

[145] C. Zheng, L. Huang, Q. Guo, W. Chen, W. Li, H. Wang, Facile one-step fabrication of upconversion fluorescence carbon quantum dots anchored on graphene with enhanced nonlinear optical responses, RSC Adv. 8 (2018) 10267–10276. https://doi.org/10.1039/C8RA00390D.

[146] Y. Wang, A. Hu, Carbon quantum dots: synthesis, properties and applications, J. Mater. Chem. C. 2 (2014) 6921. https://doi.org/10.1039/C4TC00988F.

[147] A. Dager, T. Uchida, T. Maekawa, M. Tachibana, Synthesis and characterization of mono-disperse carbon quantum dots from Fennel seeds: Photoluminescence analysis using machine learning, Sci. Rep. 9 (2019) 14004. https://doi.org/10.1038/s41598-019-50397-5.

[148] S. Devi, R.K. Gupta, A.K. Paul, S. Tyagi, Waste carbon paper derivatized Carbon quantum dots/(3-aminopropyl)triethoxysilane based fluorescent probe for trinitrotoluene detection, Mater. Res. Express. 6 (2018) 025605. https://doi.org/10.1088/2053-1591/aaf03c.

[149] X. Ma, S. Li, V. Hessel, L. Lin, S. Meskers, F. Gallucci, Chemical engineering and processing: process intensification synthesis of luminescent carbon quantum dots by microplasma process, Chem. Eng. Process. Process Intensif. 140 (2019) 29–35. https://doi.org/10.1016/j.cep.2019.04.017.

[150] L. Liu, Y. Li, L. Zhan, Y. Liu, C. Huang, One-step synthesis of fluorescent hydroxyls-coated carbon dots with hydrothermal reaction and its application to optical sensing of metal ions, Sci. China Chem. 54 (2011) 1342–1347. https://doi.org/10.1007/s11426-011-4351-6.

[151] L. Wang, S.J. Zhu, H.Y. Wang, S.N. Qu, Y.L. Zhang, J.H. Zhang, Q.D. Chen, H.L. Xu, W. Han, B. Yang, H.B. Sun, Common origin of green luminescence in carbon nanodots and graphene quantum dots, ACS Nano. 8 (2014) 2541–2547. https://doi.org/10.1021/nn500368m.

[152] S. Zhu, Y. Song, X. Zhao, J. Shao, J. Zhang, B. Yang, The photoluminescence mechanism in carbon dots (graphene quantum dots, carbon nanodots, and polymer dots): current state and future perspective, Nano Res. 8 (2015) 355–381. https://doi.org/10.1007/s12274-014-0644-3.

[153] K.J. Mintz, Y. Zhou, R.M. Leblanc, Recent development of carbon quantum dots regarding their optical properties, photoluminescence mechanism, and core structure, Nanoscale. 11 (2019) 4634–4652. https://doi.org/10.1039/C8NR10059D.

[154] M. Hesari, Z. Ding, A Perspective on Application of Carbon Quantum Dots in Luminescence Immunoassays, Front. Chem. 8 (2020). https://doi.org/10.3389/fchem.2020.580033.

[155] H. Ding, S.B. Yu, J.S. Wei, H.M. Xiong, Full-color light-emitting carbon dots with a surface-state-controlled luminescence mechanism, ACS Nano. 10 (2016) 484–491. https://doi.org/10.1021/acsnano.5b05406.

[156] G. Liu, J. Zhao, S. Wang, S. Lu, J. Sun, X. Yang, Enzyme-induced in situ

generation of polymer carbon dots for fluorescence immunoassay, Sensors Actuators B Chem. 306 (2020) 127583. https://doi.org/10.1016/j.snb.2019.127583.

[157] N.A. Alarfaj, M.F. El-Tohamy, H.F. Oraby, New Immunosensing-Fluorescence Detection of Tumor Marker Cytokeratin-19 Fragment (CYFRA 21-1) Via Carbon Quantum Dots/Zinc Oxide Nanocomposite, Nanoscale Res. Lett. 15 (2020) 12. https://doi.org/10.1186/s11671-020-3247-9.

[158] K. Zhang, J.H. Park, Surface localization of defects in black TiO_2: Enhancing photoactivity or reactivity, J. Phys. Chem. Lett. 8 (2017) 199–207. https://doi.org/10.1021/acs.jpclett.6b02289.

[159] X. Pan, M.Q. Yang, X. Fu, N. Zhang, Y.J. Xu, Defective TiO_2 with oxygen vacancies: Synthesis, properties and photocatalytic applications, Nanoscale. 5 (2013) 3601–3614. https://doi.org/10.1039/c3nr00476g.

[160] A. Naldoni, M. Allieta, S. Santangelo, M. Marelli, F. Fabbri, S. Cappelli, C.L. Bianchi, R. Psaro, V. Dal Santo, Effect of nature and location of defects on bandgap narrowing in black TiO_2 nanoparticles, J. Am. Chem. Soc. 134 (2012) 7600–7603. https://doi.org/10.1021/ja3012676.

[161] X. Zhang, W. Hu, K. Zhang, J. Wang, B. Sun, H. Li, P. Qiao, L. Wang, W. Zhou, Ti^{3+} self-doped black TiO2 nanotubes with mesoporous nanosheet architecture as efficient solar-driven hydrogen evolution photocatalysts, ACS Sustain. Chem. Eng. 5 (2017) 6894–6901. https://doi.org/10.1021/acssuschemeng.7b01114.

[162] X. Zou, J. Liu, J. Su, F. Zuo, J. Chen, P. Feng, Facile synthesis of thermal- and photostable titania with paramagnetic oxygen vacancies for visible-light photocatalysis, Chem. – A Eur. J. 19 (2013) 2866–2873. https://doi.org/https://doi.org/10.1002/chem.201202833.

[163] Z. Lu, C.-T. Yip, L. Wang, H. Huang, L. Zhou, Hydrogenated TiO_2 nanotube arrays as high-rate anodes for lithium-ion microbatteries, Chempluschem. 77 (2012) 991–1000. https://doi.org/https://doi.org/10.1002/cplu.201200104.

[164] X. Liu, G. Zhu, X. Wang, X. Yuan, T. Lin, F. Huang, Progress in black titania: a new material for advanced photocatalysis, Adv. Energy Mater. 6 (2016) 1600452. https://doi.org/https://doi.org/10.1002/aenm.201600452.

[165] Carbon | XPS Periodic Table | Thermo Fisher Scientific, (n.d.). https://www.thermofisher.com/by/en/home/materials-science/learning-center/periodic-table/non-metal/carbon.html (accessed June 27, 2022).

[166] T.L. Barr, M. Yin, Concerted X-ray photoelectron spectroscopy study of the character of select carbonaceous materials, J. Vac. Sci. Technol. A. 10 (1992) 2788–2795. https://doi.org/10.1116/1.577911.

[167] J.E. Wertz, J.R. Bolton, Electron Spin Resonance, Springer Netherlands, Dordrecht, 1986. https://doi.org/10.1007/978-94-009-4075-8.

[168] E.A. Reyes-Garcia, Y. Sun, K.R. Reyes-Gil, D. Raftery, Solid-state NMR and EPR analysis of carbon-doped titanium dioxide photocatalysts ($TiO_{2-x}C_x$), Solid State Nucl. Magn. Reson. 35 (2009) 74–81. https://doi.org/10.1016/J.SSNMR.2009.02.004.

[169] M. Fittipaldi, D. Gatteschi, P. Fornasiero, The power of EPR techniques in revealing active sites in heterogeneous photocatalysis: The case of

anion doped TiO_2, Catal. Today. 206 (2013) 2–11. https://doi.org/10.1016/J.CATTOD.2012.04.024.

[170] M.A. Augustyniak-Jabłokow, Y. V. Yablokov, B. Andrzejewski, W. Kempiński, S. Łoś, K. Tadyszak, M.Y. Yablokov, V.A. Zhikharev, EPR and magnetism of the nanostructured natural carbonaceous material shungite, Phys. Chem. Miner. 37 (2010) 237–247. https://doi.org/10.1007/s00269-009-0328-9.

[171] V.A. Andrjushkova, O. V. Poluboyarov, M.Y. Bulynnikova, The nature of electron paramagnetism and optical absorption of pyrolized organic substances, Izv. Sib. Otd. Akad. Nauk SSSR. Sib. J. Chem. (1992) 5–22.

[172] I. Suarez-Martinez, N. Grobert, C.P. Ewels, Nomenclature of sp carbon nanoforms, Carbon N. Y. 50 (2012) 741–747. https://doi.org/10.1016/j.carbon.2011.11.002.

[173] R.T.K. Baker, Catalytic growth of carbon filaments, Carbon N. Y. 27 (1989) 315–323. https://doi.org/10.1016/0008-6223(89)90062-6.

[174] J.-P. Tessonnier, D.S. Su, Recent progress on the growth mechanism of carbon nanotubes: A Review, ChemSusChem. 4 (2011) 824–847. https://doi.org/https://doi.org/10.1002/cssc.201100175.

[175] A.S. Kotosonov, D. V. Shilo, Electron spin resonance study of carbon nanotubes, Carbon N. Y. 36 (1998) 1649–1651. https://doi.org/10.1016/S0008-6223(98)00159-6.

[176] A. Davydov, Molecular spectroscopy of oxide catalyst surfaces, John Wiley & Sons Ltd, Chichester, 2003.

[177] G. Socrates, Infrared and Raman characteristic group frequencies : tables and charts, 3rd ed., John Wiley & Sons, Ltd, Chichester, 2001. http://lib.ugent.be/catalog/rug01:001212111.

[178] R.J. Gonzalez, Raman, Infrared, X-ray, and EELS studies of nanophase titania, Virginia Polytechnic Institute and State University, 1996.

[179] G. Busca, G. Ramis, J.M.G. Amores, V.S. Escribano, P. Piaggio, FT Raman and FTIR studies of titanias and metatitanate powders, J. Chem. Soc. Faraday Trans. 90 (1994) 3181–3190. https://doi.org/10.1039/FT9949003181.

[180] T. Ohsaka, F. Izumi, Y. Fujiki, Raman spectrum of anatase, TiO_2, J. Raman Spectrosc. 7 (1978) 321–324. https://doi.org/https://doi.org/10.1002/jrs.1250070606.

[181] W.F. Zhang, Y.L. He, M.S. Zhang, Z. Yin, Q. Chen, Raman scattering study on anatase TiO2 nanocrystals, J. Phys. D. Appl. Phys. 33 (2000) 912–916. https://doi.org/10.1088/0022-3727/33/8/305.

[182] J.C. Parker, R.W. Siegel, Calibration of the Raman spectrum to the oxygen stoichiometry of nanophase TiO_2, Appl. Phys. Lett. 57 (1990) 943–945. https://doi.org/10.1063/1.104274.

[183] J. Hodkiewicz, Characterizing carbon materials with Raman spectroscopy, in: Thermo Fisher Scientific Inc., Medison, WI, USA, 2010.

[184] C. de Almeida Filho, A.J.G. Zarbin, Porous carbon obtained by the pyrolysis of TiO_2/poly(furfuryl alcohol) nanocomposite: preparation, characterization and utilization for adsorption of reactive dyes from aqueous solution, J. Braz. Chem. Soc. 17 (2006) 1151–1157. https://doi.org/10.1590/S0103-50532006000600012.

[185] G. Scarel, C.J. Hirschmugl, V. V Yakovlev, R.S. Sorbello, C.R. Aita, H. Tanaka, K. Hisano, Infrared response of vitreous titanium dioxide films with anatase short-range order, J. Appl. Phys. 91 (2002) 1118–1128. https://doi.org/10.1063/1.1427430.

[186] T. Fuchigami, S. Inagi, M. Atobe, eds., Fundamentals and applications of organic electrochemistry, John Wiley & Sons Ltd, Chichester, United Kingdom, 2014. https://doi.org/10.1002/9781118670750.

[187] Z. Wang, C. Yang, T. Lin, H. Yin, P. Chen, D. Wan, F. Xu, F. Huang, J. Lin, X. Xie, M. Jiang, Visible-light photocatalytic, solar thermal and photoelectrochemical properties of aluminium-reduced black titania, Energy Environ. Sci. 6 (2013) 3007–3014. https://doi.org/10.1039/C3EE41817K.

[188] S. Livraghi, M. Chiesa, M.C. Paganini, E. Giamello, On the nature of reduced states in titanium dioxide as monitored by electron paramagnetic resonance. I: The anatase case, J. Phys. Chem. C. 115 (2011) 25413–25421. https://doi.org/10.1021/jp209075m.

SANTRAUKA

Ventilinių metalų paviršiaus anodinė oksidacija (anodavimas) plačiai taikomas ir patogus būdas formuoti apsaugines bei tvarkias oksidines nanomedžiagas. Jų savybės kontroliuojamos keičiant anodavimo tirpalų sudėtį ir režimo parametrus. Pagrindiniai iš jų: anodavimo įtampa, elektrolito tipas, jo koncentracija ir temperatūra lemia suformuotų plėvelių morfologiją ir sudėtį. Anodinių oksidų modifikavimas elektrolitų komponentais elektrocheminės oksidacijos metu galėtų būti naudingas siekiant reguliuoti medžiagų savybes. Atliekant vienpakopį aliuminio anodavimą organinėse rūgštyse, tokiose kaip oksalo, malono, vyno ir glikolio rūgštis, dėl elektrocheminio anijono transformacijos AAO plėvelėje susidaro amorfinės anglies dariniai, kurie lemia gautų dangų fluorescencijos pokyčius. Tokių dangų fluorescencijos maksimumo padėtis bei emisijos intensyvumas ženkliai pasikeičia. Anglies/AAO kompozicinės dangos galėtų būti naudojamos kaip stipriai adsorbuojantys paviršiai, katalizatoriai, katalizatoriaus laikikliai, superkondensatoriai, kuro elementų elektrodų medžiagos ir absorbentai dujoms laikyti. Tačiau minėtų elektrolitų atveju anodavimas vyksta esant aukštesnei nei 100 V įtampai, kuri yra per didelė plačiam šių procesų panaudojimui. Todėl tenka ieškoti elektrolitų, kurie leistų formuoti anglimi praturtintas AAO plėveles anoduojant aliuminį žemesne įtampa.

Analogiškai AAO, amorfinės anglies intarpai gali susidaryti anoduojant titaną organiniuose elektrolituose. Titano nanovamzdelių modifikavimas anglimi padidina jų fotokatalitinį aktyvumą. Be to anglies darinių įsiterpimas galimai skatina tvarkių TiO_2 nanokristalų „augimą“ ir nulemia medžiagos savybes. Labiau suprantant anglies junginių įsiterpimo į anodinius oksidus procesus, jų cheminę prigimtį ir struktūrinius ypatumus, galima būtų sukurti naujas medžiagas, turinčias reikiamą morfologiją ir pasižyminčias naujomis fizikocheminėmis, fotokatalitinėmis ir optinėmis savybėmis.

Disertacijos tikslas

Anglies turinčių anodinių aliuminio ir titano oksidų plėvelių formavimo vienpakopiu elektrocheminiu apdorojimu galimybių tyrimas, suformuotų dangų charakterizavimas ir taikymo sričių paieška.

Disertacijos uždaviniai

1. Ištirti anglies turinčių anodinių aliuminio oksido (AAO) plėvelių elektrocheminio formavimosi ypatumus elektrolituose, įgalinančiuose anglies darinių formavimąsi ir įsiterpimą į AAO plėveles.
2. Optimizuoti AAO plėvelių su didesniu anglies kiekiu formavimo žemesne anodavimo įtampa sąlygas, ištirti suformuotų plėvelių sudėtį, struktūrą, optines savybes ir palyginti su kitomis anodine poliarizacija suformuotomis anglies/aliuminio oksidų kompozicinėmis medžiagomis.
3. Ištirti titano anodinės oksidacijos metu įsiterpiančios į dangą anglies cheminę būseną.
4. Nustatyti anodinių plėvelių struktūros, morfologijos ir fluorescencijos priklausomybę nuo įsiterpusios anglies kiekio ir būsenos.
5. Iš anglimi praturtintų AAO plėvelių išskirti ir charakterizuoti anglies (nano)darinius.

Ginamieji teiginiai

1. Įsiterpusi į skruzdžių rūgšties ir amonio heptamolibdato (arba natrio vanadato) elektrolite formuojamą AAO anglis yra karboksilato jonų ir kitų sp^2 ir sp^3 hibridizacijos anglies formų pavidale.
2. Į AAO plėveles, suformuotas skruzdžių rūgšties elektrolituose, įsiterpusios anglies kiekis siekia ~5,0 masės %, tai yra, dvigubai daugiau nei anoduojant aliuminį oksalo ar vyno rūgštyse, nepaisant ženkliai aukštesnės anodavimo įtampos pastarosiose.
3. Amonio heptamolibdato ir natrio vanadato pridėjimas į skruzdžių rūgšties elektrolitą slopina aliuminio tirpimą anodavimo metu, padidina plėvelių storį ir skatina anglies įsiterpimą į AAO matricą. Pridėjus oksalo rūgšties suformuojamos storesnės ir lygesnės dangos.
4. Įsiterpę į skruzdžių rūgšties tirpaluose suformuotas AAO plėveles anglies junginiai pasižymi nuo sužadinimo priklausoma mėlynąja fluorescecija.

Naujumas

Amonio heptamolibdato, natrio metavanadato ir oksalo rūgšties priedų panaudojimas skruzdžių rūgštyje pirmą kartą leido padidinti formuojamos anodinio aliuminio oksido plėvelės storį nuo 1 iki 20–40 µm. Priklausomai nuo tirpalo sudėties, anoduojant 80 V įtampa, analogiška anodavimo oksalo rūgšties tirpale įtampai ir 2,5 karto mažesne nei anoduojant vyno rūgšties tirpale, vidutinis anglies kiekis plėvelėse nesumažėja ir siekia 3,45–

5,5 masės %, t.y., beveik dvigubai daugiau nei plėvelėse, suformuotose oksalo ir vyno rūgščių tirpaluose. Parodyta, kad į anodines aliuminio oksido plėveles įsiterpia CO_2 and CO molekulės, karboksilato jonai ir kiti *sp*^{2} ir *sp*^{3} hibridizacijos formų anglį turintys komponentai. Aliuminio anodinės oksidacijos metu įsiterpę anglį turintys komponentai buvo išskirti iš aliuminio oksido matricos. Pirmą kartą parodyta, kad šie komponentai yra biologiškai suderinamos liuminescuojančios nanodalelės, pasižyminčios priklausoma nuo sužadinimo 280–450 nm bangos ilgiu emisija.

Disertacijos praktinė vertė

1. Sukurtos ir optimizuotos sąlygos anglimi praturtintų AAO plėvelių sintezei sudėtiniuose elektrolituose, kuriuose yra 0,4 M skruzdžių rūgšties, 0,03 M amonio heptamolibdato arba 0,2 M natrio vanadato ir oksalo rūgšties. ~ 5,0 masės % anglies kiekis plėvelėse gaunamas palaikant 80 V anodavimo įtampos režimą.
2. Ištirtas amonio heptamolibdato, natrio vanadato ir oksalo rūgšties poveikis AAO plėvelių, suformuojamų skruzdžių rūgšties anodavimo elektrolituose, sudėčiai ir morfologijai.
3. Nustatyta, kad, priklausomai nuo elektrolito sudėties, į AAO įterptos anglies kiekis yra 3,45–5,75 masės %; anglis yra CO_2, CO, karboksilato jonų ir kitų *sp*^{2} ir *sp*^{3} hibridizacijos anglies darinių formose.
4. Nustatyta plati mėlynos spalvos AAO plėvelių fluorescencija 350–700 nm bangos ilgio ruože, su maksimumu ties 460 nm. AAO fluorescencijai būdingas neeksponentinis gesimas, jos vidutinė gyvavimo trukmė yra apie 0,30–0,32 ns.
5. Aliuminio anodinės oksidacijos metu į oksido matricą įsiterpę anglies dariniai gali būti išskiriami iš AAO matricos ir naudojami kaip liuminesuojančios ir biologiškai suderinamos nanodalelės. Šių nanodalelių liuminescencijos emisija priklauso nuo žadinimo bangos ilgio 280–450 nm ruože. Liuminescencijos vidutinė gyvavimo trukmė varijuoja nuo 7,25 iki 8,04 ns.

Medžiagos ir tyrimo metodai

Anglimi praturtintos AAO plėvelės buvo gautos pastovios įtampos režimu (anodavimo įtampa (U_a) svyravo nuo 60 iki 100 V), esant pastoviai 18 °C temperatūrai sudėtiniuose elektrolituose. Elektrolitų sudėtis: 0,4–0,8 M skruzdžių rūgšties, 0,03 M amonio heptamolibdato arba 0,2 M natrio vanadato ir 5–100 mM oksalo rūgšties.

Aliuminio elektrocheminei oksidacijai kompleksiniuose elektrolituose apibūdinti U_a diapazone nuo 0 iki 100 V, buvo pritaikytas linijinio skleidimo voltamperometrijos (LSV) metodas. AAO plėvelių paviršius morfologija ir skerspjūviai buvo ištirti skenuojančia elektronine mikroskopija (SEM). Anglies ir aliuminio kiekiai anodinėje plėvelėje nustatyti termogravimetrine (TG)/diferencine termine analizė (DTA) kartu su išsiskyrusių H_2O, CO_2 ir CO dujų masės spektrometrijos analize (MS). Siekiant nustatyti plėvelių sudėtį, atlikti Furjė transformacijos infraraudonųjų spindulių (FTIR) matavimai. Rentgeno fotoemisijos spektroskopijos (RFS) tyrimai atlikti siekiant gauti informacijos apie anglies, aliuminio, molibdeno ir deguonies chemines būsenas AAO plėvelėse. Plėvelės fluorescencinės savybės buvo tiriamos naudojant juostelių kamerą (1 Pav.).

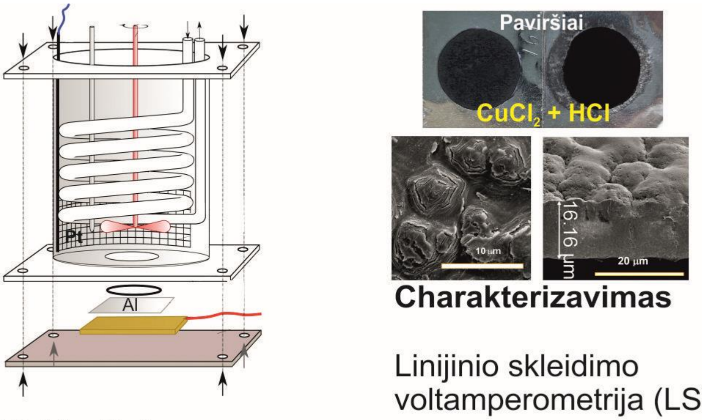

Charakterizavimas

Linijinio skleidimo voltamperometrija (LSV)

Skenuojanti elektroninė mikroskopija (SEM)

Diferencinė terminė analizė (TG/DTA/MS)

Rentgeno fotoemisijos spektroskopija (XPS)

Infraraudonųjų spindulių spektroskospija (IR)

Fluorescencinė spektr.

Elektrolitai

0,8 M HCOOH
0,2 M $NaVO_3$

0,4 M HCOOH
0,03 M $(NH_4)_6Mo_7O_{24}$

0,4 M HCOOH
0,03 M $(NH_4)_6Mo_7O_{24}$
5−100 mM $H_2C_2O_4$

0,4 M HCOOH
20 mM $H_2C_2O_4$

1 pav. Anodinio aliuminio oksido plėvelės: mėginių paruošimas ir charakterizavimas.

Siekiant nustatyti anglies nanodarinių, įsiterpusių į aliuminio oksido matricą, prigimtį ir pobūdį, pastarieji buvo išskirti iš AAO plėvelių, suformuotų esant skirtingomis sąlygomis, (2 pav.). Nustatyta, kad išskirta anglis yra anglies nanodalelės. Tai buvo įrodyta naudojant peršviečiamąją elektroninę mikroskopiją, sustiprintą Ramano sklaidą, UV-Vis spektroskopiją ir pastovios būsenos fluorescencinę spektroskopiją su laiko skiriamaja geba.

Anglies nanodalelių biologinis suderinamumas buvo nustatytas naudojant COS-7 ląsteles (Cell line service, produkto numeris 605470), išaugintas Ibidi high 8 šulinėlių plokštelėje (Ibidi, katalogo numeris: 80806) DMEM terpėje (Gibco, katalogo numeris: 31053028), papildytas 10% galvijų vaisiaus serumu (FBS) (Gibco, katalogo numeris: A3840102) ir penicilinu-streptomicinu (Gibco, katalogo numeris: 15140122).

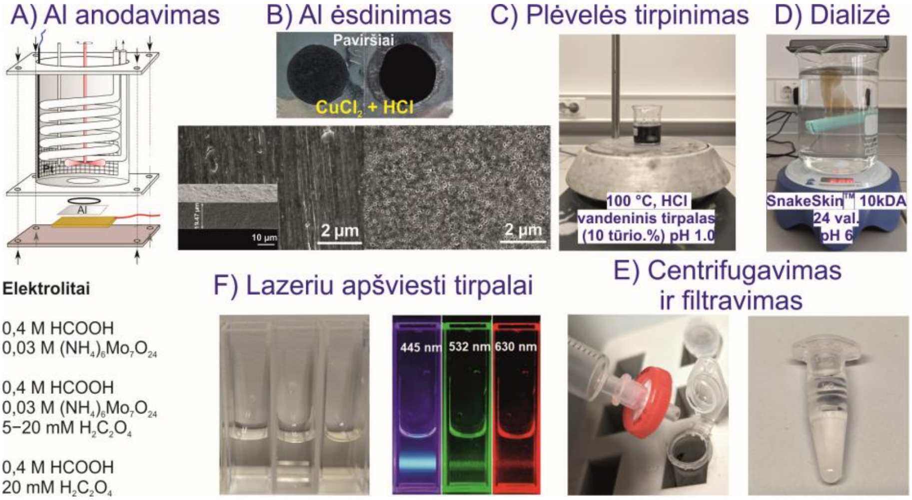

2 pav. Anglies išskyrimo iš anglimi praturtintų AAO plėvelių schematinė iliustracija. Aliuminio anodavimo skirtinguose elektrolituose, kuriuose yra skruzdžių rūgšties principinė schema (A), AAO plėvelių ėsdinimas ir SEM vaizdai (B), plėvelės tirpinimas (C), tirpalo dializė (D), centrifūgavimas ir filtravimas (E) ir galutinio produkto liuminescencijos tyrimas žadinant 445 nm (mėlyna), 532 nm (žalia) ir 630 nm (raudona) bangos ilgio šviesa (F).

Rezultatai ir jų aptarimas

Nustatyta, kad aliuminio elektrocheminė oksidacija skruzdžių rūgšties tirpaluose leidžia gauti porėtas AAO plėveles prie žemesnių anodavimo įtampų (apie 22 V) su ženkliai didesniu anglies kiekiu (iki 5,8 masės%) lyginant su AAO gautose anoduojant kitose organinėse rūgštyse, tokiose kaip oksalo, malono ir vyno rūgštis. Tačiau skruzdžių rūgšties anodinio aliuminio oksido plėvelės neturi įprastos porėtos struktūros, o jų storis neviršija 1 μm. Tikslus formiato jonų skilimo mechanizmas ir skirtingų formų anglies įsiterpimo į AAO mechanizmas nėra ištirti ir reikalauja tolesnių tyrimų. Aliuminio anodavimo skruzdžių rūgštyje tobulinimo strategija galėtų būti tokia: į anodavimo elektrolitą pridėti nedidelį kiekį oksianijonų, tokių kaip vanadatai, molibdatai, volframatai ir (arba) organinių rūgščių, tokių kaip oksalo arba vyno.

Tolygūs sodriai juodos spalvos Al paviršiai gauti 0,2–0,25 M $NaVO_3$ ir 0,5–1,0 M HCOOH tirpaluose, kurių pH 2,5–3,0. Esant 20 °C ir 80 V anodavimo režimui, per 1 val. susidaro vienodo, apytiksliai 40 μm storio ir ryškios juodos spalvos, plėvelės. Skruzdžių rūgšties su natrio vanadato priedais elektrolito sudėtis buvo optimizuota siekiant gauti tolygias ir sodrios juodos spalvos AAO paviršiaus dangas. Tačiau vanadžio (V) ir chromo (VI) jonai yra toksiški. Būtų logiška vanadatus pakeisti netoksiškais, aplinkai draugiškesniais penkiavalenčių vanadžio jonų analogais, kaip antai molibdato (VI) junginiais. Tai buvo pagrindinis tolimesnių tyrimų objektas. Toliau tęsėme $(NH_4)Mo_7O_{24}$ priedų poveikio AAO „augimui“ tyrimus optimizuojant aliuminio anodavimo sąlygas ir naudojant sudėtinius elektrolitus, kuriuose yra skruzdžių rūgšties ir amonio heptamolibdato.

Darbe tirta AAO/anglies kompozicinių dangų, suformuotų anoduojant aliuminį 60–80 V įtampos režime vandeniniame skruzdžių rūgšties tirpale su amonio heptamolibdato priedais, morfologijos ir sudėties priklausomybė nuo formavimo sąlygų ir fluorescencijos priklausomybė nuo įterptos anglies kiekio bei būsenos. Linijinio skleidimo voltamperometrijos ir poliarizacijos kreivių tyrimai parodė, kad registruotas srovės profilis yra netolygus. Iš čia seka, kad anodavimo procesas nėra pastovus, o tai lemia daugialypės porėtos struktūros formavimąsi. Termogravimetrijos, diferencinės terminės analizės ir infraraudonųjų spindulių spektroskopijos tyrimai parodė, kad vidutinis anglies kiekis yra apie 5,5 masės %, o į AAO įsiterpusi anglis yra CO_2, CO, karboksilato jonų ir kitų sp^2 ir sp^3 hibridizacijos anglies darinių pavidalu. AAO plėvelių paviršiaus ir atvirkštinės pusės Ože elektronų spektroskopijos tyrimai įrodė, kad anglis yra ne tik paviršiuje, bet ir tolygiai pasiskirsto per oksido sluoksnį. Remiantis fluorescencijos tyrimais, aliuminio oksido/anglies kompozicinė danga turi plačią mėlyną fluorescenciją 350–700 nm bangos ilgio regionuose su fluorescencijos maksimumu ties 460 nm. Gauti rezultatai rodo, kad fluorescencijos spektro dinamika yra neeksponentinė ir gali būti aprašyta kaip kelių skilimo komponentų superpozicija. Šie komponentai gali būti įvairūs anglies turintys junginiai ir funkcinės grupės, tokios kaip C=O ir COOH. Tačiau, remiantis SEM rezultatais, plėvelės turi iškilimų ir yra sutrūkinėjusios. Prailginus anodavimo trukmę, iškilimų dydis ir aukštis didėja, jose susidaro daug terasų. Fazių sąlyčio riba tarp AAO plėvelės ir aliuminio yra banguota. Nustatyta, kad šią problemą galima išspręsti į anodavimo tirpalą įdėjus nedidelį kiekį oksalo rūgšties.

5–20 mM koncentracijos oksalo rūgšties pridėjimas į 0,4 M skruzdžių rūgšties tirpalą, kuriame yra 0,03 M amonio heptamolibdato, išlygina AAO plėvelės ir aliuminio fazių sąlyčio ribą; 100 mM oksalo rūgšties pridėjimas į elektrolitą beveik visiškai blokuoja reguliarios anodinės plėvelės augimą. Pastebėta, kad anoduojant aliuminį skruzdžių rūgštyje su amonio heptamolibdato priedu, pastarasis apsaugo plėvelę nuo aliuminio tirpimo žymiai efektyviau nei naudojant tik oksalo rūgšties priedus. Pagrindinė oksalo rūgšties paskirtis anodavimo proceso metu yra pagerinti plėvelės morfologiją. Amonio heptamolibdatas padidina plėvelės storį. Linijinio skleidimo voltamperometrijos tyrimai kartu su AAO bandinių SEM analize parodė, kad heptamolibdato turinčiuose elektrolituose anodavimo proceso pradžioje susidaro plona porėta AAO plėvelė. Pasiekus elektrolito oksidacijos potencialą, plona paviršinė plėvelė yra pramušama, todėl anoduojamasis paviršius ženkliai padidėja, o anodinis oksidas pradeda sparčiai augti (3 pav.).

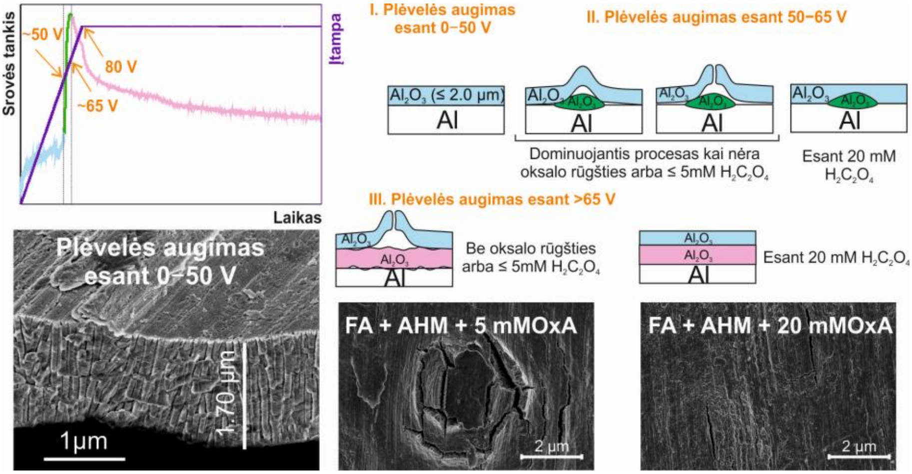

3 pav. Elektrocheminės aliuminio oksidacijos 0,4 M HCOOH (OxA) elektrolite su 0,03 M $(NH_4)_6Mo_7O_{24}$ (AHM) ir 5–20 mM $H_2C_2O_4$ (OxA) priedais, procesų schematinis vaizdavimas.

Elektrolito sudėtyje esant amonio heptamolibdato priedams įsiterpęs anglies kiekis karbonato-karboksilato pagrindu ir *sp*^{2} ir *sp*^{3} hibridizacijos būsenose esančių formų bei suminės anglies kiekis reikšmingai nesikeičia ir atitinkamai yra 4,87–5,05 masės% ir 4,97–5,67 masės%. Skruzdžių rūgšties elektrolito su oksalo rūgšties priedais atveju, *sp*^{2} ir *sp*^{3} būsenų anglies ir bendras anglies kiekis sumažėja atitinkamai iki 3,23 masės% ir 3,37 masės %, palyginus su AAO sudėtimi suformuota naudojant elektrolitus, kurių sudėtyje yra tik heptamolibdato priedai (1 lentelė).

Remiantis gautais rezultatais galime daryti išvadą, kad į anodavimo elektrolitą, kuriame yra 0,4 M HCOOH ir 0,03 M $(NH_4)_6Mo_7O_{24}$, įdėjus 20 mM oksalo rūgšties pagerėja plėvelių paviršiaus morfologija be ženklaus anglies kiekio sumažėjimo.

1 lentelė. Anglies kiekis (masės %) išmatuotas TG/DTA/MS metodu AAO plėvelėse, susidarančiose oksiduojant aliuminį 0,4 M HCOOH (FA) elektrolite, turinčiame skirtingą kiekį $H_2C_2O_4$ (OxA) su 0,03 M $(NH_4)_6Mo_7O_{24}$ (AHM) priedais ir be jo, palaikant pastovią 80 V įtampą.

Pavyzdžiai	**ω_C (bendras), masės%**
FA+AHM	5,31
FA+AHM+5mMOxA	5,67
FA+AHM+10mMOxA	5,24
FA+AHM+20mMOxA	4,97
FA+20mMOxA	3,37

Aliuminio anodinės oksidacijos metu AAO matricoje susidarę ir iš jos išskirti anglies intarpai yra liuminescuojančios ir biologiškai suderinamos nanodalelės. Jų liuminescencijos emisija 280–450 nm ruože priklauso nuo žadinimo bangos ilgio. Vidutinė liuminescencijos gyvavimo trukmė, priklausomai nuo plėvelės sudėties, yra 7,25–8,04 ns. Kadangi anglies nanodalelės buvo gautos ištirpinant AAO plėveles be papildomo apdorojimo (pvz., ultragarso), galime padaryti keletą išvadų: (*i*) formiato jonų oksidacijos metu susidariusi anglis yra įsiterpusi į AAO plėvelę sp^2 ir sp^3 būsenose; (*ii*) įsiterpusios anglies komponentai yra liuminescuojančios anglies nanodalelės; (*iii*) AAO matrica žymiai sumažina įsiterpusios anglies fluorescenciją.

Remdamiesi gautų anglies nanodalelių biologinio suderinamumo tyrimų rezultatais, darome išvadą, kad anglies nanodalelės, išskirtos iš skirtingų anglimi praturtintų AAO plėvelių, pasižymi dideliu biologiniu suderinamumu, todėl galėtų būti panaudojamos įvairiems *in vivo* taikymams be didesnės žalos gyvų ląstelių vientisumui.

Naudojant įvairius spektrinius ir struktūrinius medžiagų analizės metodus nustatyti juodos spalvos TiO_2 nanovamzdelių struktūriniai ypatumai ir juose įsiterpusios anglies cheminė būsena. Nanovamzdelinės morfologijos, juodos spalvos anatazo (TiO_2) plėvelės gaunamos atkaitinant amorfinį TiO_2 vandenilio atmosferoje 500 °C temperatūroje. Remiantis eksperimentiniais duomenimis nustatyta, kad juodą plėvelių spalvą lemia amorfinės, į grafitą panašios (grafitizuotos) anglies dariniai. Anglies kiekis, esantis juodos spalvos TiO_2 nanovamzdeliuose, žymiai viršija Ti^{3+} jonų kiekį. Atskleista amorfinės anglies išsidėstymo juodos spalvos TiO_2 nanovamzdeliuose tvarka. Įsiterpusios anglies dariniai nanostruktūrizuotoje porėtoje TiO_2 plėvelėje suteikia jai sodrią juodą spalvą, kuri yra svarbi norint gauti šviesą sugeriančias dangas su minimaliu šviesos atspindžiu. Anglies įsiterpimo ir susidarymo procesų valdymas įgalina nanovamzdelinių TiO_2 plėvelių optinių ir kitų savybių reguliavimo galimybes.

Išvados

1. Amonio heptamolibdato ir natrio metavanadato priedai, kaip korozijos inhibitoriai, stabdo aliuminio tirpimą pradinėse aliuminio anodavimo skruzdžių rūgšties tirpaluose stadijose taip padidindami plėvelės augimo greitį ir storį. Oksalo rūgšties priedai, užkirsdami kelią aliuminio taškinei korozijai, taip pat skatina anodinio aliuminio oksido plėvelės susidarymą skruzdžių rūgšties tirpale. Be to, oksalo rūgšties priedai, sudarydami lygesnio paviršiaus oksido sluoksnį, pagerina plėvelės augimo vienodumą ir morfologiją.
2. AAO plėvelėse, suformuotose sudėtiniuose elektrolituose, turinčiuose skruzdžių rūgšties, amonio heptamolibdato ir oksalo rūgšties, priklausomai nuo elektrolito sudėties vidutinis aptinkamas anglies kiekis yra 3,45–5,75 masės %. Šis kiekis 2,2 ir 1,7 karto didesnis už kiekį, nustatytą oksalo ir vyno rūgšties tirpaluose suformuotose AAO plėvelėse 80 V įtampa, kuri artima anodavimo oksalo rūgštyje įtampai ir 2,5 karto mažesnė už anodavimo vyno rūgštyje įtampą.
3. Į AAO anglis įsiterpia CO_2, CO, karboksilato jonų ir kitų sp^2 ir sp^3 hibridizacijos būsenos anglies junginių pavidalu.
4. AAO plėvelėms charakteringa plati mėlyna fluorescencija 350–700 nm bangų ilgio ruože su fluorescencijos maksimumu ties 460 nm. Fluorescencijos gesimas yra neeksponentinis, jos vidutinė gyvavimo trukmė yra tarp 0,30–0,32 ns. Fluorescencinis spektras yra kelių skilimo komponentų superpozicija. Be deguonies vakansijų, jiems priskirtinos hidroksilo grupės ir anglį turintys junginiai.
5. Aliuminio anodinės oksidacijos metu į oksido matricą įsiterpusi anglis gali būti išskirta iš AAO matricos ir naudojama kaip liuminesuojančios ir biologiškai suderinamos nanodalelės. Priklausomai nuo pradinės AAO plėvelės sudėties išskirtų anglies nanodalelių tirpalams būdinga nuo sužadinimo priklausomos emisijos 280–450 nm bangos ilgio intervale su vidutine 7,25–8,04 ns gyvavimo trukme elgsena.
6. Skirtingos anglies formos taip pat įsiterpia ir į titano anodinio oksido plėveles ir nudažo jas juodai. Etilenglikolio turinčiame elektrolite

susidariusios titano oksido plėvelės paviršiuje nustatytas bendras anglies kiekis yra 20,1 ± 1 at.%, iš kurių 13,8 at.% priskirtini grafitinei angliai.

Autorės indelis

Disertacijoje pateikiami pačios autorės atliktų eksperimentinių tyrimų rezultatai. Disertacinio darbo literatūrinės ir eksperimentinės dalių struktūros, tikslai, pagrindinių tyrimo rezultatų aptarimas ir apibendrinimas atliktas kartu su moksliniu vadovu dr. Arūnu Jagminu. Autorė savarankiškai suformavo visus pavyzdžius, parinko tyrimo metodus jiems charakterizuoti, ruošė pavyzdžius, tiesiogiai dalyvavo tyrime. Dr. Vaclovas Klimas atliko DTA/TG/MS tyrimus. Fluorescenciniai tyrimai ir jų aptarimas buvo atlikti su dr. Renata Karpicz. Dr. Arnas Naujokaitis atliko SEM tyrimus. IR ir Ramano spektroskopijos tyrimus atliko bei gautus rezultatus aptarti padėjo dr. Ieva Matulaitienė. Titano nanovamzdelių mėginių tyrimai buvo atlikti bendradarbiaujant su dr. Marya Invanovskaya, dr. Evgeni Ovodok ir dr. Sergejumi Poznyaku.

Apie autorę

Katsiaryna gimė Minske, Baltarusijoje. 2003 m. baigė 19-ąją Jankos Kupalos vidurinę mokyklą, Minske. 2008 m. įgijo chemijos magistro laipsnį. 2008–2019 metais dirbo tyrėja Baltarusijos valstybiniame Informatikos ir Radioelektronikos universitete. 2019 m. ji pradėjo doktorantūros studijas Valstybiniame mokslinių tyrimų institute Fizinių ir technologijos mokslų centre.

ACKNOWLEDGEMENTS

I would like to thank my supervisor, Dr. Arūnas Jagminas, for his invaluable supervision, support, and tutelage during my PhD studies. Additionally, I would like to thank Dr. Vaclovas Klimas for his treasured support, which influenced my experiment methods and critiqued my results. I am extremely grateful to one of my closest friends and colleagues, Dr. Renata Karpicz, for her help, support, and assistance at every stage of my research, insightful comments, and suggestions. I also thank Dr. Giedrė Grincienė, Dr. Maria Ivanovskaya, and Dr. Rokas Žalneravičius for their shared knowledge and encouragement. I want to thank my lab mates, colleagues, and research team – Dr. Paulius Gaigalas, Dr. Simonas Ramanavičius, and Dr. Ieva Matulaitienė. My appreciation goes to my family and friends for their encouragement and support throughout my studies.

LIST OF PUBLICATIONS

[1] A. Jagminas, V. Klimas, **K. Chernyakova**, V. Jasulaitiene, Designing carbon-enriched alumina films possessing visible light absorption, Materials (Basel). 15 (2022) 2700. https://doi.org/10.3390/ma15072700.

[2] M. Ivanovskaya, K. **Chernyakova**, E. Ovodok, S. Poznyak, D. Kotsikau, I. Azarko, Nature of paramagnetic defects in black titanium dioxide nanotubes, Mater. Chem. Phys. 278 (2022) 125703. https://doi.org/10.1016/j.matchemphys.2022.125703.

[3] M. Ivanovskaya, **K. Chernyakova**, E. Ovodok, S. Poznyak, D. Kotsikau, M. Micusik, Synthesis and structural features of black TiO_2 nanotubes after annealing in hydrogen, Mater. Chem. Phys. 297 (2023) 127416. https://doi.org/10.1016/j.matchemphys.2023.127416.

[4] **K. Chernyakova**, V. Jasulaitiene, A. Naujokaitis, R. Karpicz, I. Matulaitiene, V. Klimas, A. Jagminas, Aluminum anodizing in an aqueous solution of formic acid with ammonium heptamolybdate additive, J. Electrochem. Soc. 170 (2023) 013501. https://doi.org/10.1149/1945-7111/acb019.

[5] **K. Chernyakova**, V. Klimas, R. Karpicz, A. Naujokaitis, A. Jagminas, Effect of oxalic acid additives on aluminum anodizing in formic acid containing ammonium heptamolybdate. J. Electrochem. Soc. (2023) https://doi.org/10.1149/1945-7111/ad0513.

Scientific publications not included in the thesis:

[1] **K. Chernyakova**, B. Tzaneva, I. Vrublevsky, V. Videkov, Effect of aluminum anode temperature on growth rate and structure of nanoporous anodic alumina, J. Electrochem. Soc. 167 (2020) 103506. https://doi.org/10.1149/1945-7111/ab9d65.

[2] U. Samukaite-Bubniene, R. Mazetyte-Stasinskiene, **K. Chernyakova**, R. Karpicz, A. Ramanavicius, Time-resolved fluorescence spectroscopy based evaluation of stability of glucose oxidase, Int. J. Biol. Macromol. 163 (2020) 676–682. https://doi.org/10.1016/j.ijbiomac.2020.06.284.

[3] **K. Chernyakova**, A. Ispas, R. Karpicz, G. Ecke, I. Vrublevsky, A. Bund, Formation of ordered anodic alumina nanofibers during aluminum anodizing in oxalic acid at high voltage and electrical power, Surf. Coatings Technol. 394 (2020) 125813. https://doi.org/10.1016/j.surfcoat.2020.125813.

[4] G. Krucaite, R. Beresneviciute, D. Tavgeniene, S. Grigalevicius, B. Zhang, A. Gruodis, **K. Chernyakova**, R. Karpicz, Hole-transporting materials based on diarylfluorene compounds containing different substituents: DFT simulation, spectroscopic characterization and applications in organic light emitting diodes, Opt. Mater. (Amst).

119 (2021) 111345. https://doi.org/10.1016/j.optmat.2021.111345.

[5] V.G. Pham, N.T. Pham, L.D. Tran, T.H. Dinh, I. Vrublevsky, **K. Charniakova**, H.V. Le, Insight into the effect of zinc oxide nanoparticles coated multi-walled carbon nanotubes (ZnO/MWCNTs) on the thermal conductivity of epoxy nanocomposite as an electrical-insulating coating, J. Aust. Ceram. Soc. (2021). https://doi.org/10.1007/s41779-021-00646-6.

[6] **K. Chernyakova**, I. Vrublevsky, A. Jagminas, V. Klimas, Effect of anodic oxygen evolution on cell morphology of sulfuric acid anodic alumina films, J. Solid State Electrochem. 25 (2021) 1453–1460. https://doi.org/10.1007/s10008-021-04925-x.

[7] **K. Chernyakova**, B. Tzaneva, A. Jagminas, N. Lushpa, I. Vrublevsky, Influence of induced local stress on the morphology of porous anodic alumina at the initial stage of oxide growth, J. Electrochem. Soc. (2023). https://doi.org/10.1149/1945-7111/ad00dd.

Conferences:

[1] „Open Readings 2021“ 16–19 March 2021, Vilnius, Lithuania. Poster presentation: „Effect of substrate nature on cell morphology of thin anodic alumina films formed in the sulfuric acid solution.“

[2] „Advanced Materials and Technologies 2021“ 23–27 August 2021, Palanga, Lithuania. Poster presentation: „Composition and fluorescence properties of electrochemically synthesized nanoporous anodic alumina/carbon composites.“

[3] “Electronics – ET2021” 15–17 September 2021, Sozopol, Bulgaria. Oral presentation: „Obtaining, properties and application of anodic nanoscale films of titanium dioxide on Ti-Al films for perovskite solar cells.“

[4] “FizTech 2021“ 20−21 October 2021, Vilnius, Lithuania. Oral presentation: „Formation of alumina nanofibres during high-field aluminum anodizing.“

[5] „EMRS 2022 Fall Meeting“ 19−22 September 2022, Warsaw, Poland. Poster presentation: „Morphology and composition of black titania nanotubes.“

[6] “FizTech 2022“ 19−20 October 2022, Vilnius, Lithuania. Oral presentation: „Effect of ammonium molybdate additive on the morphology and composition of formic acid anodic alumina.“

[7] „Excited States of Transition Elements (ESTE 2023)” 3–8 September 2023, Sweiradow-Zdroj, Poland. Poster presentation: “Amorphous carbon nanoparticles synthesized by aluminum anodizing in formic acid with ammonium heptamolybdate additives.”

[8] Aluminum Anodizers Council’s Annual Conference and Exposition 10–12 October, 2023, Seattle, USA. Oral presentation: “Aluminum anodizing in heptamolybdate-containing electrolytes.”

About the author:

Katsiaryna was born in Minsk, Belarus. She graduated from secondary school No. 19, named after Ya. Kupala, in Minsk in 2003. In 2008, she got a Master's degree in Chemistry. From 2008 to 2019, she worked as a researcher at the Belarusian State University of Informatics and Radioelectronics. In 2019, she started her Ph.D. studies at the State Research Institute Center for Physical Science and Technology.

NOTES

Vilnius University Press
9 Saulėtekio Ave., Building III, LT-10222 Vilnius
Email: info@leidykla.vu.lt, www.leidykla.vu.lt
bookshop.vu.lt, journals.vu.lt
Print run 30